MAGNETIC ANOMALY MAP AND MAGNETIC STRUCTURE OF SHATSKY RISE (NORTHWEST PACIFIC) AND THE IMPLICATIONS FOR OCEANIC PLATEAU FORMATION

A Dissertation

by

YANMING HUANG

Submitted to the Office of Graduate and Professional Studies of
Texas A&M University
in partial fulfillment of the requirements for the degree of

DOCTOR OF PHILOSOPHY

Chair of Committee,	William W. Sager
Co-chair of Committee,	Zuosheng Yang
Committee Members,	Bradford M. Clement
	Niall Slowey
Head of Department,	Shari Yvon-Lewis

December 2018

Major Subject: Oceanography

ABSTRACT

Oceanic plateaus are common oceanic features and because they are believed to be constructed by magma outpouring from the mantle, knowledge about their formation is important for understanding mantle dynamics. Many oceanic plateaus have been found formed near or at mid-ocean ridges, yet the manner of the interactions between plateau and mid-ocean ridge eruptions are not well understood. Shatsky Rise is an oceanic plateau in the northwest Pacific Ocean. Recent seismic data reveal internal structures of the two largest edifices in Shatsky Rise, Tamu and Ori massifs, which appear to be enormous central volcanoes. However, magnetic lineations imply that they formed near Pacific-Farallon-Izanagi triple junction and are probably traversed by magnetic lineations. It is unclear how such large central volcanoes could have formed at or near spreading ridges, which are themselves enormous linear volcanoes. To understand the magnetic structure and the process of crustal formation, we constructed a magnetic anomaly map for Shatsky Rise and performed magnetic modeling for Tamu and Ori massifs. Surprisingly, the whole of Shatsky Rise is mainly characterized by linear or curvilinear magnetic anomalies, indicating that the emplacements of large, high edifices have little influence on the pattern of magnetic anomalies. Linear magnetic anomalies traverse the centers of Tamu, Ori, and Shirshov massifs, indicating their formation by seafloor spreading. Curvilinear magnetic anomalies and multiple magnetic bights surrounding these three high edifices suggest that their formation involved complex triple junction tectonics, such as microplates, ridge propagations and

reorientations. Magnetic modeling results are consistent with the linear magnetic anomalies having been produced by linear magnetization blocks with opposite geomagnetic polarities. Tamu and Ori massifs show horizontal age progression across the edifices and thus are not central volcanoes formed by vertical stack of lava layers. Although extra magma supply may have thickened the crust of Shatsky Rise, the eruptive volcanism must have been focused on the narrow zone along the ridge axis and no far-travelling lava flows were formed to obscure the linear pattern. Similar to Shatsky Rise, many oceanic plateaus are found near spreading ridges. This coincidence suggests that oceanic plateau formation is an under-examined variant of seafloor spreading.

ACKNOWLEDGEMENTS

I'm in debt to many people who have helped me during my time in graduate school. This dissertation would not have been possible without their supports.

First of all, I am especially grateful to my advisor, also my committee chair, Dr. William W. Sager, who not only taught me how to do scientific research, but also inspired me by his hardworking and passion.

I would like to thank my committee co-chair, Dr. Zuosheng Yang and my committee members, Dr. Bradford M. Clement and Dr. Niall Slowey, for their continuous help during my dissertation work.

I'm also grateful to Dr. Masao Nakanishi for providing valuable marine magnetic data and his guidance on interpreting magnetic anomaly maps. Moreover, I'm thankful to Dr. Masako Tominaga and John Greene for their guidance to magnetic modeling, and thankful to Dr. Jinchang Zhang, William Durkin and Harsha Thoram for their help on programming.

Last but not least, I would like to express my deepest appreciation to my family and friends, especially my wife, Liyan Wang. I would not have gotten through these years without their warm love and encouragement.

CONTRIBUTORS AND FUNDING SOURCES

This work was supervised by a dissertation committee consisting of Professors William W. Sager, Zuosheng Yang and Niall Slowey of the Department of Oceanography and Professor Bradford M. Clement of the Department of Geology and Geophysics.

The Japanese survey data analyzed for Chapter II was partly provided by Professor Masao Nakanishi from Graduate School of Science at Chiba University.

All other work conducted for the dissertation was completed by the student independently.

Graduate study was supported by a fellowship from the Department of Oceanography at Texas A&M University and a fellowship from China Scholarship Council.

TABLE OF CONTENTS

Page

ABSTRACT ii

ACKNOWLEDGEMENTS iv

CONTRIBUTORS AND FUNDING SOURCES v

TABLE OF CONTENTS vi

LIST OF FIGURES viii

LIST OF TABLES xiii

CHAPTER I INTRODUCTION 1

CHAPTER II CORRECTION OF MAGNETIC DATA TO MAKE A MAGNETIC ANOMALY MAP FOR SHATSKY RISE 3

2.1 Overview 3
2.2 Introduction 4
2.2.1 Geological setting of Shatsky Rise 9
2.3 Data and Methods 11
2.3.1 Magnetic data 11
2.3.2 Data processing 16
2.4 Results 26
2.4.1 Comparison with previous isochron map 31
2.4.2 Description of magnetic anomalies 31
2.5 Discussion 39
2.5.1 Construction of magnetic anomaly map 39
2.5.2 Interpretations of the magnetic anomaly map 43
2.5.3 Implications for the formation of Shatsky Rise 46
2.6 Conclusions 49

CHAPTER III MAGNETIC ANOMALY MAP OF ORI MASSIF AND ITS IMPLICATIONS FOR OCEANIC PLATEAU FORMATION 51

3.1 Overview 51
3.2 Introduction 52
3.2.1 Shatsky Rise geologic setting 56
3.2.2 Study rationale and motivation 58
3.3 Data and Methods 59
3.3.1 Magnetic dataset 59
3.3.2 Magnetic modeling 61
3.4 Results 65
3.4.1 Magnetic anomaly map 65
3.4.2 Modeling results 68
3.5 Discussion 72

3.5.1 Magnetic anomaly map 72
3.5.2 Geophysical constraints for magnetic modeling 73
3.5.3 Volcanism at Ori Massif 74
3.6 Conclusions 80

CHAPTER IV MAGNETIC ANOMALY MAP OF TAMU MASSIF IMPLIES ITS FORMATION BY SEAFLOOR SPREADING 83

4.1 Overview 83
4.2 Introduction 84
4.2.1 Geological setting of Tamu Massif 86
4.3 Data and Methods 90
4.3.1 Magnetic dataset 90
4.3.2 Data processing 94
4.3.3 Magnetic modeling 95
4.4 Results 98
4.4.1 Magnetic anomaly patterns 98
4.4.2 Results of magnetic models 103
4.5 Discussion 109
4.6 Conclusion 113

CHAPTER V SUMMARY OF CONCLUSIONS 115

REFERENCES 117

LIST OF FIGURES

Page

Figure 1. Shatsky Rise location, bathymetry and magnetic lineations. TM=Tamu Massif, TR=Toronto Ridge, OM=Ori Massif, SM=Shirshov Massif, PR=Papanin Ridge. Inset map shows the location of Shatsky Rise in the northwest Pacific Ocean. Shatsky Rise bathymetry (Smith and Sandwell, 1997) shallower than -5 km is depicted with contours at 0.5-km intervals. Pink heavy lines denote magnetic lineations and fracture zones (Nakanishi et al., 1999). 8

Figure 2. Chart of magnetic ship tracks over and around Shatsky Rise. Dashed black lines show older cruises positioned with navigation other than GPS. Solid red lines denote surveys positioned with GPS. Thin black contours represent Shatsky Rise bathymetry shallower than -5 km, contoured at 0.5-km intervals. 15

Figure 3. Histogram showing the distribution of magnetic anomaly COE after particular correction steps. (A) COE distribution after just removing internal field (IGRF) contribution. (B) COE distribution after removing outliers & noise and removing external fields (CM4 and Kp). (C) COE distribution after improving data set consistency by 'backbone' analysis. RMS error values are given in Table 2. 18

Figure 4. Examples of data with outliers and noise. Deleted outliers and noise are plotted as red points while retained data are represented by blue points. 19

Figure 5. Influence of magnetic storms when Kp ≤ 5. (Upper) High Kp values without apparent disturbance to shipborne data. (Lower) High Kp values with obvious disturbances to shipborne data. Shipborne data are plotted as black dots. Kp values (given at 3-hour intervals) are plotted as the purple curve and disturbed time periods are denoted by shaded areas. Crossover errors (COE) are denoted as blue, orange, and red diamonds with color based on the magnitude. COE are plotted vertically on the same scale as anomaly values. 20

Figure 6. Effect of manual navigation corrections. Plots are 1 arc-minute gridded magnetic anomaly maps. Black arrows indicate the artifacts (trails) caused by poorly-navigated surveys that disrupt the map pattern. Improvement from navigation corrections are noticeable in the resulting map (right). 24

Figure 7. Detail on effect of manual navigation corrections. Plots are following Figure 6, but show a smaller region, illustrating the improvement in the southwest part of our study area. 25

Figure 8. Ship tracks over Shatsky Rise magnetic anomaly map, showing data constraints for magnetic anomalies. (left) Raw magnetic anomaly map. Green bathymetry contours (4 km in depth) show the footprints of Tamu, Ori and Shirshov massifs. (right) Magnetic anomaly map overlapped with ship tracks. Black lines show older cruises positioned with navigation other than GPS, while red lines denote surveys positioned with GPS. 28

Figure 9. Shatsky Rise magnetic anomaly map with published magnetic isochrons (solid black lines) and fracture zones (dashed black lines) (Nakanishi et al., 1999, 2015). Thicker red (blue) lines show positive (negative) magnetic lineations interpreted from the anomaly map. Green bathymetry contours (4 km in depth) show the footprints of Tamu, Ori and Shirshov massifs. 29

Figure 10. Newly-identified magnetic lineations compared to the Nakanishi et al. (1999) isochron map. Thin solid (dash) gray lines denote isochrons (fracture zones) identified by Nakanishi et al. (1999, 2015). Thicker red (blue) lines show positive (negative) magnetic lineations interpreted from the anomaly map. Green topographic contours (4 km in depth) show the footprints of Tamu, Ori and Shirshov massifs. 30

Figure 11. Magnetic anomaly map of Tamu and Ori Massifs. Annotations are the same as Figure 10 except that topographic contours of -5 km, -4 km, -3 km are shown and ship tracks are represented by gray dashed lines..... 34

Figure 12. Magnetic anomaly map detail showing Shirshov Massif. Annotations are the same as those in Figure 10 except that topographic contours are plotted at 0.5-km intervals and annotated at 1-km intervals. Ship tracks are plotted as gray dashed lines. 37

Figure 13. Magnetic anomaly map of Papanin Ridge. Conventions are the same as Figure 12. 38

Figure 14. The EMAG2v3 map for Shatsky Rise. (left) our new magnetic anomaly map for Shatsky Rise. (right) Shatsky Rise magnetic anomaly map based on EMAG2v3. Annotations are the same as Figure 9. 42

Figure 15. Location map for Shatsky Rise and Ori Massif. Dashed line encompasses the area of Figures 16 to 20. Bathymetric data are estimated depths from satellite altimetry (Smith and Sandwell, 1997). Red lines denote magnetic isochrons and fracture z zones (Nakanishi et al., 1999). Red dots are ODP and IODP drill sites mentioned in the text. Inset shows location of Shatsky Rise relative to Japan and the Japan Trench. 55

Figure 16. (A) Chart of surveys used in this study. Dashed lines denote cruises used in Nakanishi et al. (1999); solid lines are newer data (Table 3). Gray contours show bathymetry at 500-m intervals. (B) Data coverage and anomalies. Data point size is based on anomaly amplitude (larger point = larger anomaly absolute value) and color denotes both amplitude and sign. Annotated solid lines denote isochrons and heavy dashed lines represent fracture zones (Nakanishi et al., 1999). 60

Figure 17. (A) Bathymetry and (B) igneous basement depth maps for Ori Massif. Basement is set at the interface between sediments and basalts by subtracting sediment thickness from bathymetry. Depth contours in both maps are shown at 250-m intervals and are annotated at 500-m intervals. 62

Figure 18. Results from homogeneous magnetization model (Plouff, 1976). X and Y axis denote distance with units of km. (A) Model polygons following depth contours at 200-m intervals and input magnetic anomaly points. Anomaly points are plotted with the same size but with different colors based on anomaly values. (B) Calculated anomalies from the forward model (assuming remanent magnetization inclination, declination, and intensity of 0°, 0°, and 2.7 A/m, respectively). (C) Calculated magnetic field using least-square inversion (inclination, declination, intensity = 25.3°, -31.1°, and 5.8 A/m). (D) Residual magnetic field resulting from subtracting least–square inversion model from observed anomalies. 63

Figure 19. Uniform-thickness layer magnetic inversion model (Parker and Huestis, 1974). (A) Magnetic anomaly map of Ori Massif. Black dotted lines show basement contours from 3.5 km to 4.5 km around the center of Ori Massif. White annotated lines and d dashed lines denote magnetic isochrons and fracture zones identified by Nakanishi et al. (1999), respectively. (B) Calculated magnetization map resulting from the uniform-thickness inverse model (Parker and Heustis, 1974). The assumed remanent magnetic field direction is inclination, -20°, and declination, 20°. Black dotted lines are basement depth contours for reference. 70

Figure 20. Variable-thickness layer magnetic inversion model. A) Magnetic anomaly map for Ori Massif. B) Calculated magnetization map resulting from the variable thickness inverse model (Caratori Tontini et al., 2008). Contours and annotations are the same as Figure 19..... 71

Figure 21. Location, bathymetry and magnetic lineations of Tamu Massif. Bathymetry (Smith and Sandwell, 1997) shallower than -5 km is illustrated with contours at 0.5-km intervals. Magnetic isochrons and fracture zones are denoted as solid and dashed pink lines, respectively, following Nakanishi et al. (1999) and Nakanishi et al. (2015). White filled circles show the locations of the Ocean Drilling Program Site 1213 as well as Integrated Ocean Drilling Program Sites U1347. Inset map shows the locations of Shatsky Rise and Tamu Massif in the northwest Pacific Ocean. . 87

Figure 22. Magnetic ship tracks over Tamu Massif. Red solid lines show the tracks of cruise FK151005. Black solid lines show recent GPS-navigated cruises, black dashed lines denote older cruises with other, less accurate navigation systems. 92

Figure 23. Bathymetry (left) and top of igneous basement (right). Basement top is produced by subtracting sediment thickness from the bathymetry. Topographic contours are plotted at 0.5 km intervals with 1-km intervals shown by thicker lines and annotated. 97

Figure 24. Magnetic anomaly map for Tamu Massif. (left) Anomaly map with bathymetry contours of -5, -4 and -3 km, denoted by green lines. (right) Anomaly map compared to lineations. Solid black lines show magnetic isochrons identified by Nakanishi et al. (1999), and dashed black lines show fracture zones. Solid red lines represent newly-identified positive lineations, while dashed blue lines represent newly-identified negative lineations..... 100

Figure 25. Results of homogeneous model (Plouff, 1976). (A) Input magnetic anomaly measurements and polygons following topographic contours used to represent the source body. (B) Calculated magnetic anomalies from a forward model with remanent magnetization representative of an equatorial formation. (C) Calculated magnetic field from the least-squares inversion. (D) Residual magnetic field from subtracting least-square inversion model from observed magnetic anomalies. 103

Figure 26. Magnetic anomaly map(left) compared to magnetization map (right) calculated by uniform thickness model (Parker and Huestis, 1974). In left map, solid and dashed lines denote magnetic isochrons and fracture zones, respectively. Green contours show bathymetry contours for Tamu Massif at -5, -4 and -3 km. White filled black circles show the locations of ODP Site 1213 and IODP Site U1347..... 105

Figure 27. Magnetic anomaly map (left) compared to magnetization map (right) calculated by variable thickness model (Caratini Tontoni et al., 2008). Annotations are the same as those in Figure 26. 106

Figure 28. Reconstruction of tectonic evolution of Tamu Massif. (top) The counterclockwise rotation of Pacific-Farallon ridge began with the split of M21. (middle) The rotation continued between Chrons M21n and M20r, end up with the broad central positive which show a trend parallel to Pacific-Izanagi ridge. (bottom) Magnetic bights resumed regularly from M20n to M18, traversing the northern flank of Tamu Massif. Red (blue) lines denote spreading ridges during normal (reversed) geomagnetic polarity time periods, with small arrows showing the direction of seafloor spreading. Red and blue dots, annotated with "J", show the apex of the P-F-I triple junction. Dashed lines show wedge-shaped anomalies owing to ridge propagations, with small black arrows show the propagating direction. Inset map is the geomagnetic polarity time scale from Late Jurassic to Early Cretaceous (Ogg, 2012). J/K means Jurassic-Cretaceous boundary. 108

LIST OF TABLES

Page

Table 1. Magnetic surveys over Shatsky Rise..... 13

Table 2. Crossover errors (COE) statistics..... 17

Table 3. Magnetic data sources of Ori Massif. 59

Table 4. Magnetic data cruises around Tamu Massif. 93

CHAPTER I

INTRODUCTION

Oceanic plateaus are extensive and relatively flat elevations that rise more than 1 km above surrounding abyssal plains in the oceans (Sandwell and Makenzie, 1989). Generally, they cover areas greater than 0.1 million square kilometers and their volumes are usually millions of cubic kilometers. Similar to continental flood basalts (CFB), oceanic plateaus are also classified as large igneous provinces that are characterized by massive volcanic outpourings within short period of time (Coffin and Eldholm, 1994). As oceanic plateaus are believed to be derived from mantle eruptions to the Earth's surface, knowledge about the formation of these volcanoes can be important for understanding mantle dynamics and Earth history. Furthermore, compared to CFB, oceanic plateaus are less contaminated by continental materials and thus are thought to be more representative of the mantle source regions.

Oceanic plateaus are widely accepted as formed by nascent mantle plumes originating from deep mantle (Richards et al., 1989; Coffin and Eldholm, 1994). The thermal plumes are originally envisioned as isolated and not associated with the largest and linear volcanoes in the oceans, the spreading ridges (Wilson, 1963; Morgan, 1971). However, recent studies have noticed the coincidences that many oceanic plateaus formed nearby spreading ridges (Ito et al., 2003; Sager, 2005). It is surprising that two major, independent surface manifestations of mantle upwelling in the oceans appear to be linked with each other. The manner of the interactions is poorly understood.

Shatsky Rise is an oceanic plateau located in the northwest Pacific Ocean and magnetic lineations suggest its formation near the Pacific-Farallon-Izanagi triple junction during the Late Jurassic and Early Cretaceous time (Hilde et al., 1976; Sager et al., 1988; Nakanishi et al., 1999). Therefore, Shatsky Rise is an ideal site for the study of the interaction of mantle plumes and spreading ridges. Recent seismic studies concluded that the two largest edifices in Shatsky Rise, Tamu and Ori massifs, are central volcanoes which are characterized by anomalously low slopes that may be ascribed to low-viscosity and far-travelling lava flows (Sager et al., 2013; Zhang et al., 2015; Zhang et al., 2016). Magnetic isochrons were identified as across the center of Ori Massif, but poorly documented (Nakanishi et al., 1999). Tamu Massif has a more complex anomaly pattern. Its northern flanks are traversed by magnetic bights and magnetic isochrons from surrounding basins seem to extend into the flanks of this immense volcano (Nakanishi et al., 1999). More data and work are needed to understand the processes and tectonic events that shaped the pattern of magnetic anomalies.

We collected a large magnetic dataset for Shatsky Rise. Then, we constructed and modeled magnetic anomalies around Shatsky Rise to study its formation mechanism and the implications for oceanic plateau formation. Detailed studies and results are described in following chapters. Chapter II focuses on constructing a new magnetic anomaly map for Shatsky Rise. Chapter III and IV discussed the structure information of Ori and Tamu Massifs by the usage of magnetic modeling techniques. Chapter V is the summary of conclusions derived from our studies.

CHAPTER II

CORRECTION OF MAGNETIC DATA TO MAKE A MAGNETIC ANOMALY MAP FOR SHATSKY RISE

2.1 Overview

Shatsky Rise oceanic plateau was emplaced during a period of frequent geomagnetic polarity reversals, allowing reconstruction of its tectonic evolution using magnetic anomalies. Existing data indicate that it formed at a spreading ridge triple junction during Late Jurassic and Early Cretaceous time. Prior studies mainly focused on identifying magnetic isochrons and encountered difficulties in tracing magnetic lineations over high relief. We complied a large magnetic data set over Shatsky Rise and its environs, using 5.5 $x10^6$ data points from 96 geophysical cruises spanning 54 years. The long-time span and heterogeneity of component data sets made consolidation a challenge. Contributions of internal and external fields and spurious readings were removed during processing. A "backbone" method, using recent GPS-navigated data as a foundation, was developed to improve the coherency of the new data set. Ultimately, the mean and root mean square of the crossover errors (differences where tracks cross) within the new data set were reduced from 51.1 nT and 1896.8 nT to 0.1 nT and 55.5 nT. The most astounding observation from the new magnetic anomaly map is that the entire plateau and surrounding crust is characterized by linear anomalies; plateau morphology has little effect. Of particular importance, linear anomalies were found at the centers of high edifices, implying that they formed at spreading ridges. Nevertheless, the anomalies

also imply complex tectonics related to the triple junction. Tamu Massif apparently formed by the rotation of a segment of Pacific-Farallon spreading ridge by 90° as the triple junction moved through the edifice. Ori Massif appears to have formed on the Pacific-Izanagi ridge between triple junctions. Shirshov Massif contains discordant lineations that may indicate a rotated microplate. These findings do not support the formation of plateau edifices by central eruptions of far-ranging lava flows. Instead, the edifices must have formed by spreading analogous to mid-ocean ridges with limited lateral extent of eruptions.

2.2 Introduction

Oceanic plateaus are common submarine constructions, covering an area of approximately 5.11% of the ocean basins all over the world (Harris, 2014). Most are basaltic mountains, classified as large igneous provinces and are thought to be the oceanic counterpart of continental flood basalts (Richards et al., 1989). The formation mechanisms and evolution of these enormous volcanoes is still enigmatic. One difficulty is that they are remote and massive thus difficult to sample and often characterized by a small amount of data. Moreover, different formation hypotheses have been developed and each has gained partial support from limited geological and geophysical data. Two widely-cited but contrasting formation mechanisms are the plume model and the plate model. The plume model postulates a large amount of hot material arising from the deep mantle (the plume head). When this plume head arrives at the base of the lithosphere, it spreads out and causes enormous melt and eruptions (Richards et al., 1989; Duncan and

Richards, 1991; Campbell and Griffiths, 1992; Coffin and Eldholm, 1994). Whereas, the plate model states that voluminous volcanism can be attributed to decompression melting of anomalously fertile (lower melting temperature) mantle in response to lithospheric extension (Foulger, 2002; Foulger and Anderson, 2005; Foulger, 2007; Anderson and Natland, 2014).

Linear magnetic anomalies (aka "magnetic lineations") are created by a combination of seafloor spreading and geomagnetic field reversals (Vine and Matthews, 1963; Vine, 1966). As recorders of past positions of mid-ocean ridges and seafloor isochrons, they play an important role in understanding the tectonic history of ocean basins. Unfortunately, many oceanic plateaus formed during the Cretaceous Quiet Period (Cretaceous Long Normal Superchron), a ~35-Myr period without magnetic reversals (Ogg, 2012), so that linear magnetic anomalies cannot be used in the reconstruction of their tectonic evolution. In contrast, Shatsky Rise is unusual because it is a large plateau formed during Late Jurassic and Early Cretaceous time, a time when the magnetic field experienced polarity reversals and linear magnetic anomalies were recorded at mid-ocean ridges (MOR). These magnetic lineations indicate that Shatsky Rise is formed nearby a triple junction of spreading ridges, so it can give clues about hotspot-ridge interaction (Sager et al., 1988; Nakanishi et al., 1999).

Previous magnetic studies over Shatsky Rise focused on identifying magnetic isochrons that reveal the tectonic history of this huge submarine mountain range (Mammerickx and Sharman, 1988; Sager et al., 1988; Sharman and Risch, 1988; Nakanishi et al., 1989, 1999, Nakanishi et al., 2015). These studies all relied on manual

picking of magnetic anomaly peaks. This is subjective and difficult for sparse datasets. Furthermore, tracing magnetic anomaly peaks provides limited information about volcanic history and the magnetic structure of the oceanic plateau. In contrast, the creation of a magnetic anomaly map is a more objective process because it is not dependent on subjective tracing or the assumption that a feature is an isochron. Furthermore, the pattern of magnetic anomalies can be interpreted as structural information helping to understand how a basaltic volcano was formed (e.g., Sager et al., 1993; Sager et al., 2005). Moreover, 19 years have elapsed since last systematic study of the magnetic anomaly data over and around Shatsky Rise (Nakanishi et al., 1999). New data have been collected with modern magnetometers and precise Global Positioning System (GPS) navigation. These factors suggest that a reexamination of the magnetic anomalies around and within Shatsky Rise is warranted.

Although magnetic data are important for understanding tectonic evolution, their correction and compilation offers many difficulties owing to the constant changes of the magnetic field and challenges of older datasets. A sea-surface magnetic measurement combines a series of superimposed multi-source magnetic fields. Furthermore, the geomagnetic field varies with time. Several recent studies of global magnetic datasets discussed systematic and rational development about corrections of magnetic data (Chandler and Wessel, 2008; Quesnel et al., 2009; Maus et al., 2009; Chandler and Wessel, 2012). They noticed the inconsistent usage of various geomagnetic reference fields to calculate marine magnetic anomalies and the lack of details about cancellation

of external fields in most surveys. These problems are likewise not solved in previous magnetic studies of Shatsky Rise.

Here, we collected new magnetic data obtained since Nakanishi et al. (1999) and compiled these data with prior data using systematic corrections to derive a new magnetic anomaly map focused on Shatsky Rise. This new map gives insights into the formation of the rise. Surprisingly, the magnetic anomalies are mostly linear and show little correlation to the rise bathymetry, suggesting that the large edifices have little effect on the pattern of magnetic anomalies.

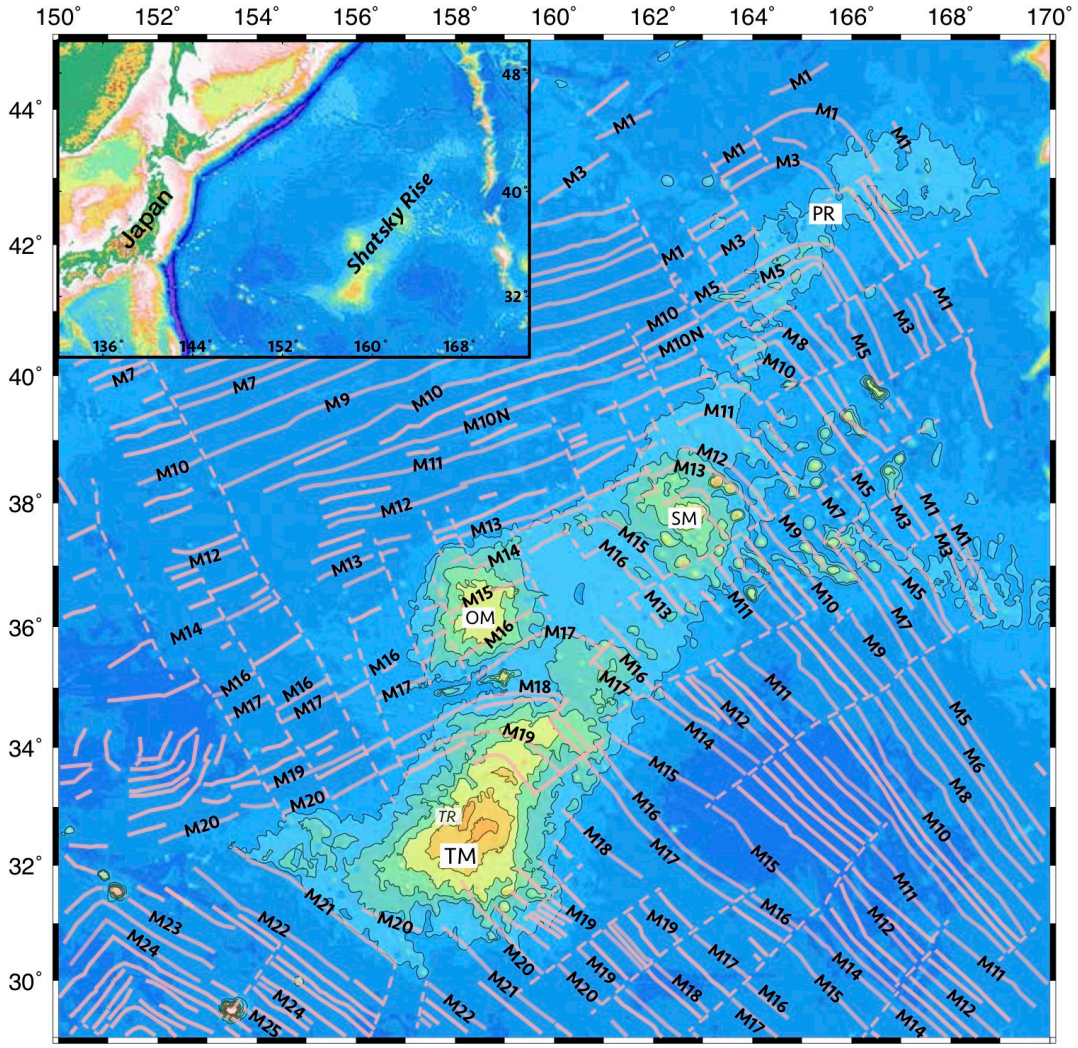

Figure 1. Shatsky Rise location, bathymetry and magnetic lineations. TM=Tamu Massif, TR=Toronto Ridge, OM=Ori Massif, SM=Shirshov Massif, PR=Papanin Ridge. Inset map shows the location of Shatsky Rise in the northwest Pacific Ocean. Shatsky Rise bathymetry (Smith and Sandwell, 1997) shallower than -5 km is depicted with contours at 0.5-km intervals. Pink heavy lines denote magnetic lineations and fracture zones (Nakanishi et al., 1999).

2.2.1 Geological setting of Shatsky Rise

Shatsky rise is a large submarine mountain range, located approximately 1,000 miles east of Japan in the northwest Pacific Ocean. It consists of three high edifices (Tamu, Ori and Shirshov massifs), one low volcanic ridge (Papanin Ridge) and a cluster of seamounts (Ojin Rise Seamounts) (Fig. 1). Radiometric dating and magnetic isochrons both imply that Shatsky Rise is an oceanic plateau formed at Late Jurassic and Early Cretaceous time (Sager et al., 1988, 1999; Nakanishi et al., 1999; Mahoney et al., 2005; Geldmacher et al., 2014; Tejada et al., 2016).

Recently, Integrated Ocean Drilling Program (IODP) Expedition 324 recovered significant amounts of igneous rocks from Shatsky Rise and focused on understanding its formation (Sager et al., 2016). Tamu Massif is characterized by thick massive lava flows similar to those found in Ontong Java Plateau and continental flood basalts, likely formed by extraordinarily extensive eruptions. In contrast, at Ori Massif, the massive flows become thinner and eruptive material is mostly pillow lavas (Sager et al., 2011a, 2011b; Sager et al., 2013), and at Shirshov Massif, only pillow lavas were cored (Sager et al., 2011a). This finding is consistent with the size and age progression from southwest to northeast of Shatsky Rise, suggested by bathymetric and magnetic data (Nakanishi et al., 1999; Sager et al., 1999), implying that the volcanism diminished with time (Sager et al., 2016). Core samples in Shatsky Rise mostly share similar geochemical and isotopic signatures with mid-ocean ridge basalts (MORB) (Mahoney et al, 2005; Sano et al., 2012). Whereas, these samples are different from normal MORB

(N-MORB) as they are enriched in incompatible elements and were formed at greater depth and at a higher degree of partial melting (Sano et al., 2012; Heydolph et al., 2014).

The internal structure of Shatsky Rise was further studied with the help of two seismic surveys – MGL1004 and MGL1206. Refraction data across Tamu Massif imply that the thickest part of the crust is up to ~30 km thick. But a negative correlation was discovered between crustal thickness and seismic velocity, postulated to result from a cool and chemically heterogeneous source mantle (Korenaga and Sager, 2012). Multichannel seismic data show subparallel intra-basement reflectors trending downhill from the center of Tamu and Ori Massifs, which are thus interpreted as central volcanoes. However, the slope of these intra-basement reflectors and the basement interface is abnormally low, interpreted as a result of low-viscosity and long-runout sheet flows (Sager et al., 2013; Zhang et al., 2015). Moho structure constructed from multichannel reflection and wide-angle refraction data also implies thickened crust beneath Tamu Massif, Ori Massif and the basins in between. Additionally, the Moho geometry indicates that Tamu and Ori Massifs are in nearly complete Airy isostasy, in keeping with the nearly zero free-air gravity anomalies over Shatsky Rise (Sandwell and Smith, 1997; Zhang et al., 2016).

Magnetic isochrons show that SW-NE trending Japanese lineations and NW-SE trending Hawaiian lineations converge at Shatsky Rise, forming magnetic bights that indicate the paleo-locations of Pacific-Farallon-Izanagi (P-F-I) triple junction (Larson and Chase, 1972; Sager et al., 1988; Nakanishi et al., 1989, 1999) (Fig. 1). The triple junction migrated northeast along the axis of Shatsky Rise and jumped at least nine

times during the emplacement of the Rise (Nakanishi et al., 1999). In addition, irregularities of magnetic isochron spacing within Shatsky Rise were interpreted as evidence of microplates (Sager et al., 1988; Nakanishi et al., 1999). Magnetic modeling of the anomaly over Tamu Massif implied that this edifice formed during a single, long period of reversed-polarity (M17r), with rapid and massive eruptions at a rate analogous to continental flood basalts (Sager and Han, 1993). However, several magnetic isochrons southeast of Tamu Massif extend toward its center and magnetic bights cut across the northern flank (Sager et al., 1988; Nakanishi et al., 1999), which cannot be reconciled with the idea of rapid eruptions. Furthermore, Ori Massif is also traversed by isochrons M16-M14, not supporting the idea of rapid formation by only one massive magma pulse (Nakanishi et al., 1999). These findings are additionally not in good agreement with conclusions of the seismic studies, that Tamu and Ori Massif formed as central volcanoes.

2.3 Data and Methods

2.3.1 Magnetic data

The compiled magnetic dataset for Shatsky Rise contains 5,475,524 data points from 96 magnetic surveys, totaling ~256,395 km in track line length (Table 1). It contains 79 surveys obtained from the National Centers for Environmental Information (NCEI), 16 surveys from Japanese sources provided by Masao Nakanishi, and 1 recent magnetic survey focusing on Tamu Massif (cruise FK151005). Spanning from 1961 to 2015, collected over 5 decades, the new dataset exhibits inconsistency between different

surveys. Notably, this compilation adds 10 recent surveys accurately positioned with Global Positioning System (GPS) satellite navigation (Fig. 2). This is in contrast to most of the older cruises, which were navigated by inaccurate or less precise navigation systems including celestial, Loran, and Doppler satellite navigation (Table 1). Because these data virtually eliminate navigation errors common in older cruises, the new GPS-navigated data can be used as a "backbone" to remove navigational offsets in older cruises (section 2.2.4).

Figure 2 shows that marine magnetic measurements are heterogeneously distributed. Most data are concentrated over the three massifs and the seamounts east of Shirshov Massif (Ojin Rise seamounts). Data are concentrated over Tamu massif partly because of the addition of the recent magnetic surveys. Of particular note is the R/V *Falkor* cruise FK151005, which collected 1,897,065 data points in a grid of 17 transects across Tamu Massif. Elsewhere data are relatively sparse with large gaps in between ship tracks. This uneven distribution results in poor definition of magnetic anomalies in places, with uncertainty in later interpretation of the magnetic anomaly trends and connections.

Table 1. Magnetic surveys over Shatsky Rise.

Cruise ID	N	LS (km)	Year	*Ship*	Source Institute[1]	Navi[2]
JPYN02BD	1592	3548.4	1961	*Spencer F. Baird*	Scripps Institution of Oceanography	C
JPYN04BD	63	144.2	1961	*Spencer F. Baird*	Scripps Institution of Oceanography	C
LUSI01AR	878	2009.6	1962	*Argo*	Scripps Institution of Oceanography	C
JD08	932	3776.6	1964	*unknown*	Kobe University	U
V2006	415	1626.5	1964	*Vema*	Lamont-Doherty Geological Observatory	C
V2106	149	738.8	1965	*Vema*	Lamont-Doherty Geological Observatory	C
V2110	639	2835.5	1965	*Vema*	Lamont-Doherty Geological Observatory	C
RC1007	546	2476.2	1966	*Robert D. Conrad*	Lamont-Doherty Geological Observatory	U
RC1008	628	2961.3	1966	*Robert D. Conrad*	Lamont-Doherty Geological Observatory	U
ZTES03AR	2306	6338.4	1966	*Argo*	Scripps Institution of Oceanography	C
ZTES04AR	15	25.4	1966	*Argo*	Scripps Institution of Oceanography	C
ZTES05AR	721	1852	1966	*Argo*	Scripps Institution of Oceanography	C
RC1108	566	2510.4	1967	*Robert D. Conrad*	Lamont-Doherty Geological Observatory	D
OCEA68	695	4872.1	1968	*unknown*	Kobe University	U
POL6829	1507	4424.4	1968	*Surveyor*	NOAA	D
RC1207	470	1633.2	1968	*Robert D. Conrad*	Lamont-Doherty Geological Observatory	D
DSDP06GC	1387	2363	1969	*Glomar Challenger*	Scripps Institution of Oceanography	D
HUNT03HT	929	1336.6	1969	*Hunt*	Scripps Institution of Oceanography	C
RC1219	3102	5370.8	1969	*Robert D. Conrad*	Lamont-Doherty Geological Observatory	D
SCAN03AR	2375	4862.4	1969	*Argo*	Scripps Institution of Oceanography	D
SILS01BT	1388	2457	1969	*Silas Bent*	Scripps Institution of Oceanography	C
SILS02BT	3287	4895.3	1969	*Silas Bent*	Scripps Institution of Oceanography	C
70042205	46	305.5	1970	*Mahi*	University of Hawaii	D
ANTP03MV	2400	3863.3	1970	*Melville*	Scripps Institution of Oceanography	D
POL7004	3939	10153.6	1970	*Oceanographer*	NOAA	D
ARES05WT	991	1671.9	1971	*Thomas Washington*	Scripps Institution of Oceanography	D
ARES07WT	1116	2596.2	1971	*Thomas Washington*	Scripps Institution of Oceanography	D
DSDP19GC	25	41.4	1971	*Glomar Challenger*	Scripps Institution of Oceanography	D
RC1405	1594	2902.8	1971	*Robert D. Conrad*	Lamont-Doherty Geological Observatory	D
SI932005	23643	9999.1	1971	*Silas Bent*	US Naval Oceanographic Office	D/L
POL7201	190	480.3	1972	*Oceanographer*	NOAA	D
RF72	98	356.9	1972	*unknown*	Kobe University	U
SI932009	18781	10015.8	1972	*Silas Bent*	US Naval Oceanographic Office	D/L
SI933001	193	409.3	1972	*Silas Bent*	US Naval Oceanographic Office	D/L
SI933010	1571	3127.6	1972	*Silas Bent*	US Naval Oceanographic Office	D/L
73102500	16	50	1973	*Kana Keoki*	University of Hawaii	D
DSDP32GC	1919	2974.5	1973	*Glomar Challenger*	Scripps Institution of Oceanography	D
GECS-CMV	1330	2040.8	1973	*Melville*	Scripps Institution of Oceanography	D
GECS-DMV	1541	1973.5	1973	*Melville*	Scripps Institution of Oceanography	C/L
KH74-02	1974	5383.8	1974	*Hakuho-Maru*	The University of Tokyo	D
KH74-04	979	2597.6	1974	*Hakuho-Maru*	The University of Tokyo	D
75072600	214	1107.9	1975	*Kana Keoki*	University of Hawaii	D
V3212	982	2372.2	1975	*Vema*	Lamont-Doherty Geological Observatory	D
V3213	278	404.5	1975	*Vema*	Lamont-Doherty Geological Observatory	D
76080601	1883	653.4	1976	*Kana Keoki*	University of Hawaii	D
76080602	7995	2429.2	1976	*Kana Keoki*	University of Hawaii	D
GH7602	38	56.5	1976	*Hakurei Maru*	Geological Survey of Japan	U
INDP01WT	1116	1956.5	1976	*Thomas Washington*	Scripps Institution of Oceanography	D

Table 1. Continued.

L876NP	4	17.2	1976	*Samuel P. Lee*	USGS Branch of Pacific Marine Geology	D/L
RC2004	1362	1422.9	1976	*Robert D. Conrad*	Lamont-Doherty Geological Observatory	D
RC2005	702	544.5	1976	*Robert D. Conrad*	Lamont-Doherty Geological Observatory	D
SI343615	1068	395.5	1976	*Silas Bent*	US Naval Oceanographic Office	D/L
SI343625	1023	391.1	1976	*Silas Bent*	US Naval Oceanographic Office	D/L
V3311	994	875.3	1976	*Vema*	Lamont-Doherty Geological Observatory	D
77031705	15413	5333.5	1977	*Kana Keoki*	University of Hawaii	D
DSDP55GC	1217	2460.6	1977	*Glomar Challenger*	Scripps Institution of Oceanography	D
GH771-C	199	432.1	1977	*Hakurei Maru*	Geological Survey of Japan	D
GH7801	40	97.4	1978	*Hakurei Maru*	Geological Survey of Japan	U
GH7901	112	797.5	1979	*Hakurei Maru*	Geological Survey of Japan	U
GH801-A	158	636.9	1980	*Hakurei Maru*	Geological Survey of Japan	D
GH801-B	372	774.1	1980	*Hakurei Maru*	Geological Survey of Japan	D
GH805-A	169	365.8	1980	*Hakurei Maru*	Geological Survey of Japan	D
GH805-B	3	4	1980	*Hakurei Maru*	Geological Survey of Japan	D
RAMA03WT	253	464.2	1980	*Thomas Washington*	Scripps Institution of Oceanography	D
RAMA04WT	897	2269.5	1980	*Thomas Washington*	Scripps Institution of Oceanography	D
V3612	3665	5671.7	1980	*Vema*	Lamont-Doherty Geological Observatory	D
GH814-B	288	605.3	1981	*Hakurei Maru*	Geological Survey of Japan	D
RAMA13WT	567	962.7	1981	*Thomas Washington*	Scripps Institution of Oceanography	D
DSDP86GC	3230	4386.2	1982	*Glomar Challenger*	Scripps Institution of Oceanography	D
DSDP88GC	1504	1938.1	1982	*Glomar Challenger*	Scripps Institution of Oceanography	D
DSDP88N	1403	956.6	1982	*Desteiguer*	NORDA	D
KH82-05	362	2397.6	1982	*Hakuho-Maru*	The University of Tokyo	D
MG21	1603	5247.4	1982	*Morskoy Geofizik*	Institute of Marine Geology/Geophysics	D
85002211	10261	3532.4	1985	*Jean Charcot*	University of Hawaii	D
MG28	1501	4166.7	1985	*Morskoy Geofizik*	Institute of Marine Geology/Geophysics	D
PG30	4236	9327.2	1985	*Pegas*	Institute of Marine Geology/Geophysics	D
DELP86KA	667	2064.5	1986	*Wakashio-Maru*	Chiba University	D/L
DELP86WA	1196	3023.9	1986	*Wakashio-Maru*	Chiba University	D/L
KH88-03	12066	5529	1988	*Hakuho-Maru*	The University of Tokyo	D
RNDB10WT	2589	795.7	1988	*Thomas Washington*	Scripps Institution of Oceanography	D
KH89-02	4518	2403.8	1989	*Hakuho-Maru*	The University of Tokyo	D
ODP132JR	4660	1431.8	1990	*JOIDES Resolution*	Texas A&M University	G/L
ODP145JR	1863	730.3	1992	*JOIDES Resolution*	Texas A&M University	G/L
KH93-01	2534	1847	1993	*Hakuho-Maru*	The University of Tokyo	G
TN037	27058	5729.6	1994	*Thomas G. Thompson*	Texas A&M University	G
KH96-03	15975	2779.5	1996	*Hakuho-Maru*	The University of Tokyo	G
MR99-K04*	264413	2022.9	1999	*Mirai*	JAMSTEC	G
ODP197JR*	6557	4122	2001	*JOIDES Resolution*	Texas A&M University	G
ODP198JR*	10036	3515.2	2001	*JOIDES Resolution*	Texas A&M University	G
KH06-01*	1863	348.7	2006	*Hakuho-Maru*	The University of Tokyo	G
YK08-09*	46772	6824.2	2008	*Yokosuka*	The University of Tokyo	G
EXP324*	9825	3192.5	2009	*JOIDES Resolution*	Texas A&M University	G
MR08-06*	6479	418.6	2009	*Mirai*	JAMSTEC	G
MGL1004*	2448587	10243.7	2010	*Marcus G. Langseth*	Lamont-Doherty Earth Observatory	G
MGL1206*	558753	1494.7	2012	*Marcus G. Langseth*	Lamont-Doherty Earth Observatory	G
FK151005*	1897065	8420.5	2015	*Falkor*	Schmidt Ocean Institute	G
Totals	5475524	256394.3				

Table 1. Continued.

*Data not used by Nakanishi et al. (1999). N=total number of data point; LS=total length of each survey; Navi=Navigation. [1]Institute codes: NOAA=National Oceanic and Atmospheric Administration; NORDA=Naval Ocean Research and Development Activity; IPEAS=Institute Physics of the Earth Academy of Science; JAMSTEC=Japan Agency for Marine-Earth Science and Technology. [2]Navigation codes: C=Celestial; L=Long Range (radio) Navigation; D=Doppler Satellite; G=Global Positioning System; U=unknown.

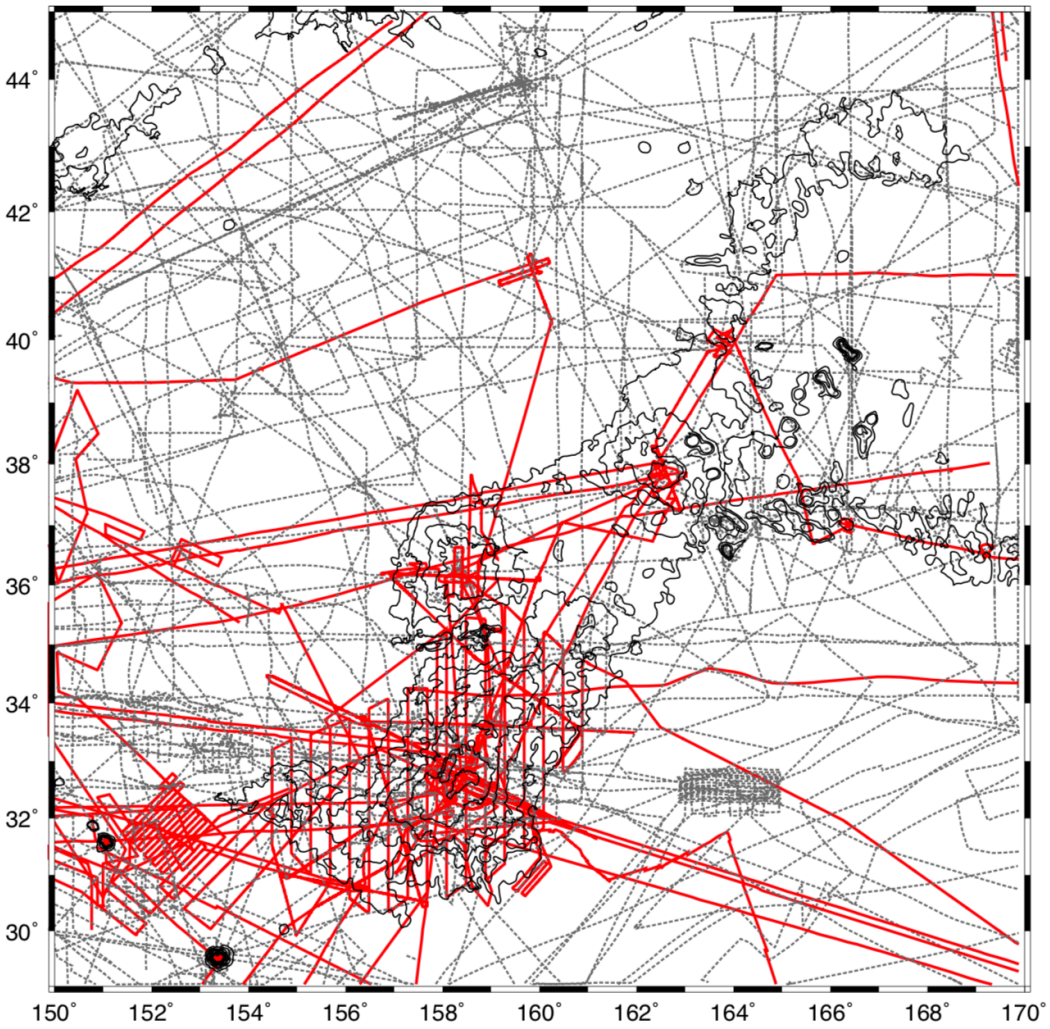

Figure 2. Chart of magnetic ship tracks over and around Shatsky Rise. Dashed black lines show older cruises positioned with navigation other than GPS. Solid red lines denote surveys positioned with GPS. Thin black contours represent Shatsky Rise bathymetry shallower than -5 km, contoured at 0.5-km intervals.

2.3.2 Data processing

To study the tectonic evolution of oceanic crust, we are interested in the geomagnetic field recorded in the crust, i.e., "crustal field". Therefore, the contributions of other fields (core and external) must be removed. Moreover, the data set contains numerous sources of noise that must be removed to reduce inconsistency between different surveys and improve anomaly definition. Crossover errors (COE), which are data offsets between intersecting ship tracks, are used as indicators of the error budget to evaluate the coherency of the dataset. Furthermore, the mean and root mean square of crossover errors ($Mean_{COE}$ and RMS_{COE}) are used to estimate improvement of each correction step. If anomalies are assumed evenly distributed between positive and negative values, $Mean_{COE}$ should be zero, whereas smaller values of RMS_{COE} indicate lesser variance.

Before considering spurious signals in measured total field (TF) values, a thorough review of each survey data file is necessary. This first step focuses on finding incorrect entries such as records with non-increasing or decreasing time series. Thereafter, we found that some surveys with many turns show large COE while others with fewer are often better. This likely indicates that cruises using Doppler satellite navigation had positions between fixes estimated by dead reckoning, which can be difficult with turns. Thus, cruises with high COE were sometimes separated into straight segments for the convenience of later corrections such as the 'backbone' method and the correction of navigation errors. Ultimately, 96 surveys were divided into 317 segments.

Furthermore, considering the width of magnetic lineations (~10-20 km) in our study areas, some recent surveys with measurements at 1-sec intervals, are oversampled. These data sets were decimated to retain data points at 1-min interval. This corresponds to spatial sampling at ~300 m intervals at a cruising speed of 10 kt. After this decimation, the total number of processed measurements was greatly reduced, totaling 344,681 (Table 2 Case I).

Table 2. Crossover errors (COE) statistics.

Case	$N_{Records}$	N_{COE}	N_{COE} > 100 nT	$Mean_{COE}$ (nT)	RMS_{COE} (nT)	Remarks
I	344681	6095	615	51.1	1896.8	IGRF
II	334445 (-2.9%)	5655	489	12.8	88.6	Outliers and noise
III	334445	5655	390	5.2	83.1	CM4
IV	331936 (-0.8%)	5597	374	4.9	81.2	Kp
V	328429 (-1.0%)	5344	156	0.1	55.5	Backbone

Abbreviations: $N_{Records}$=total number of processed data, N_{COE}=total number of crossover errors, $Mean_{COE}$=mean of crossover errors, RMS_{COE}=root mean square of crossover errors, IGRF=international geomagnetic reference model (e.g., Finlay et al., 2011), CM4=comprehensive model 4 (Sabaka et al., 2004).

2.3.2.1 Removal of internal field

Before dealing with outliers and noise, we first used IGRF11 (Finlay et al., 2010) to remove the contribution of internal field because TF values are around 40,000 nT while anomaly values average about 0 and thus are much easier for plotting and visual inspections. The $Mean_{COE}$ and RMS_{COE} of the initial magnetic anomalies are 51.1 nT and 1896.3 nT (Table 2). Fig. 3A shows the distribution of COE within the range of ±300 nT. Only ~2% (127) of the COE are out of the range. The histogram shows that 40, 25 and 10% of the COE are larger than 25, 50, 100 nT, respectively. Our processing steps aimed to reduce these percentages.

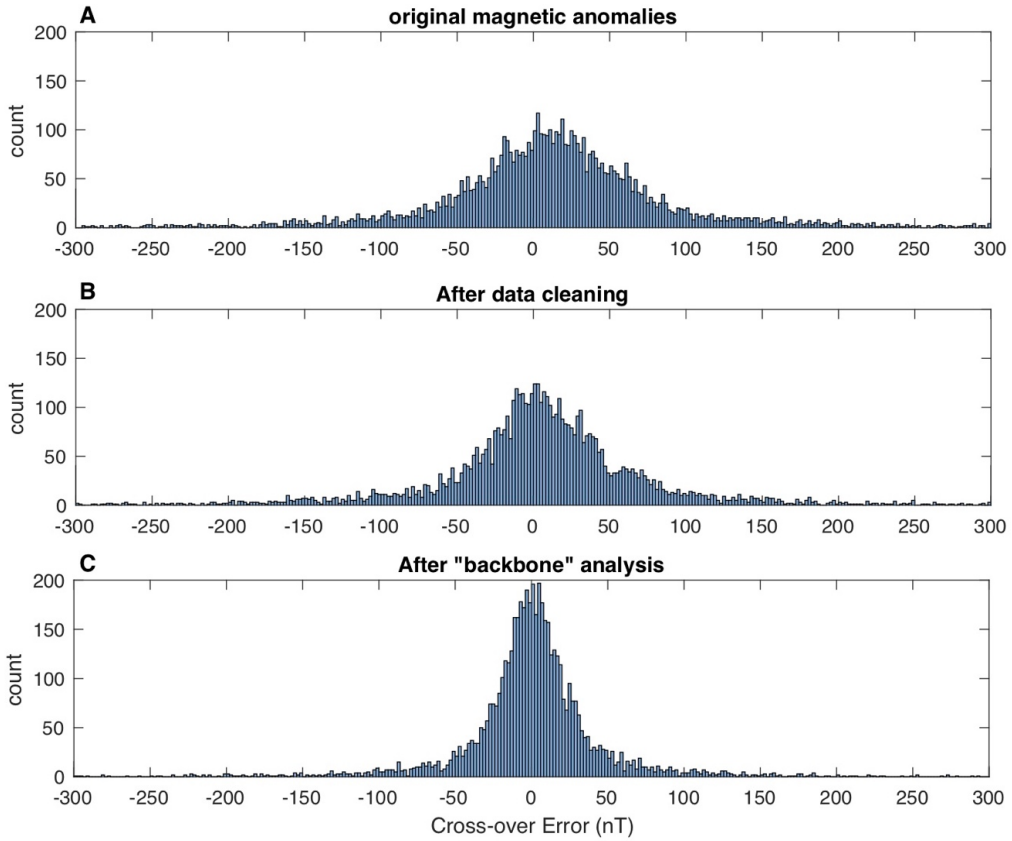

Figure 3. Histogram showing the distribution of magnetic anomaly COE after particular correction steps. (A) COE distribution after just removing internal field (IGRF) contribution. (B) COE distribution after removing outliers & noise and removing external fields (CM4 and Kp). (C) COE distribution after improving data set consistency by 'backbone' analysis. RMS error values are given in Table 2.

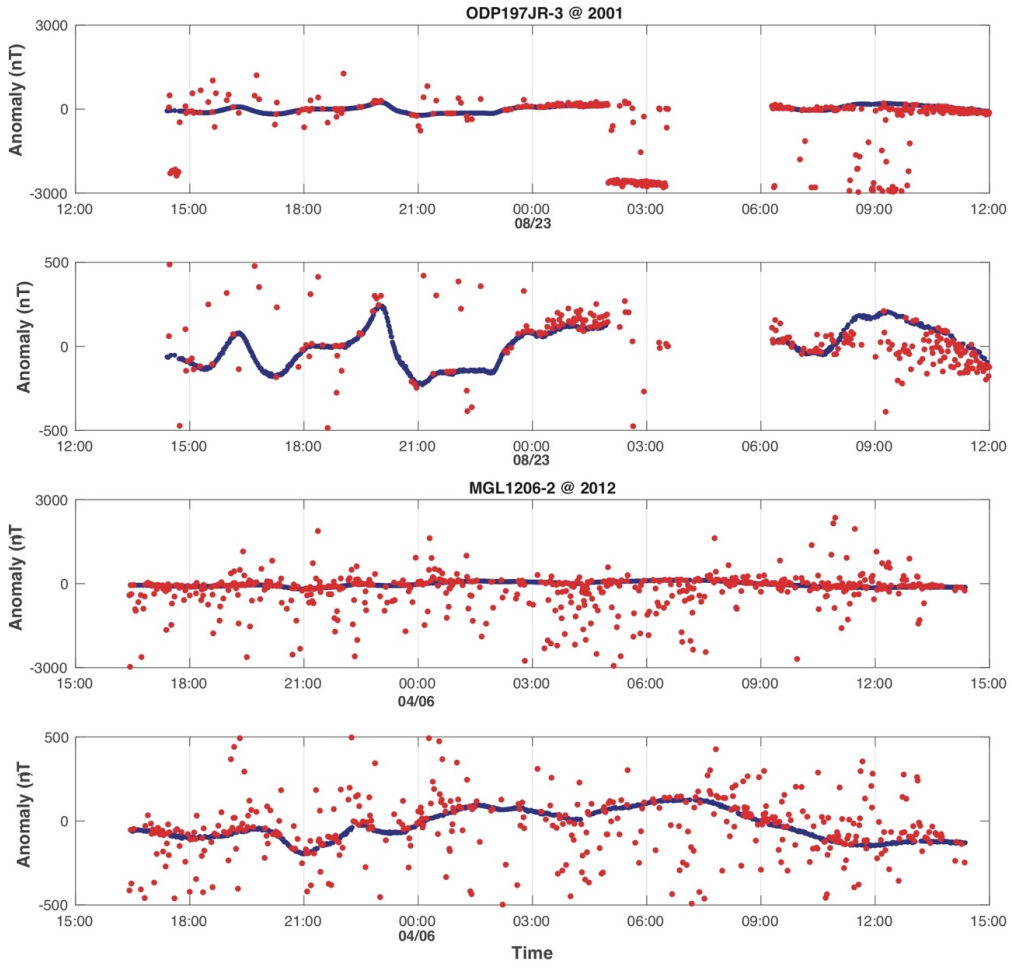

Figure 4. Examples of data with outliers and noise. Deleted outliers and noise are plotted as red points while retained data are represented by blue points.

2.3.2.2 Deleting Outliers and noise

A range of -1500 nT to 1500 nT was set as a threshold of reasonable anomaly values. Anomalies outside of this range were deleted. Since some useful high-gradient anomalies overlap in frequency with noise, filtering is rarely an appropriate way to identify and eliminate noise. Our data processing routine sought to keep as many original measurements as possible. Thus, filtering was not used for removing noise.

Instead, outliers and noise were identified by visual inspections of plots of the time series profiles (Fig. 4) and removed manually.

This first stage visual inspection can only delete visually-obvious outliers and noise. During later correction steps in which COE is adopted to evaluate the quality of survey segments, outliers and noise are sometimes inspected as related to large COE and were deleted (e.g., Fig. 5). This iteration of removal of outliers and noise is necessary as it is impossible to completely clean the dataset, eliminating all outliers and noise.

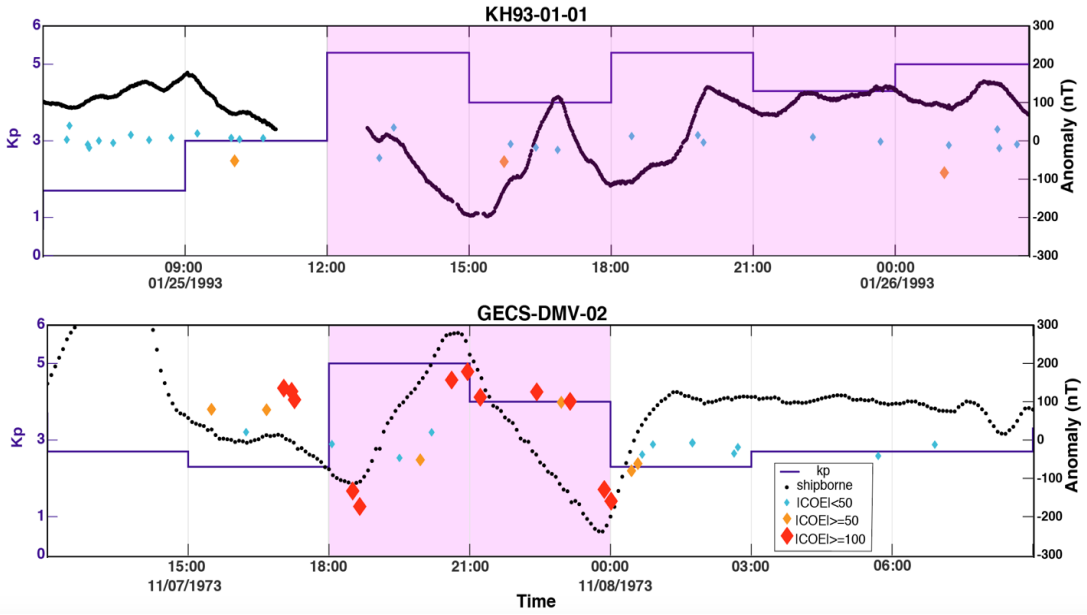

Figure 5. Influence of magnetic storms when Kp ≤ 5. (Upper) High Kp values without apparent disturbance to shipborne data. (Lower) High Kp values with obvious disturbances to shipborne data. Shipborne data are plotted as black dots. Kp values (given at 3-hour intervals) are plotted as the purple curve and disturbed time periods are denoted by shaded areas. Crossover errors (COE) are denoted as blue, orange, and red diamonds with color based on the magnitude. COE are plotted vertically on the same scale as anomaly values.

2.3.2.3 Removal of external fields

Using observatory data as well as satellite measurements from POGO, Magset, Orsted and CHAMP, the Comprehensive Model 4 (CM4, Sabaka et al., 2004) provides good estimates for magnetic fields and their temporal variations from 1960 to July 2002. Because of the time limit, it is outdated for recent survey data. To avoid inconsistencies produced by the usage of different models, for the internal/core field, we only used IGRF11. CM4 was, however, useful for removing quiet day external fields, including the fields originating from the ionosphere and magnetosphere as well as induced fields in the Earth's electrically conducting interior. By updating two main parameters (the DST and 10.7 indices) used to estimate the external fields, it is possible to extend the use of CM4 for the entire dataset.

According to former studies, CM4 produces relatively reasonable predictions for quiet days and moderately disturbed days ($Kp \leq 5.0$), but not for disturbed days (with Kp index > 5.0) (Onovughe and Holme, 2015). Geomagnetic observatory records show that the influence of magnetic storms last for approximately one to four days (Love and Remick, 2007). Even if we deleted shipborne magnetic data obtained one day after the disturbed time, 34,007 data points, ~9.9% of the whole dataset, would be removed, which is not desirable. Furthermore, according to visual inspection of the anomaly map, some disturbed-day anomalies are in good agreement with surrounding data, defining reasonable positive and negative lineations. Ultimately, with the help of COE, we did visual inspection of disturbed-day shipborne data and only deleted suspicious parts that appear to be noise and related to high COE (Fig. 5).

Figure 3B shows the distribution of all COE within the range of ±300 nT after deleting outliers and noise and removing contribution of external fields. Compared to the initial distribution of magnetic anomalies (Fig. 3A), it shows a concentration of COE within the range of ±100 nT and COE became more symmetric around 0. Indeed, the $Mean_{COE}$ reduced from -51.1 nT to 4.9 nT, showing that the corrections made the data set more symmetric. The percentages of COE larger than 25, 50, 100 nT are improved from 40, 25 and 10% to 32, 18 and 7%.

2.3.2.4 Improvement of dataset inconsistency

COE statistics show that the magnitude of COE is highly correlated to the year that the survey was carried out. We propose that this mainly arises from inaccurate navigation systems used in older surveys and their improvement over time. A significant change occurred with the switch to full-time GPS navigation because this system is highly accurate and produces closely spaced positional fixes, so the need for dead reckoning between fixes was eliminated. This switch occurred during the late 1980s. Therefore, the data set contains well-positioned data during the GPS era and poorly positioned data beforehand. We developed a "backbone" analysis in which the GPS-positioned survey data are merged as a "backbone" dataset because these data should not display differences owing to poor navigation. Subsequently, older and low-quality survey segments that show large COE were merged to the "backbone" by shifting data of each survey segment by a constant offset, which is the $Mean_{COE}$ of certain segment

versus the “backbone”. This is achieved by the use of the “x2sys” package in the GMT suite (Wessel, 2010). The backbone grew as more and more corrected data were added.

The constant amplitude shift of old cruises in order to fit the “backbone” fail to effectively merge older cruises carried out in the 1960s into the “backbone”. The tracks of these cruised are still visible in the anomaly map, disturbing the anomaly pattern. Accordingly, RMS_{COE} of these much older cruises are usually larger than 100 nT. The cause of these offsets is likely incorrect positioning owing to archaic navigation. To correct these navigation errors, we assumed there to be a constant lateral offset for a given straight-line segment and moved this segment around its recorded longitude and latitude within a limited range of x, y offsets. The best fit offset was determined as the x and y shift that produced the lowest COE where the segment crossed other survey data. It is impossible to uniquely and precisely recover the real position of the surveys because the offset may be variable along the track and because there are limited track crossings. However, a significant improvement of the COE demonstrates that this method is effective in reducing the data error budget (Table 2 case V).

Improvement of the “backbone” method is clearly shown in the histogram in Figure 3C. The $Mean_{COE}$ reduced from 4.9 nT to 0.1 nT and the RMS_{COE} shows improvement from 81.2 nT to 55.5 nT (Table 2). With this correction the straight-line artifacts that showed the tracks of poorly-navigated cruises became almost invisible in the anomaly map (Figs. 6, 7). This correction step lowered the percentages of COE higher than 25, 50, 100 nT from 32, 18 and 7% to 17, 7 and 2%.

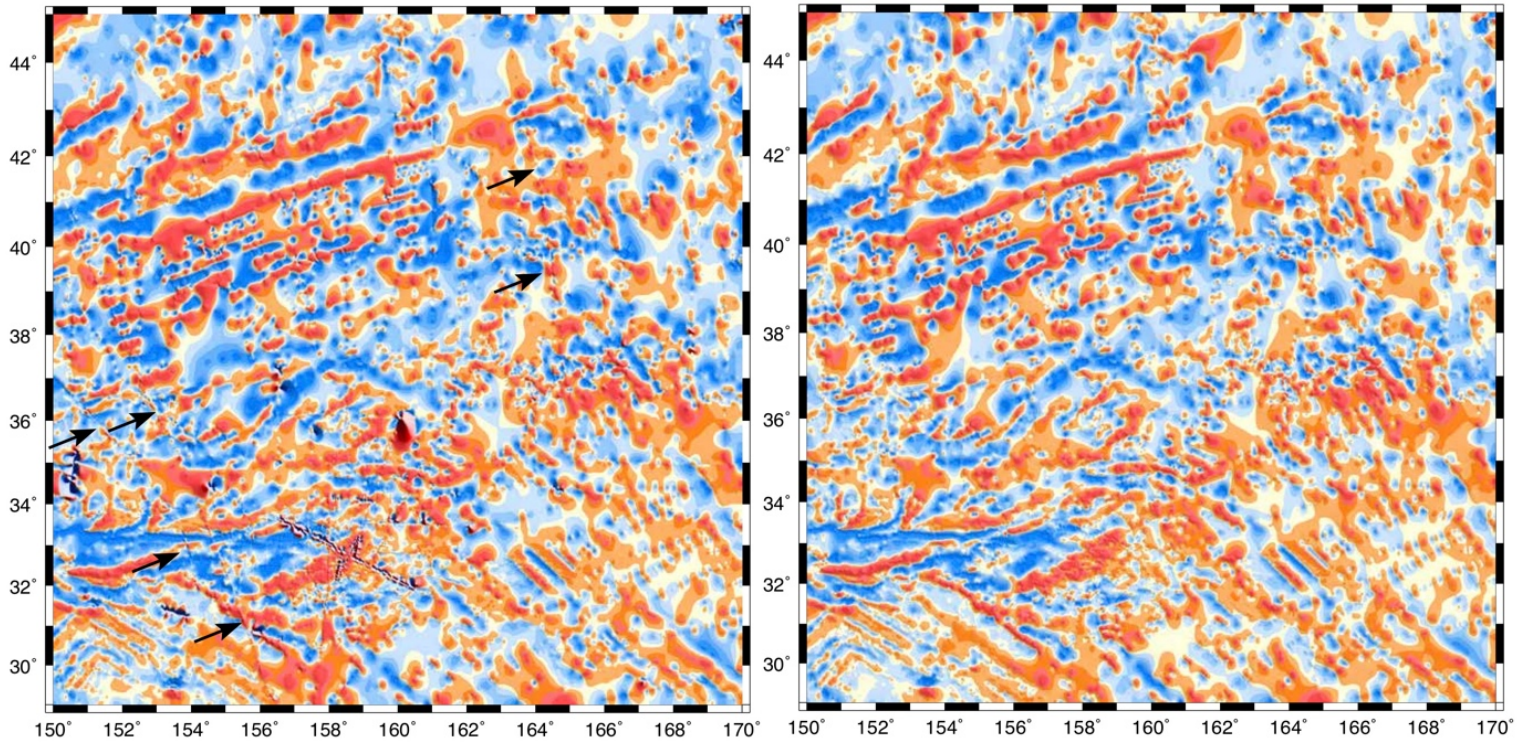

Figure 6. Effect of manual navigation corrections. Plots are 1 arc-minute gridded magnetic anomaly maps. Black arrows indicate the artifacts (trails) caused by poorly-navigated surveys that disrupt the map pattern. Improvement from navigation corrections are noticeable in the resulting map (right).

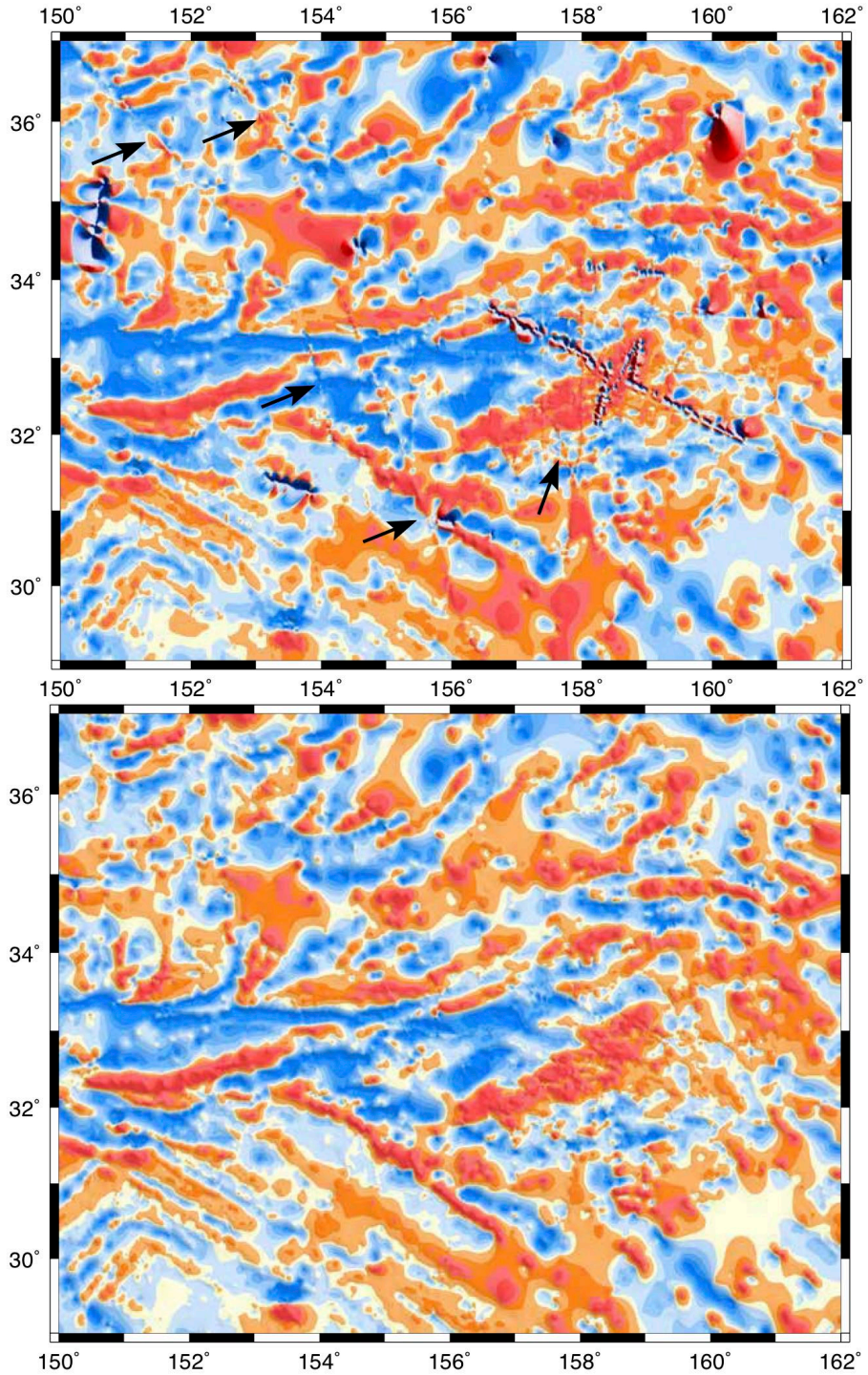

Figure 7. Detail on effect of manual navigation corrections. Plots are following Figure 6, but show a smaller region, illustrating the improvement in the southwest part of our study area.

2.4 Results

The magnetic anomaly map shows that Shatsky Rise is remarkably covered entirely by linear magnetic anomalies. From the magnetic anomalies alone, there is little indication of a large submarine, volcanic mountain range (Figs. 8-10).

Consistent with previous studies, SW-NE trending Japanese lineations and NW-SE trending Hawaiian lineations mainly characterize our study area (Larson and Chase, 1972; Sager et al., 1988; Nakanishi et al., 1989, 1999). The linear character is most pronounced where track density is highest and less linear where track density is low (Fig. 8). Southwest, west and the center of Tamu Massif, the summits of Ori and Shirshov Massifs and Ojin Rise seamounts are covered by a denser network of ship tracks. In addition, track density over the area of 38-42°N, 150-161°E is also higher. Magnetic lineations over these areas are clearly evident. In contrast, data coverage over other areas is sparse and the gridding algorithm produced rounded anomalies in many places.

The confluences of the Japanese and Hawaiian lineations (i.e., magnetic bights), which show the paleo-locations of the P-F-I triple junction (Larson and Chase, 1972; Nakanishi et al., 1999), occur from the southwest corner of our anomaly map to the northeast corner, following the axis of Shatsky Rise up to the point where the Papanin ridge bends eastward around 42.5°N, 165°E.

Breaks of the linear pattern are also visible in the anomaly map (Figs. 9, 10). Around 34°N, 151°E, some curved positive anomalies are delineated. A broad and complex negative stretches from the west edge of our map to Tamu Massif, making the

area of 32-33°N, 150-158°E mainly characterized by complex linear and curvilinear segments. Both features mentioned above located between the M22 and M19 isochrons identified by Nakanishi et al. (1999), perhaps resulting from the reorganization of the P-F-I triple junction. Another change occurs north of 42°N, where the directions of magnetic lineations are disturbed and some anomalies are aligned nearly N-S. Poor data control leads to large uncertainties in identification of the anomalies in this region.

Surprisingly, topography shows little obvious influence on the shape of magnetic anomalies in Shatsky Rise. A large positive anomaly over Tamu Massif is trends SW-NE, in agreement with the Japanese lineation trend. Ori and Shirshov Massifs and Papanin Ridge have no discernible effect on anomalies as they are traversed by magnetic lineations.

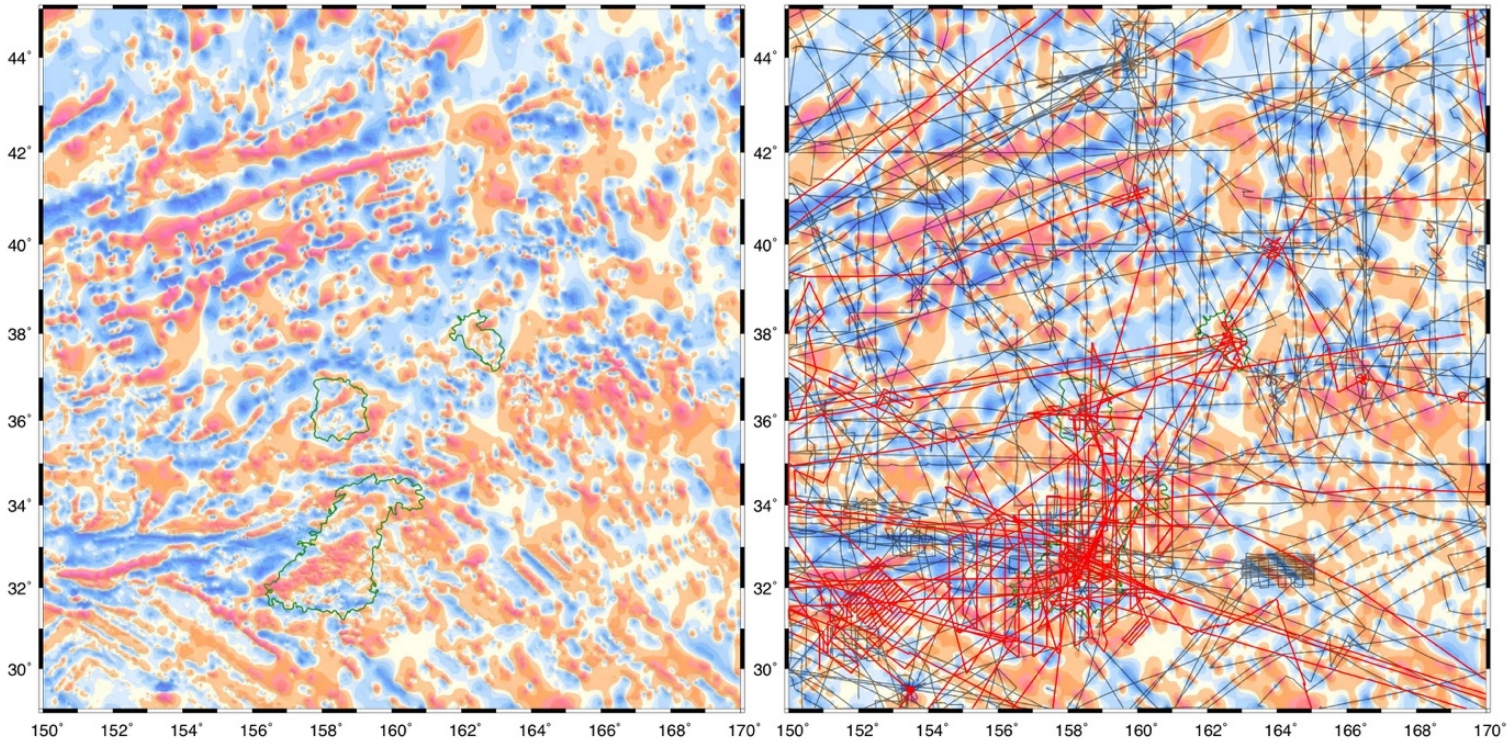

Figure 8. Ship tracks over Shatsky Rise magnetic anomaly map, showing data constraints for magnetic anomalies. (left) Raw magnetic anomaly map. Green bathymetry contours (4 km in depth) show the footprints of Tamu, Ori and Shirshov massifs. (right) Magnetic anomaly map overlapped with ship tracks. Black lines show older cruises positioned with navigation other than GPS, while red lines denote surveys positioned with GPS.

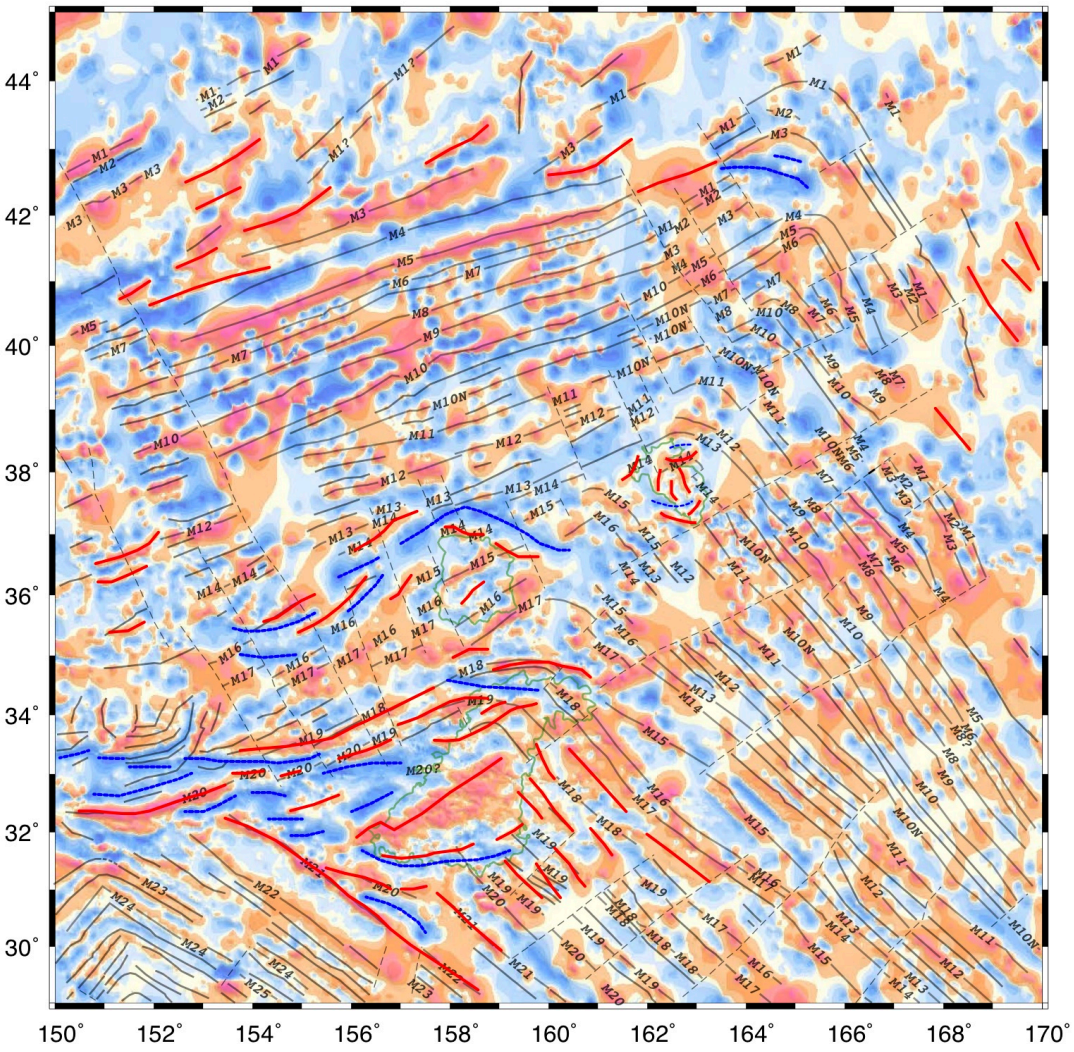

Figure 9. Shatsky Rise magnetic anomaly map with published magnetic isochrons (solid black lines) and fracture zones (dashed black lines) (Nakanishi et al., 1999, 2015). Thicker red (blue) lines show positive (negative) magnetic lineations interpreted from the anomaly map. Green bathymetry contours (4 km in depth) show the footprints of Tamu, Ori and Shirshov massifs.

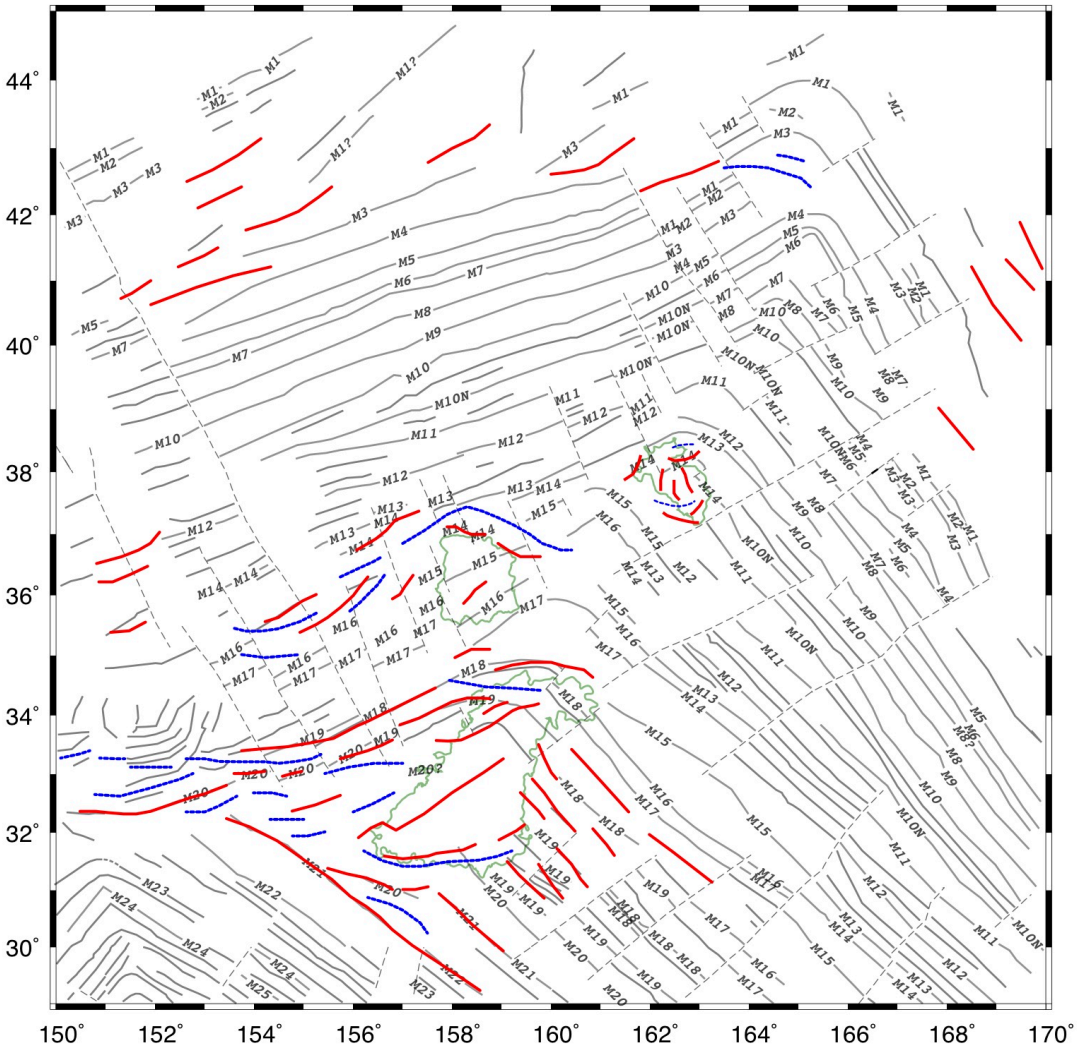

Figure 10. Newly-identified magnetic lineations compared to the Nakanishi et al. (1999) isochron map. Thin solid (dash) gray lines denote isochrons (fracture zones) identified by Nakanishi et al. (1999, 2015). Thicker red (blue) lines show positive (negative) magnetic lineations interpreted from the anomaly map. Green topographic contours (4 km in depth) show the footprints of Tamu, Ori and Shirshov massifs.

2.4.1 Comparison with previous isochron map

Our anomaly map agrees well with the Nakanishi et al. (1999) isochron map, especially those magnetic lineations located in deep oceanic basins. Whereas, with new data, our anomaly deciphered new magnetic lineations (Figs. 9, 10), including new lineations at the center of Tamu Massif, several Hawaiian lineations east of Tamu Massif around 32.5°N, 161°E, a possible repeated M16 isochron across the middle of Ori Massif, lineations across the center of Shirshov Massif, several new lineations younger than M3 both in Japanese and Hawaiian lineations. Furthermore, curvilinear magnetic lineations are also identified in our new anomaly map, compared to the segmented isochrons postulated by Nakanishi et al. (1999). That is to say, some isochrons may be curved in response to tectonic activities, but not segmented as proposed by previous studies. Particularly, curvilinear magnetic lineations west of Tamu and Ori Massifs break the trend of Japanese lineations (Figs. 10, 11). Moreover, the amplitudes of discordant and curvilinear lineations are usually larger.

2.4.2 Description of magnetic anomalies

2.4.2.1 Lineations over deep basins

Magnetic lineations are more linear and regular within surrounding ocean basins. Southwest of Tamu Massif is characterized by magnetic bights whose apexes progress northwest (Fig. 9).

East of Shatsky Rise are mainly NW-SE trending Hawaiian lineations (Fig. 9). East of Tamu and Ori Massifs, Hawaiian lineations are easily identified as they are

regular in this area. In contrast, the linear anomalies are more difficult to follow southeast of Shirshov Massif where Ojin Rise Seamounts occur. Here the anomalies are not well defined and appear as broad positives. On potential cause is the high-amplitude positives produced by the seamounts. Another problem is that many magnetic data over this area are from a single, pre-GPS cruise, showing large crossover errors. Farther north, due to data paucity, magnetic anomalies are often rounded or isolated short features. Several Hawaiian lineations are still identifiable between 38°N and 42°N, but not north of 42°N. Another finding is that the trend of Hawaiian lineations changed from ~N45°W southeast of Tamu to ~N30°E east of Papanin Ridge, which may result from changes of tectonic stress fields that accommodate the emplacement of Shatsky Rise (Sager et al., 1988).

West of Shatsky Rise, the map is characterized by the SW-NE trending Japanese lineations (Fig. 9). North of 42°N, similar to the Hawaiian lineations, the Japanese lineations are not well defined due to the scarcity of data. Between 38°N and 42°N, west of Papanin Ridge and Shirshov Massif, long and coherent Japanese lineations have been delineated by virtue of denser ship tracks. North of the long M3 Chron at 41.7°N, 156.5°E, the new anomaly map portrays several new lineations that are less regular (Fig. 10), indicating complex tectonic environments that disturbed the ridge geometry. In the area of 40.5-43°N, 162-163.5°E where Nakanishi et al. (1999) picked fracture zones and short spreading segments, the gridding combines the data into a large positive anomaly (Fig. 9) because of the scarcity of data in this area.

West of Ori and Tamu Massifs, the SW-NE trends of Japanese lineations are rarely indicated (Fig. 11). Rounded anomalies are portrayed due to data paucity, for example, the area of 34-35°N, 152.5-154°E and 34.5-36°N, 154.5-158°E. Closer to Ori and Tamu Massifs, where data are denser, gridding delineated curvilinear anomalies that break surrounding anomaly pattern. Around 35.0°N, 155°E, several curvilinear negative and positive anomalies are newly identified, extending to the flank of Ori Massif. West of Tamu Massif, the pattern of the anomalies is more complicated. Our map confirmed the curved lineations around 33-34°N, 150-152°E, which was interpreted in previous studies as caused by a microplate (Sager et al., 1988; Nakanishi et al., 1999). South of the microplate, a W-E trending, broad negative obscures part of the curvilinear positives that belong to the microplate and may extend into the western flank of Tamu at 158°E. South of this broad negative, there is a wide and high-amplitude curvilinear positive whose east tip was identified as M20 by Nakanishi et al. (1999).

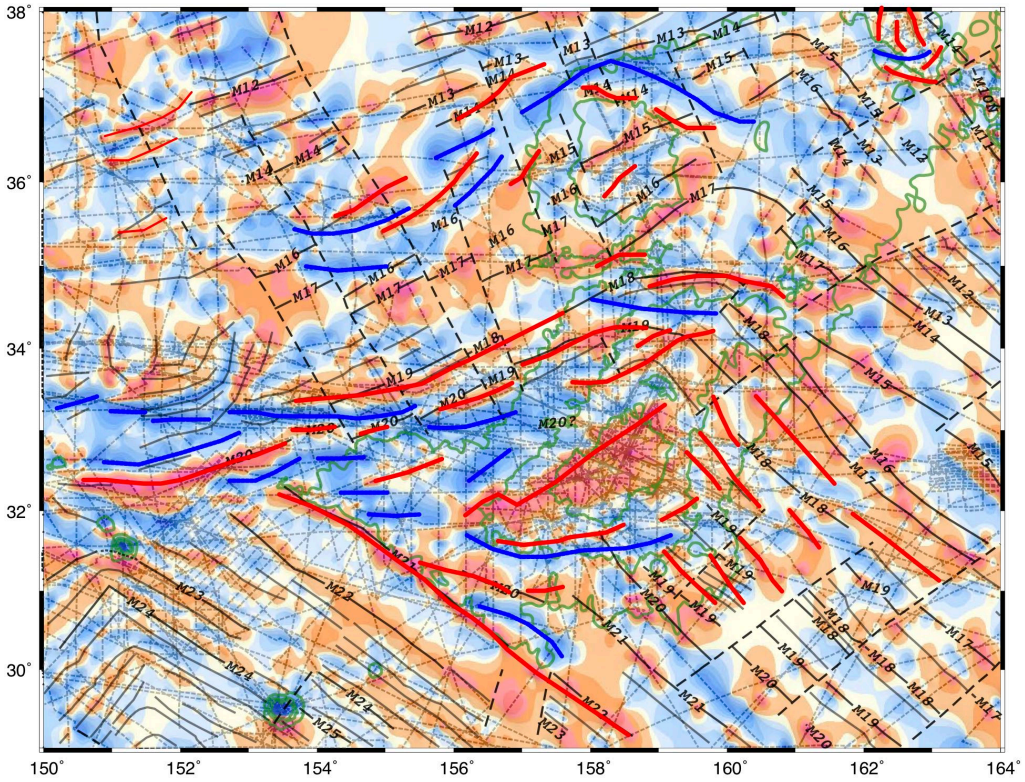

Figure 11. Magnetic anomaly map of Tamu and Ori Massifs. Annotations are the same as Figure 10 except that topographic contours of -5 km, -4 km, -3 km are shown and ship tracks are represented by gray dashed lines.

2.4.2.2 Lineations over high edifices

Recent magnetic data reveal the pattern of magnetic anomalies at the center and the uppermost flanks of the high edifices within Shatsky Rise (Figs. 11, 12). A surprising finding is that these anomalies are mostly linear or curvilinear, unexpectedly cutting through topographic contours. However, unlike the coherent and regular Hawaiian and Japanese lineations in the abyssal plains, lineations are sometimes widened or distorted as they pass through high edifices.

Tamu Massif is mostly traversed by linear and curvilinear magnetic anomalies. Although the pattern is complex, our anomaly map reveals that magnetic anomalies over

Tamu Massif show continuous trend change that may result from reorganization of spreading directions (Fig. 11). The M21 isochron along the southwest boundary of Tamu Massif formed right prior to the formation of Tamu Massif (Nakanishi et al., 1999). Previous studies identified a short positive on the lower south flank of Tamu Massif as M20 with a different trend from M21. With resolution owing to new data, our anomaly map shows that this short anomaly is longer and splits from M21 at 31.2°N, 155.7°E, rotating ~20° anticlockwise. North of this anomaly, there is a long, W-E trending negative anomaly extending from 31.7°N, 157°E to 31.7°N, 160°E. It is coupled with short anomalies with the same trend to the south and north. Further north, the center of Tamu Massif is distinctly characterized by a broad, linear positive anomaly that trends SW-NE, in alignment with the volcano axis and the trend of Japanese lineations. Interestingly, while the southern boundary of this anomaly is ragged, the north side is sharp and highly linear. West of the central positive are mostly SW-NE trending negative anomalies. Whereas, their trends are discordant and some are curvilinear, which may be associated with the influence of the W-E trending broad negative west of Tamu Massif. New and notable is that there is a short, broken positive anomaly over the low western extension of Tamu Massif at 32.5°N, 155.5°E. It has the same trend as the central positive. The northern flank of Tamu Massif is cut through by magnetic bights, the trend of which, however, is different from what traced by Nakanishi et al. (1999). Moreover, a W-E trending wide negative cuts though these magnetic bights at 34.5°N, 159°E.

The center of Ori Massif is also traversed by linear magnetic anomalies and new data decipher curvilinear anomalies wrapping around the massif (Fig. 11). Ori Massif was formed right after a northwest jump of the P-F-I triple junction from the north flank of Tamu Massif to the south edge of Ori Massif (Nakanishi et al., 1999). As a result, its south edge records the west arm of the M17 bight. Going northwest, the center of Ori massif is traversed by magnetic lineations M16-M14. New data define these central lineations as trending N45°E, slightly different from the trend of surrounding Japanese lineations which is N30°E. In addition, between M16 and M15, new data portray another short positive anomaly, the shape and amplitude of which are similar to the M16 south of it. The most distinct feature is the broad, deep negative bight encompassing the northwest boundary of Ori Massif, which was previously missed because isochron studies only picked and connected correlated peaks (Nakanishi et al., 1999). Positive segments south of this negative anomaly appear to form a correlated positive bight, including the M15 isochron at 36.3°N, 157.5°E, one pair of M14 isochrons at 37°N, 158.5°E and a NW-SE trending positive anomaly east of Ori Massif. Unfortunately, due to the lack of data around 36.7°N, 157.7°E, the connection of these positive anomalies into a positive bight is unclear. Similar to Tamu Massif, the west of Ori Massif is also characterized by several curvilinear anomalies that break the trend of SW-NE trending Japanese anomalies but show connections to the broad negative northwest of Ori Massif.

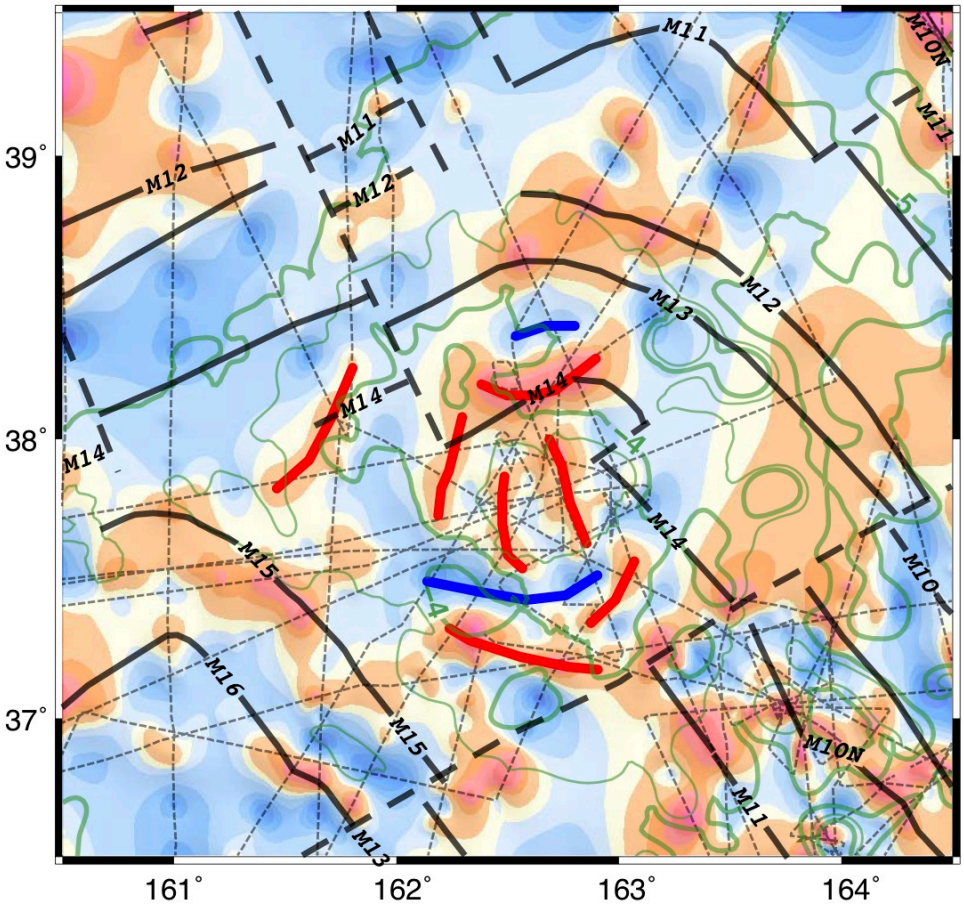

Figure 12. Magnetic anomaly map detail showing Shirshov Massif. Annotations are the same as those in Figure 10 except that topographic contours are plotted at 0.5-km intervals and annotated at 1-km intervals. Ship tracks are plotted as gray dashed lines.

Shirshov Massif is not as well surveyed as Tamu and Ori Massif. The center of this massif is covered by relatively dense ship tracks, whereas the flanks surrounding it show large data gaps, leading to large uncertainties in identification of magnetic lineations (Fig. 8, Fig. 12). Shirshov Massif is also surrounded by curvilinear magnetic lineations, albeit shorter ones. South of the massif is characterized by an E-W striking anomaly at 37.2°N, 162.7°E. A SW-NE trending anomaly splits from it at 37.3°N, 163°E, which seems to follow the trend of Shirshov Massif's southeast boundary.

Surprisingly, the center of Shirshov Massif is crossed by three lineations, almost trending N-S (Fig. 12). North of these three lineations is another E-W trending lineation where Nakanishi et al. (1999) identified M14. Its amplitude is much higher than surrounding anomalies and its eastern tip is curved northward, different from the M14 bight. Farther north, there are one or two magnetic bights, which were identified by Nakanishi et al. (1999) as M12 and M13. These discordant magnetic lineations imply complex tectonics during the formation of Shirshov Massif.

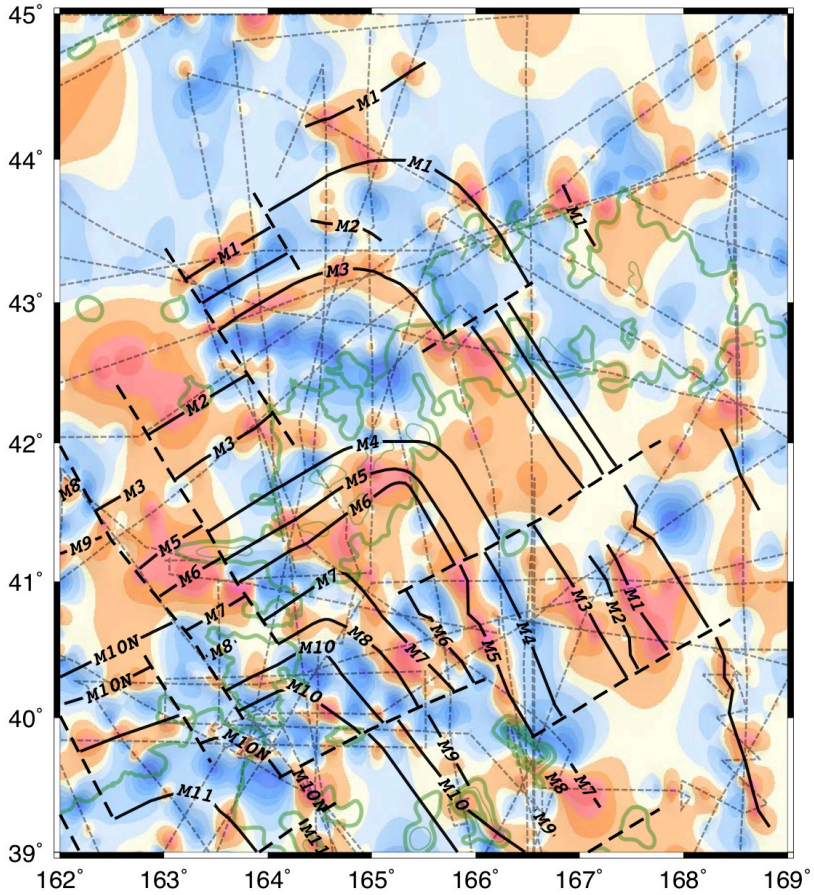

Figure 13. Magnetic anomaly map of Papanin Ridge. Conventions are the same as Figure 12.

Over Papanin Ridge ship tracks become more sparsely distributed and magnetic anomalies are usually defined as isolated segments or rounded anomalies (Fig. 13). Nevertheless, the SW-NE trending Japanese lineations and the NW-SE trending Hawaii lineations are still traceable west and east of Papanin Ridge. Their confluences (i.e., magnetic bights) are poorly defined. The most-clearly-defined anomaly is the M3 bight that is located west of Papanin Ridge. South of it, the anomaly map shows a broad negative anomaly that interrupts the trends of other anomalies.

2.5 Discussion

2.5.1 Construction of magnetic anomaly map

2.5.1.1 Influences of sparse data

Although linear or curvilinear magnetic anomalies predominantly characterized the magnetic anomaly map for Shatsky Rise, linear patterns are sometimes disrupted by rounded anomalies. Few of these rounded anomalies are generated by the influences of seamounts. Instead most result from the gridding algorithm treatment of sparse data. This algorithm uses splines under tension, which tends to construct equidimensional anomalies. Such anomaly structure likely does not reflect that of the crustal magnetic field. This problem is especially troublesome for the areas northwest of Tamu Massif, west of Ori Massif, and around Shirshov Massif and Papanin Ridge. Although there have been many cruises that collected magnetic data around Shatsky Rise over the years, the collected data are nevertheless inadequate in some areas to portray the crustal field

pattern. Dense, regular magnetic surveys are needed to reach the next level of magnetic anomaly interpretation.

2.5.1.2 Data processing methods

Construction of global magnetic anomaly data sets sometimes involve adjustment of long-wavelength signals using a magnetic field model derived from satellite measurements (Maus et al., 2009; Quesnel et al., 2009). This is a major difference between this compilation and prior global studies. Because our study is limited in size and do not show clear long wavelength shifts, such corrections were not deemed to be necessary.

Leveling methods have been adopted to promote data agreement (e.g., Quesnel et al., 2009; Ishihara et al., 2011). Such methods, however, force data measurements to agree where they are offset. Because this agreement is artificial and can obscure anomaly features, leveling was not done in this study. It makes a prettier map, but at the expense of data fidelity. Instead, we used another approach, developing the "backbone" method, using well-navigated data as a benchmark to which poorly navigated data were fit, thus reducing the inconsistencies between different surveys.

Largest COE are mostly related to old cruises that used celestial navigation. Although it is impossible to uniquely reconstruct the actual positions for old cruise tracks, the decrease of RMS_{COE} is apparent after the correction of navigation errors, indicating that the inconsistencies within our data set mainly arise from the poor navigation techniques used during older epochs. In this study, correction of navigation

errors involved interactive replotting of anomaly maps and recalculation of COE, a process that was extremely time-consuming. A more efficient algorithm is needed. One could construct a grid search algorithm that would test different x,y offsets and compare the COE to find the minimum values.

2.5.1.3 Comparison with EMAG2v3

Compared to the Shatsky Rise anomaly map extracted from the global Earth Magnetic Anomaly Grid Version 3 (EMAG2v3; Meyer et al., 2017), the resolution of our anomaly map is higher and thus shows more detail, partly because the grid interval for our anomaly map is 1 arc-minute while EMAG2v3 is gridded at 2 arc-minutes resolution (Fig. 14). Herein EMAG2v3 refers to the version representing magnetic anomalies at sea level (another representation of EMAG2v3 gives anomalies upward continued to a constant altitude of 4 km). Unfortunately, input data to EMAG2v3 are not described, meaning that it is difficult to interpret or explain anomalies on this product.

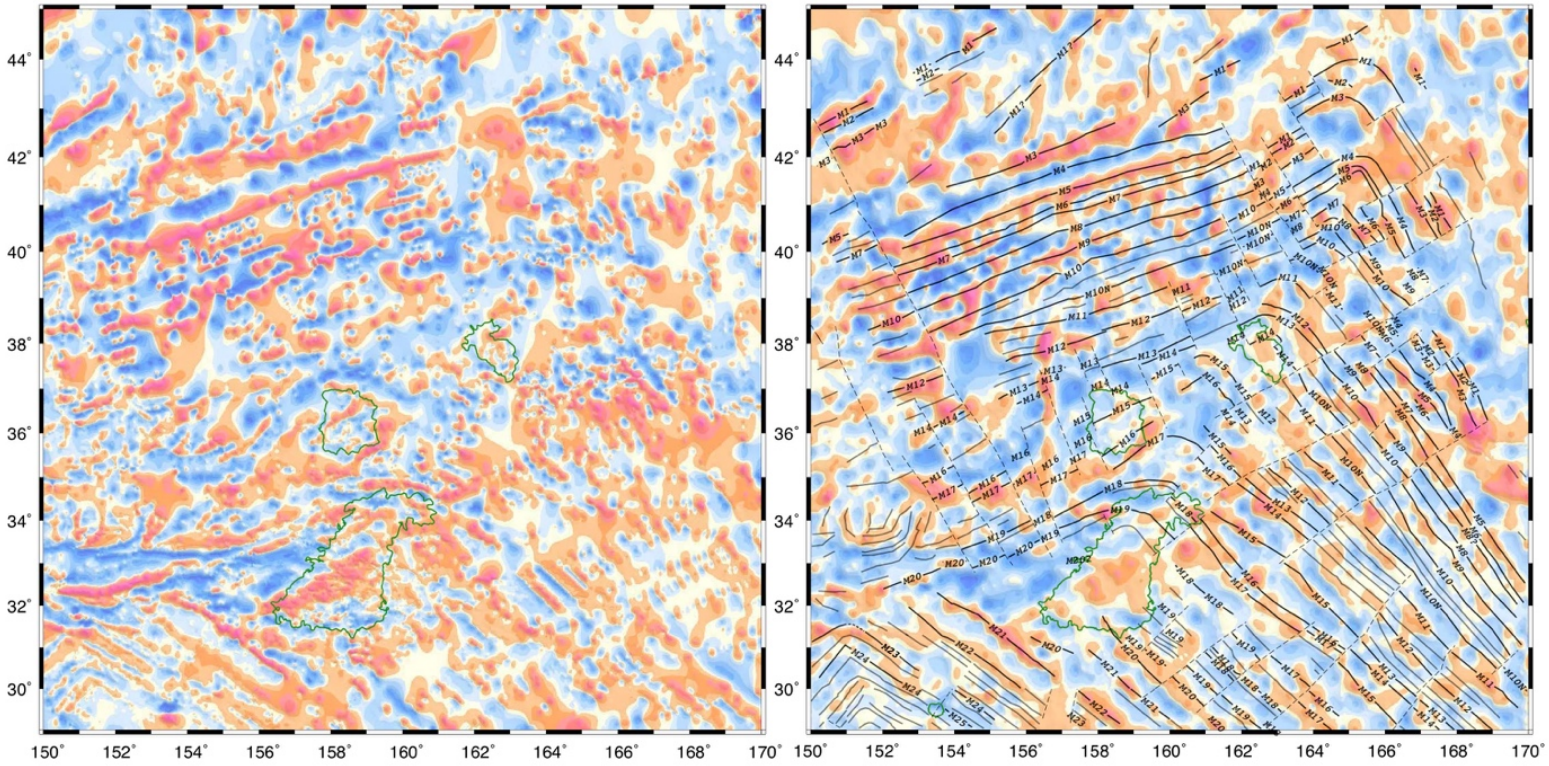

Figure 14. The EMAG2v3 map for Shatsky Rise. (left) our new magnetic anomaly map for Shatsky Rise. (right) Shatsky Rise magnetic anomaly map based on EMAG2v3. Annotations are the same as Figure 9.

The overall patterns of the two anomaly maps are similar as they both show that SW-NE trending Japanese lineations and NW-SE trending Hawaii lineations converge at Shatsky Rise (Fig. 14). Furthermore, both show that the P-F-I triple junction migrated along the axis of Shatsky Rise northeastward. Whereas, in the EMAG2v3 map, only broadest magnetic lineations are well defined, the others are broken into rounded, irregular anomalies. In contrast, narrower magnetic lineations are better deciphered in our anomaly map. Additionally, at the centers of the high edifices, details are not apparent in the EMAG2v3 map. Indeed, newly-identified linear or curvilinear magnetic anomalies around and at the center of high edifices are missing. For instance, the three N-S trending linear anomalies across the center of Shirshov Massif are blended as rounded anomaly.

2.5.2 Interpretations of the magnetic anomaly map

The fact that magnetic lineations are pervasive across Shatsky Rise is striking. Especially, recent magnetic data reveal that the high elevations within Shatsky Rise are also traversed by magnetic lineations. Indeed, without plotting the bathymetry contours of the Shatsky Rise massifs, one would not be able to pinpoint their locations. They have little influence on magnetic anomaly character. However, the new anomaly map did show breaks of the linear magnetic anomalies and curvilinear anomalies around high edifices, indicating the involvement of complex tectonics. But, with new data, central magnetic anomalies appear to show connections to surrounding coherent Japanese and Hawaiian lineations, making the reorganizations of spreading ridges traceable.

Tamu Massif magnetic anomalies show a reorientation of a segment of Pacific-Farallon ridge, which rotated to end up in alignment with Pacific-Izanagi ridge, as the triple junction propagated across Tamu Massif. This event initiated with the split of the NW-SE trending M21 along the southwest boundary of Tamu Massif, involved the intervening phase that characterized by the W-E trending negative anomalies south of the central positive, and finally ceased when the SW-NE trending central positive formed (Fig. 11). That is to say, the NW-SE trending Pacific-Farallon ridge rotated ~90º counterclockwise and turned to SW-NE spreading. According to magnetic isochrons identified by Nakanishi et al. (1999), M20 and M19 characterize the west flank of Tamu Massif and M18 forms a bight across the northeast flank of Tamu Massif. The central positive must form before M20 or M19. In this sense, the long W-E trending negative anomaly south of the central positive appears to be a normal polarity Chron either between M21-M20 or M20-M19 (Note: positive anomalies at this location are caused by reversed polarity and vice versa). To achieve the broad width of the central positive, rapid emplacement as well as a long period of reversal polarity are needed. The central positive may be formed during M20. However, the pattern of magnetic anomalies west of the central positive suggest that the formation of Tamu Massif is more complicated. The broken positive anomaly at 32.5ºN, 155.5ºE shares the same trend as the central positive and thus may indicate a segmented piece related to the central positive (Fig. 11). The negative anomalies around the broken positive are not strictly linear but are linear or curvilinear showing variable trends and high amplitudes. This disorderliness may result from complex ridge tectonics associated with the ~90º rotation of the Pacific-Farallon

ridge. Indeed, propagating rift lithosphere is commonly characterized by high-amplitude magnetic anomalies (e.g., Hey, 2005) and propagating rifts are often found at microplate boundaries (e.g., Bird et al., 1998).

Ori Massif formed at the Pacific-Izanagi ridge as its center is traversed by regular magnetic lineations (M16-M15) trending SW-NE, parallel to Japanese lineations. It is striking that these anomalies are both clear and linear, despite being in the center of the large, nearly-circular volcanic edifice of Ori Massif. This means that Ori Massif formed at a spreading center and the ridge tectonic regime was little disturbed by the massive volcanism. However, the newly-identified negative bight to the north and the M17 bight to the south suggest that Ori massif was formed as a microplate surrounded by multiple triple junctions. The triple junction to the north may be a short lived one because we cannot find other similar bights north and south of it. Furthermore, when Ori Massif formed, the P-F-I triple junction was east of it, migrating northeast toward Shirshov Massif, so the relation of Ori Massif to the P-F-I triple junction is unclear. In addition, between the central M16 and M15 isochrons identified by Nakanishi et al. (1999) we identified another short M16, which may result from a small ridge jump. Together, Ori Massif appears to have been formed by seafloor spreading, which may have been complicated by microplate tectonics and ridge jumps.

Shirshov Massif, like Tamu and Ori massifs, is also characterized by magnetic lineations. The pattern of magnetic lineations over Shirshov Massif is discordant with magnetic bights identified by Nakanishi et al. (1999) (Fig. 12). Both the south and north edges of Shirshov Massif are characterized by W-E trending negative anomalies,

indicating ridge reorganizations. The N-S trending magnetic lineations across the center are the most striking finding at Shirshov Massif. Accompanied with curvilinear magnetic anomalies surrounding the massif, we propose that Shirshov Massif may be another microplate. However, as the flanks of Shirshov Massif are covered by sparse data, the connections to surrounding magnetic lineations are uncertain.

Papanin Ridge appears to be traversed by magnetic bights recording the paleo-locations of P-F-I triple junction (Fig. 13). Rounded anomalies around Papanin Ridge do not allow interpretation of the triple junction location in many places. Nevertheless, the position of the M3 bight to the west of the ridge implies that the triple junction separated from Papanin ridge before M3. The high-amplitude, broad negative anomaly south of M3 appear to obscure the paths of the P-F-I triple junction, indicating complex tectonics with response to the separation of Papanin ridge and the triple junction.

North of 42ºN, the split of M3 at 42.5ºN, 160.5ºE suggest that Japanese lineations rotated counterclockwise (Fig. 10). This reorganization of Pacific-Izanagi ridge appears to accommodate the northwest migration of the P-F-I triple junction, which, as aforementioned, separated from the eastward extension of Papanin Ridge before M3. Data in this region are so sparse that it is difficult to interpret this reorganization with confidence.

2.5.3 Implications for the formation of Shatsky Rise

Shatsky Rise appears to be a submarine mountain range whose formation involves frequent ridge reorientations and ridge jumps. These disruptions of ridge

geometry may be attributed to the influences of hotspot-related stresses. Alternations of ridge geometry associated with ridge-hotspot interaction have been observed near many hotspots such as Iceland (Hardarson et al., 1997; Ito, 2001), the Galapagos Spreading Center (Wilson and Hey, 1995), the Azores Plateau (Gente et al., 2003; Georgen, 2011), and Ascension (Brozena and White, 1990). Moreover, magnetic lineations imply that the P-F-I triple junction jumped at least 9 times northeastward whereas plate kinematics indicate that the triple junction should have migrated northwestward (Sager et al., 1988; Nakanishi et al., 1999). This discrepancy may also be attributed to the influence of a hotspot. Indeed, numerical models have suggested that mid-ocean ridge jumps could be triggered by magmatic heating and thinning of lithosphere in response to migrating hotspot (Mittelstaedt et al., 2008; 2011).

Newly identified magnetic lineations traversing high edifices suggest that, although ridge-controlled tectonics may have been complicated by a hotspot, they were not overwhelmed by the massive volcanic eruptions. This challenges our common wisdom about the formation of such massive volcanic edifices. The bulk of a large volcano is usually a vertical stack of lava flows, most of which record the magnetic field direction (Harrison et al., 1975). If occurring during a period with no magnetic reversals, the sum of such lava layers would result in a coherent dipolar anomaly. If formation includes periods of magnetic reversals, the result should be radial or irregularly-shaped magnetic anomalies (Harrison et al., 1975; Sager et al., 1993; 2005). However, linear magnetic anomalies recorded in Shatsky Rise are analogous to those formed at mid-

ocean ridges (MOR) where magma eruptions are laterally constrained to the ridge crest (e.g., Gee and Kent, 2007).

The MOR formation mechanism seems to reconcile with some odd geophysical and geochemical observations in the Shatsky Rise oceanic plateau. Nakanishi et al. (1999) noted the large distance between M21 and M19 and suggested that a ridge jump annexed a piece of another plate to the Pacific plate. Our new anomaly map, however, suggests that Tamu Massif formed as a MOR and the extra spacing occurred because of complex ridge reorientations. Furthermore, the $^{40}Ar/^{39}Ar$ dating of core samples is in keeping with the age of Chrons M21-M19 that cut through Tamu Massif (Mahoney et al., 2005; Heaton and Koppers, 2014; Geldmacher et al., 2014; Tejada et al., 2016). The implication is that Tamu Massif is the crust itself instead of a volcano sitting on a pre-existing crust. Another evidence supporting the MOR formation is that the geochemical and isotopic signatures of core rocks from Shatsky Rise are mostly similar to mid-ocean ridge basalts (MORB) (Mahoney at al., 2005; Sano et al., 2012).

Although recent seismic studies suggest Tamu and Ori massifs to be large central volcanoes, several lines of the morphology are not well explained but might support a MOR origin. Intra-basement reflectors at Tamu and Ori Massifs appear to be subparallel to the surface of the basement top (Sager et al. 2013; Zhang et al., 2015), i.e., there are no dip-to-center reflectors caused by isostatic depression in response to centralized eruptions, as occurs for example with seaward-dipping reflector packages (Planke et al., 2000). Instead, the massifs are in isostatic balance during their emplacement. Furthermore, the slopes of Tamu and Ori massifs are abnormally gentle. One

explanation is the formation near an active ridge crest where thin and weak lithosphere fails to support a steep bulk.

2.6 Conclusions

A large and heterogeneous magnetic data set has been compiled to construct a magnetic anomaly map for Shatsky Rise. Systematic data corrections have been applied to not only remove spurious signals but also improve the consistencies within the data set. Finally, the $Mean_{COE}$ and RMS_{COE} of the data set were improved from (51.1nT, 1896.8nT) to (0.1nT, 55.5nT).

According to the new magnetic anomaly map, magnetic lineations in the abyssal plains are in good agreement with previous isochron maps. However, new linear or curvilinear magnetic anomalies were identified over high edifices within Shatsky Rise, providing new insights into the formation of this huge volcanic mountain range. Tamu Massif results from a ~90º counterclockwise rotation of Pacific-Farallon ridge. Ori Massif formed at the Pacific-Izanagi ridge and may have been a microplate as surrounded by multiple triple junctions. Shirshov Massif may be another rotated microplate because its central anomalies rotated and ultimately trended N-S. High-amplitude and/or curvilinear magnetic anomalies are identified as breaking Japanese lineations west of Tamu and Ori Massif, apparently caused by the complex tectonics of the plate reorganization during the formation of Tamu Massif.

Frequent ridge reorientations and jumps around Shatsky Rise may result from the influences of a hotspot that provided massive eruptions for the construction of this large

oceanic plateau. The complex tectonic changes, however, are traceable with the help of our new anomaly map, especially for Tamu and Ori massifs. Furthermore, all three high massifs are traversed by linear magnetic anomalies, a finding that does not support the hypothesis that they formed as massive central volcanoes. Instead, they formed as mid-ocean ridges. The thickened crust may result from enhanced volcanism by the hotspot. Whereas, the voluminous lava flows are still confined to the neo-volcanic zone, analogous to what usually occurs at spreading centers.

CHAPTER III

MAGNETIC ANOMALY MAP OF ORI MASSIF AND ITS IMPLICATIONS FOR OCEANIC PLATEAU FORMATION[*]

3.1 Overview

Many oceanic plateaus have been emplaced at or adjacent to mid-ocean ridges. To explain plateau volume and thickened crust compared to normal oceanic crust, hotspot-ridge interaction is commonly assumed, but the manner of interaction remains unclear. The Shatsky Rise oceanic plateau is a large volcanic mountain range that formed at a triple junction during Late Jurassic and Early Cretaceous time. Recent drilling and seismic investigations suggest that the intermediate edifice in the rise, Ori Massif, is a central volcano. Paradoxically, magnetic lineations have been traced across the center of Ori Massif, implying formation at a spreading ridge. In this study, we re-examined magnetic anomalies over and around Ori Massif, including new data obtained in the last two decades to obtain insights about formation of this volcanic edifice. Magnetic data from 21 cruises was corrected, combined, and gridded to construct a

[*] Reprinted with permission from "Magnetic anomaly map of Ori Massif and its implications for oceanic plateau formation" by Huang Y., W. W. Sager, M. Tominaga, J. A. Greene, J. Zhang, and M. Nakanishi (2018), *Earth and Planetary Science Letters*, Vol. 501, 46-55, Copyright [2018] by Elsevier.

magnetic anomaly map. Forward and inverse magnetic modeling was done to investigate the magnetic structure of Ori Massif. The results imply that Ori Massif is predominantly characterized by linear magnetic anomalies resulting from alternating normal and reversed polarity magnetization blocks, analogous to similar anomalies recorded by spreading-ridges. This magnetic structure is not expected for a central volcano producing long runout lava flows, suggesting that Ori Massif eruptions must be constrained near the ridge axis. Magnetic bights bracketing the north and south boundaries of Ori Massif imply that it was bracketed by triple junctions, indicating complex ridge tectonics during the formation of Shatsky Rise. The surprising finding that Ori Massif is traversed by coherent magnetic lineations, suggests that other plateaus can record magnetic lineations, despite the large crustal thickness. It also conclusively links Shatsky Rise volcano formation to spreading ridges.

3.2 Introduction

Shatsky Rise is a basaltic large igneous province located in the northwest Pacific Ocean. Magnetic lineations within and around Shatsky Rise indicate that it formed at the Pacific-Farallon-Izanagi (P-F-I) triple junction during Late Jurassic and Early Cretaceous time (Hilde et al., 1976; Sager et al., 1988; Nakanishi et al., 1999). Recent research indicates that the rise primarily consists of three massive volcanoes (Sager et al., 2013, 2016). This raises an important question: how could such large volcanoes form at mid-ocean ridges, which are themselves enormous volcanoes?

Mid-ocean ridges are formed by linear volcanism confined to the plate boundary (Macdonald, 1982), whereas large volcanoes, formed by magmatic eruptions from a central vent or vents, construct edifices with a radial pattern (Mitchell, 2001). How do these processes interact at Shatsky Rise? Many oceanic plateaus appear to be formed at mid-ocean ridges, such as Iceland and the Azores Plateau in the Atlantic (Gente et al., 2003; Foulger et al., 2005), the Magellan Plateau, Hess Rise, and Ontong Java Nui (Manihiki Plateau, Hikurangi Plateau, and Ontong Java Plateau) in the Pacific (Sager, 2005; Taylor, 2006). Thus, Shatsky Rise may be representative of many oceanic plateaus, so the study of this geologic setting can provide important clues for understanding oceanic plateau formation and mantle melting.

Magnetic anomalies over oceanic plateaus have the potential to provide constraints on their formation. Mid-ocean ridges record linear polarity zones in the upper crust as it cools near the ridge crest and is magnetized in the direction of the ambient magnetic field. This process leaves behind a tell-tale pattern of linear magnetic anomalies that has been used to determine the age of the seafloor and the past positions of mid-ocean ridges (e.g., Vine and Matthews, 1963; Heirtzler et al., 1968). The observation of such magnetic lineations implies that volcanism is localized to a narrow linear eruption zone. Additionally, magnetic modeling has been applied to seamounts to obtain paleomagnetic data and constraints on eruption history (Harrison et al., 1975; Sager et al., 1993). Typically, this technique assumes that the seamount is homogenously magnetized or has limited changes in magnetization structure (Harrison et al., 1975). Sager and Han (1993) applied this technique to Tamu Massif (the largest volcanic

edifice of Shatsky Rise) and concluded that much of this edifice was formed within a single polarity period. Nevertheless, Shatsky Rise also contains many linear magnetic anomalies, interpreted as magnetic isochrons recorded by mid-ocean ridges (Nakanishi et al., 1999).

This dichotomy in magnetic anomaly style suggests further study of Shatsky Rise is needed. Here we examine the magnetic anomaly structure of Ori Massif, the second largest edifice within Shatsky Rise. We combine new and old magnetic data over Ori Massif to create a magnetic anomaly map. Magnetic inversion modeling was used to obtain an unbiased estimate of the Ori Massif magnetization structure, which helps interpreting the magnetic anomaly map and sheds new light on the formation of this plateau.

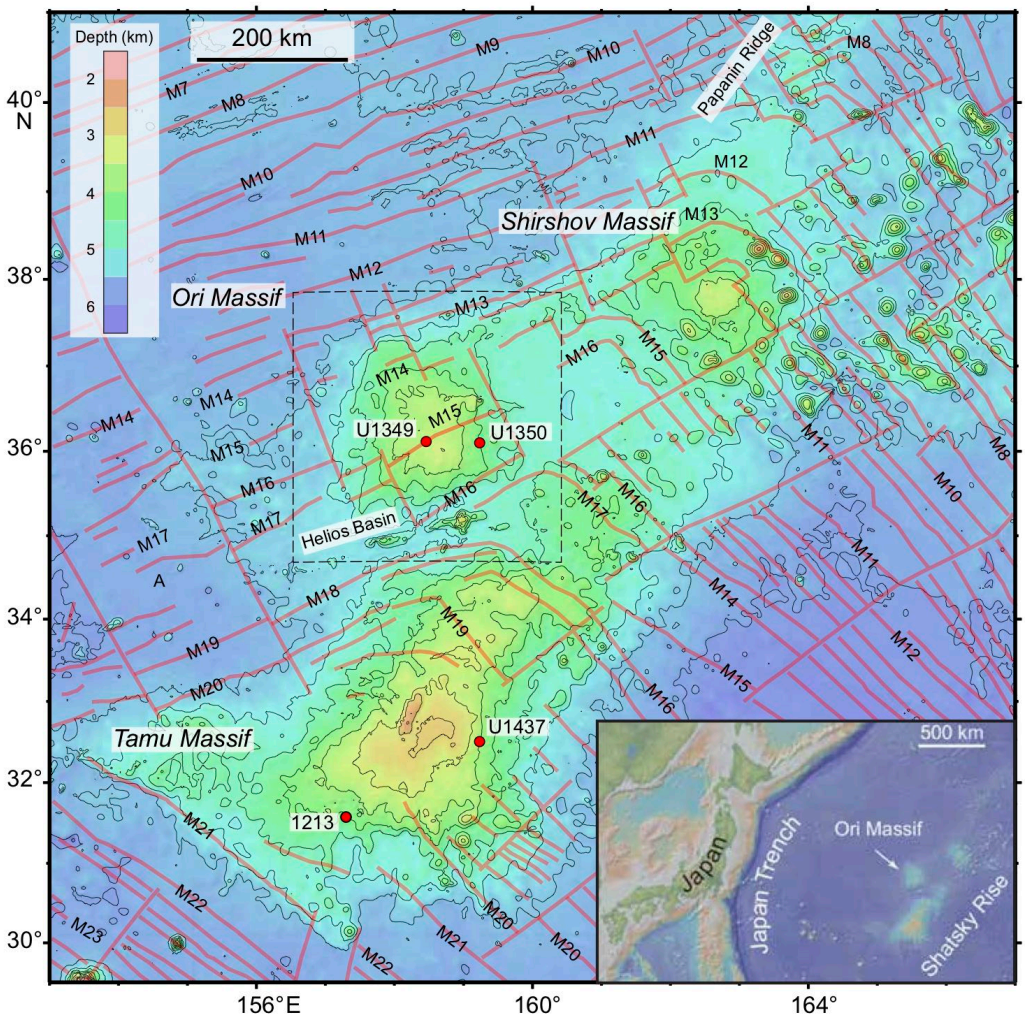

Figure 15. Location map for Shatsky Rise and Ori Massif. Dashed line encompasses the area of Figures 16 to 20. Bathymetric data are estimated depths from satellite altimetry (Smith and Sandwell, 1997). Red lines denote magnetic isochrons and fracture z zones (Nakanishi et al., 1999). Red dots are ODP and IODP drill sites mentioned in the text. Inset shows location of Shatsky Rise relative to Japan and the Japan Trench.

3.2.1 Shatsky Rise geologic setting

The Shatsky Rise is a large basaltic mountain range located ~1500 km east of Japan, formed during the Late Jurassic and Early Cretaceous (e.g., Nakanishi et al., 1999; Sager et al., 1988; 1999). Magnetic lineations suggest that Shatsky Rise is located at the intersections of the SW-NE trending Japanese lineations and the NW-SE trending Hawaiian lineations. The intersections of these magnetic lineations (i.e., magnetic bights) indicate the past locations of the P-F-I (Pacific-Farallon-Izanagi) triple junction from Late Jurassic through Mid-Cretaceous time (Larson and Chase, 1972; Sager et al., 1988; Nakanishi et al., 1989, 1999). The axis of Shatsky Rise appears to follow the northeast migration of the triple junction which has jumped at least nine times during the rise emplacement (Nakanishi et al., 1999). Curved and discordant lineation patterns also imply that several microplates may have been annexed to the Pacific plate during during its formation (Sager et al., 1988; Nakanishi et al., 1999).

With an area of ~5.3 x 10^5 km^2 (Zhang et al., 2016), Shatsky Rise consists of three large edifices (Tamu, Ori and Shirshov massifs) and a volcanic ridge (Papanin Ridge) (Fig. 15). The volume of the edifices progressively decreases from Tamu Massif to Shirshov Massif (Sager et al., 1999). Tamu Massif is the largest known single volcano on Earth, comparable in size to the largest volcano in the solar system, Olympus Mons on Mars (Sager et al., 2013). Ori Massif, with an area of ~3.3 x 10^4 km^2, is comparable in area to the Island of Hawaii (~3.0 x 10^4 km^2). Recent studies of coring data from Integrated Ocean Drilling Program (IODP) Expedition 324 suggested waning of volcanism with time as massive flows are thickest on the largest and oldest edifice,

Tamu Massif, but are thinner and fewer on Ori Massif and Shirshov Massif. In contrast, Ori and Shirshov massifs are mainly characterized by pillow flows which indicate modest effusion rate (Sager et al., 2011).

Age constraints for Shatsky Rise are few as most dredged and many core samples are highly altered and not ideal for radiometric dating. Basalt flows cored from Tamu Massif at Ocean Drilling Program (ODP) Site 1213 yielded an Ar^{40}/Ar^{39} radiometric age of 144.6 ± 0.8 Ma (Mahoney et al., 2005). Radiometric dating from IODP Site U1347, also on Tamu Massif, reveal an age of 143-145 Ma (Geldmacher et al., 2014; Tejada et al., 2016). These dates are in good agreement with the ages of the magnetic isochrons that bracket Tamu Massif (M21-M19), indicating that Tamu Massif formed near the triple junction spreading ridges. Late-stage or rejuvenated volcanism is also suggested as the uppermost flows of Site U1347 produced a younger age of ~139 Ma and the Toronto ridge, at the summit of Tamu Massif, gave an age of ~129 Ma (Geldmacher et al., 2014; Tejada et al., 2016). As for Ori Massif, igneous rocks from IODP Site U1350, located on the southeast flank of the massif, yielded a radiometric date ~134 Ma (Heaton and Kroppers, 2014). This age is ~4-6 Myr younger than magnetic lineations M16 and M15 which cross Ori Massif (Nakanishi et al., 1999; Ogg, 2012). Two possible factors for this discrepancy are that Site U1350 lavas recorded late-stage volcanism or that the M-anomaly time scale is inaccurately calibrated (Ogg, 2012).

Recent multichannel seismic data give insights into the structure of the edifices within the Shatsky Rise. Both Tamu and Ori Massif are seen to be large central volcanoes because sub-parallel lava packages are imaged dipping outward from the

summits (Sager et al., 2013; Zhang et al., 2015). The crust beneath Ori Massif is estimated to be ~25 km thick using reflection imaging of the Moho and isostatic modeling (Zhang et al., 2016).

3.2.2 Study rationale and motivation

Nakanishi et al. (1999) mapped magnetic lineations across the center of Ori Massif, suggesting its formation at a spreading ridge. This is an unexpected result considering the thickness of Ori Massif crust and the fact that seismic data indicate it to be a massive shield volcano. New magnetic data have been collected over Ori Massif in the past two decades, suggesting that a re-examination of the magnetic anomalies is warranted. The study by Nakanishi et al. (1999) focused on tracing magnetic isochrons by picking and correlating magnetic anomaly peaks, a subjective process. In this study, we take a more objective approach by gridding and plotting a magnetic anomaly map and using this product as input to magnetic modeling routines. The objective is to understand the magnetization structure of Ori Massif and thereby better obtain clues about its formation.

Table 3. Magnetic data sources of Ori Massif.

Cruise ID	Year	*Ship*	Source institution	Navigation[1]
77031705	1970	*Kana Keoki*	Hawaii Institute of Geophysics	DopSat
FK151005*	2015	*Falkor*	Schmidt Ocean Institute	GPS
KH-74-4	1974	*Hakuho-Maru*	Ocean Research Institute, The University of Tokyo	DopSat
KH-82-5	1982	*Hakuho-Maru*	Ocean Research Institute, The University of Tokyo	DopSat
KH-88-3	1988	*Hakuho-Maru*	Ocean Research Institute, The University of Tokyo	DopSat
KH-96-3	1996	*Hakuho-Maru*	Ocean Research Institute, The University of Tokyo	GPS
ANTP03MV	1970	*Melville*	Scripps Institution of Oceanography	DopSat
DSDP32GC	1973	*Glomar Challenger*	Scripps Institution of Oceanography	DopSat
IODP324JR*	2009	*JOIDES Resolution*	IODP/Texas A&M University	GPS
INDP01WT	1976	*Thomas Washington*	Scripps Institution of Oceanography	DopSat
MG28	1985	*Morskoy Geofizik*	Institute of Marine Geology/Geophysics	DopSat
MGL1206*	2012	*Marcus G. Langseth*	Lamont-Doherty Earth Observatory	GPS
ODP198JR*	2001	*JOIDES Resolution*	IODP/Texas A&M University	GPS
POL7004	1970	*Oceanographer*	National Oceanic and Atmospheric Administration	DopSat
RC1108	1967	*Robert D. Conrad*	Lamont-Doherty Geological Observatory	DopSat
SI932005	1971	*Silas Bent*	US Navy Naval Oceanographic Office	DopSat
SI932009	1972	*Silas Bent*	US Navy Naval Oceanographic Office	DopSat
SI933010	1972	*Silas Bent*	US Navy Naval Oceanographic Office	DopSat
TN037	1994	*Thomas G. Thompson*	Texas A&M University	GPS
V2006	1964	*Vema*	Lamont-Doherty Geological Observatory	Celest
ZTES05AR	1966	*Argo*	Scripps Institution of Oceanography	Celest

* New data since Nakanishi et al. (1999).
[1] Navigation types: Celest = Celestrial; DopSat = Doppler satellite fixes with dead reckoning; GPS, Global Positioning System

3.3 Data and Methods

3.3.1 Magnetic dataset

Our dataset builds on that of Nakanishi et al. (1999) with the addition of four recent cruises, making a total of 21 cruises with ~9805 km of magnetic data (Table 3). The new dataset is heterogeneous as it spans a time period of 51 years (1964-2015), during which navigation systems have greatly improved. Additionally, the ship tracks

are unevenly distributed (Fig. 16) with most of the data concentrated over the summit of Ori Massif but sparsely spaced in the flank regions.

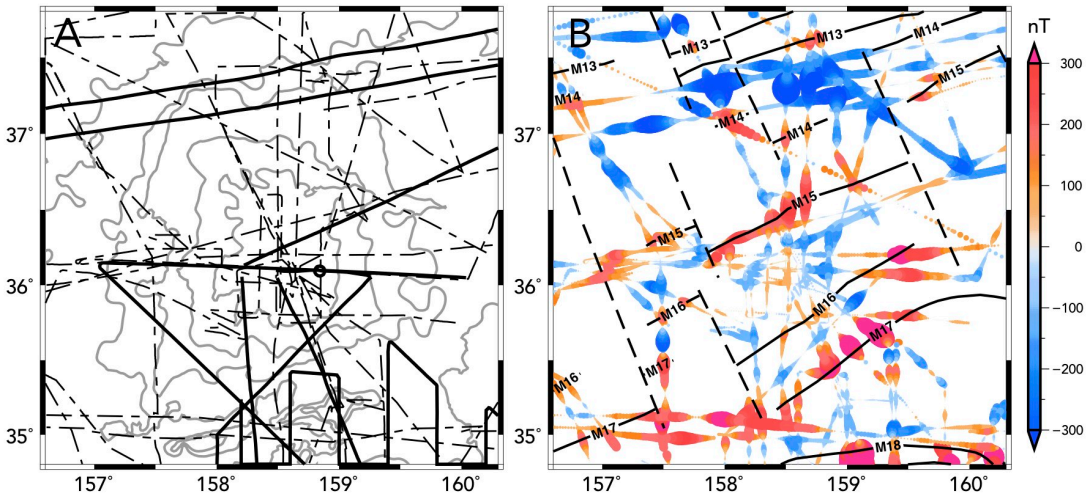

Figure 16. (A) Chart of surveys used in this study. Dashed lines denote cruises used in Nakanishi et al. (1999); solid lines are newer data (Table 3). Gray contours show bathymetry at 500-m intervals. (B) Data coverage and anomalies. Data point size is based on anomaly amplitude (larger point = larger anomaly absolute value) and color denotes both amplitude and sign. Annotated solid lines denote isochrons and heavy dashed lines represent fracture zones (Nakanishi et al., 1999).

Magnetic data were processed with the following steps. 1) Data were adjusted to the International Geomagnetic Reference Field 11 (IGRF11) (Finlay et al., 2010) in order to remove the internal magnetic field and its time variations and produce magnetic field anomalies. 2) Outliers and spurious readings caused by instrumental errors and transcription errors in old cruises were identified and deleted by visual inspection. 3) Simple, external field signals were estimated and removed by the application of Comprehensive Model Phase 4 (CM4) (Sabaka et al., 2004). The CM4 model has a time range of 1960 to mid-2002; however, by updating the DST and F10.7 indices used by the

model, the estimation of the external field was extended to the end of 2015 so that the updated CM4 model is applicable for the whole dataset. 4) The Kp index was examined to find periods disturbed by geomagnetic storms (Kp > 5.0) and those data were inspected and deleted if noisy. 5) Cross-over errors (COE), i.e., differences where ship tracks cross, were used to check the external consistency between data from different cruises. During the COE check, we noted that unexpectedly high (>80nT) COE mainly arise from navigation errors in surveys carried out before 1968. With visual inspection, we moved these tracklines small distances (less than ~3 km) around their original positions to minimize their COE. In addition, using the "x2sys" package in the GMT suite (Wessel, 2010) to determine offset, we added or subtracted a constant value to make some older cruises match recent high-quality survey data.

Two steps were used to grid the data. First, data were resampled by taking the median value of 1-arc minute blocks (GMT routine "blockmedian"). Thereafter, the dataset was gridded by virtue of continuous curvature splines (GMT routine "surface") with a tension factor of 0.25, which is good for potential field data (Smith and Wessel, 1990). The gridded dataset was plotted for interpretation and used as input to magnetic modeling routines.

3.3.2 Magnetic modeling

Three magnetic modeling techniques were used to evaluate the source of the observed magnetic anomalies. As a first step, we performed a linear least-squares inversion (Plouff, 1976) in which the source body is approximated by a stack of

polygonal prisms that follow the top of basalt (Fig. 17) and is assumed to have a homogeneous magnetization. As magnetic lineations were found across Ori Massif, this homogeneous model is implausible, but this model helps us to understand the anomaly produced by the volcanic edifice as a whole (Fig. 18). The "goodness-of-fit" ratio (GFR), the ratio of the mean observed anomaly divided by the mean residual (observed field minus calculated field), and correlation coefficient (calculated versus observed anomaly) were used to judge the degree to which the model mimics the observed field. For the GFR, a large number indicates a good fit; whereas for the correlation coefficient, a number approaching the maximum value of one does the same.

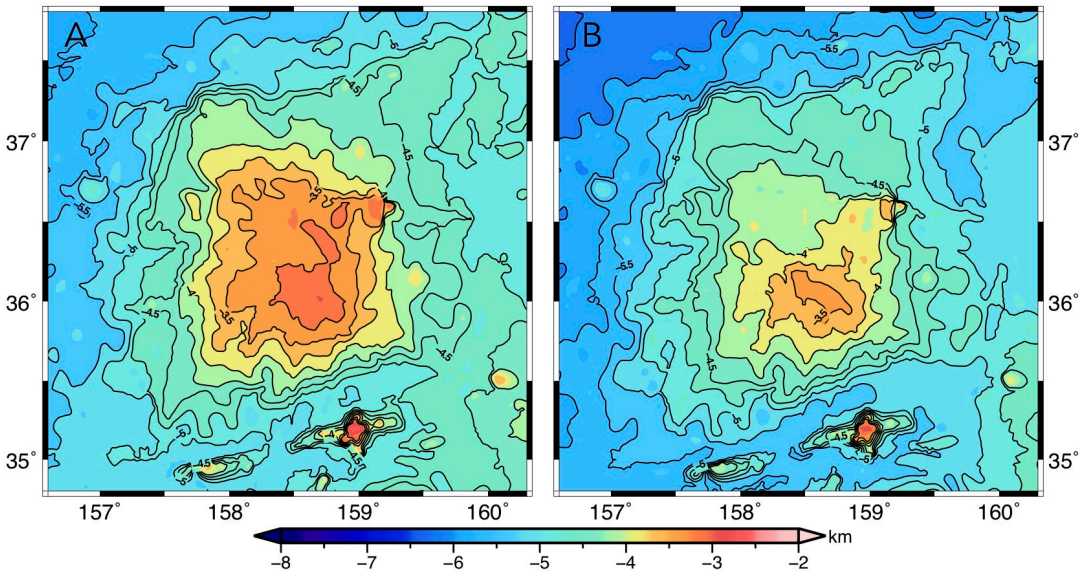

Figure 17. (A) Bathymetry and (B) igneous basement depth maps for Ori Massif. Basement is set at the interface between sediments and basalts by subtracting sediment thickness from bathymetry. Depth contours in both maps are shown at 250-m intervals and are annotated at 500-m intervals.

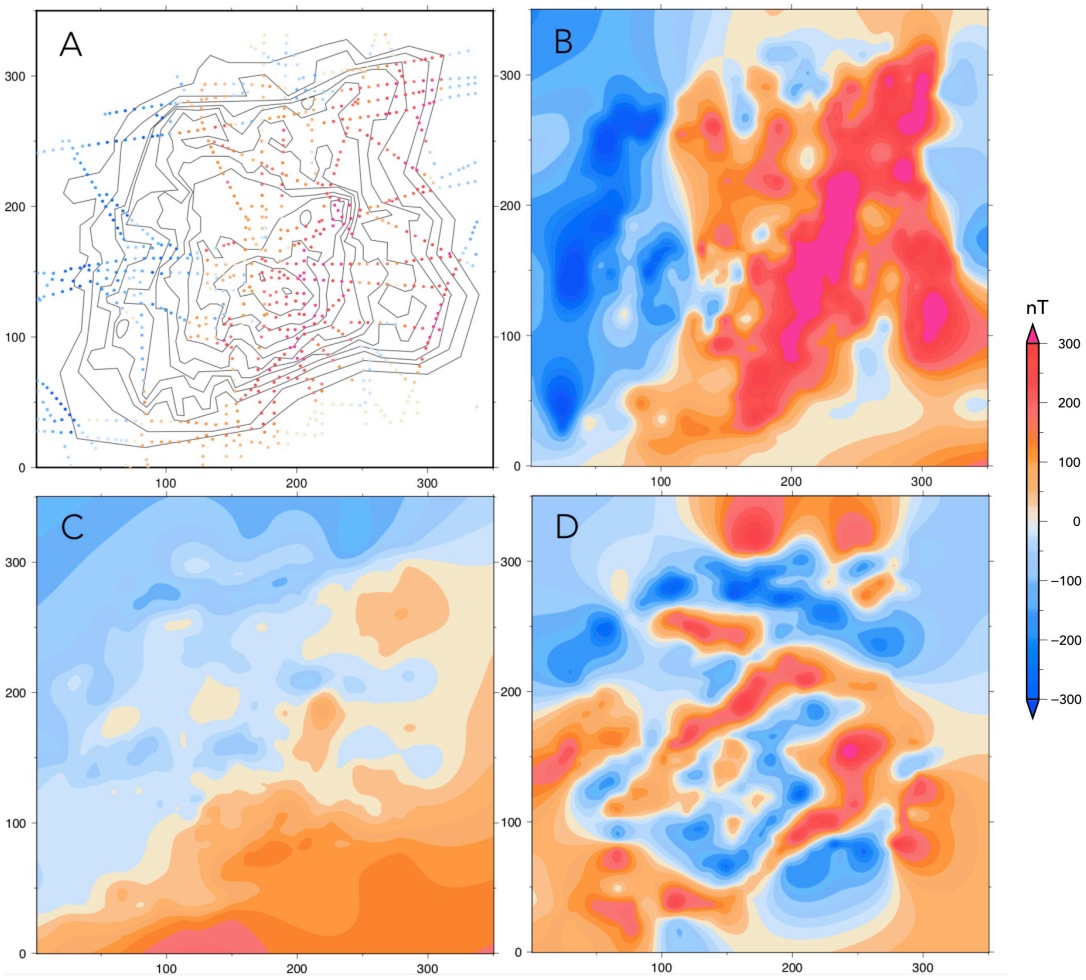

Figure 18. Results from homogeneous magnetization model (Plouff, 1976). X and Y axis denote distance with units of km. (A) Model polygons following depth contours at 200-m intervals and input magnetic anomaly points. Anomaly points are plotted with the same size but with different colors based on anomaly values. (B) Calculated anomalies from the forward model (assuming remanent magnetization inclination, declination, and intensity of 0°, 0°, and 2.7 A/m, respectively). (C) Calculated magnetic field using least-square inversion (inclination, declination, intensity = 25.3°, -31.1°, and 5.8 A/m). (D) Residual magnetic field resulting from subtracting least–square inversion model from observed anomalies.

Two Fourier inversion techniques were used in this study. One assumes a uniform source layer thickness (Parker and Huestis, 1974). Another is an extension of this routine, which allows a variable source layer thickness (Caratori Tontini et al., 2008). The top of the model is set at the interface between sediments and basalt (Fig. 17), determined from multichannel seismic profiles (Zhang et al., 2015) and a database derived from single channel seismic profiles (National Centers for Environmental Information (NCEI); https://www.ngdc.noaa.gov/mgg/sedthick/sedthick.html).

Many models for marine magnetic anomalies assume a thin source layer thickness of 0.5 to 1 km because observed magnetic anomalies are attributed primarily to the uppermost crust (seismic layer 2A) (e.g., Gee and Kent, 2007). Ori Massif's crust is approximately three times thicker than normal oceanic crust (Zhang et al., 2016) and it rises about 3 km above the surrounding abyssal plain (Sager et al., 1999). Thus, the source layer of the uniform thickness model was set to be 3 km thick, representing the upper igneous crust of the volcano. This thickness assumption mainly affects the derived magnetization amplitude, but the spatial pattern is affected little. Seismic tomography of Tamu Massif suggests that the bottom of the upper crust is nearly horizontal (Korenaga and Sager, 2012). Ori Massif is a similar volcano, so the bottom for the variable thickness model was assumed to be flat and 1 km below the abyssal seafloor, i.e., a depth of 7.5 km.

Both models used declination of -2.6° and inclination of 48.4° as ambient field direction, calculated from the IGRF at the center of Ori Massif. Magnetization is assumed to be entirely remanent because dredged and drilled seamount basalts usually

have remanent magnetization that are ~10 times larger than the induced magnetization (Harrison et al., 1975). Paleolatitudes measured from core samples recovered at two IODP drill sites (U1349 and U1350) place Ori Massif near the equator during its formation (Sager et al., 2015). Declination cannot be determined from these azimuthally-unoriented core samples; however, Cretaceous Pacific paleomagnetic poles imply declinations that range from near zero to several tens of degrees positive (clockwise) (Larson and Sager, 1992). Given these results, a reasonable starting assumption for remanent inclination and declination is zero for both. Nevertheless, this assumption must be treated with caution owing to paleomagnetic data uncertainties. Moreover, both modeling routines do not give reliable results with zero inclination. Therefore, we used low, but non-zero inclination values (±10°, ±20°) in our models. Different positive and negative declinations (±30°) were also tested to find results that best mimicked the input data. Ultimately, the model with -20° inclination and 20° declination was selected as an adequate representation of the observed anomaly. Other models with slightly different inclination and declination values also give reasonable results, but choosing a different alternative does not change our findings.

3.4 Results

3.4.1 Magnetic anomaly map

After corrections, the mean of magnetic anomaly COEs was reduced from 24.94 nT to 3.75 nT. Similarly, the COE root mean square (RMS) improved from 102.66 nT to 37.65 nT. The cleaned dataset was used to construct a magnetic anomaly map (Fig.

19A), which is mainly characterized by linear magnetic anomalies, even at the summit of Ori Massif. Five positive anomalies and four intervening negative anomalies appear to pass through Ori Massif with a NE-SW trend, consistent with the nearby Japanese lineations (Nakanishi et al., 1999). This trend is disrupted by several anomalies with discordant patterns around the edge of Ori Massif. Prominent are the broad negative bight (an inverted "V") to the north of Ori Massif and a parallel, NW-SE trending positive anomaly on the northeast flank. In addition, an E-W trending positive anomaly runs along the southern border of the map.

At first glance, magnetic lineations in our anomaly map fit well with isochrons picked by Nakanishi et al. (1999). The E-W trending anomaly at the southernmost edge of the study area was identified by Nakanishi et al. (1999) as the northern curve of an M18 bight. Going northward, M18 and M17 show different trends with a wedge-shape gap between them, interpreted by Nakanishi et al. (1999) as evidence of a NE jump of the P-F-I triple junction. Farther northward, lineations M17 to M14 follow a NE-SW trend through the Ori Massif. M16 and M15 bracket the summit of Ori Massif and our new map reveals that the trend of M15 is slightly different from that mapped by Nakanishi, with a trend of N45°E, similar to M16 and M17. In addition, with constraints from new data, the short M15 isochron on the west side of the map appears to extend farther westward than mapped by Nakanishi et al. (1999). The M14 isochrons appear as identified by Nakanishi et al. (1999), depicting two segmented lineations on the north flank. Farther north, several poorly-defined Japanese lineations have NE-SW trends.

Although the map agrees well with previously defined magnetic anomalies, it shows some new features of anomaly width and patterns. The most distinct feature is the broad negative magnetic bight encompassing the north flank of Ori Massif, which was not recognized by picking positive anomaly peaks (Nakanishi et al., 1999). This feature is puzzling as it disturbs the overall NE-SW trending lineations within and around Ori Massif. Its existence, however, is not arguable because it is well-constrained by many ship tracks, especially the two new ship tracks near 37°N, 157.2°E (Fig. 16A), which constrain the extrapolation of the west arm of the bight. The new map also delineates a NW-SE trending positive lineation east of M16 and M15. Along with M14, this lineation appears to form a positive bight similar in shape to the broad negative bight. Unfortunately, we cannot trace this positive bight on the west side of Ori Massif due to the lack of data around 36.7°N 157.5°E. Nevertheless, it may well be that this anomaly is connected with that identified as M15 at 36.3°N, 157.5°E.

Another difference occurs at the summit of Ori Massif Where M16 was identified by Nakanishi et al. (1999). According to Figure 16, a cluster of new ship tracks lie over this summit area, so the shapes of these anomalies are well-resolved. The map shows the low-amplitude M16 lineation identified by Nakanishi et al. (1999) at 35.6°N, 158.7°E and that it is paired with another low-amplitude lineation at 36°N, 158.5°E, which was not identified by Nakanishi et al. (1999). Although the trends of these two lineations are slightly different, they are similar in shape and amplitude. Nakanishi et al. (1999) extended M16 eastward to 36.2°N, 159.6°E, where the new map shows a rounded positive anomaly with high amplitude. The separation of this rounded

anomaly from the summit M16 lineation is confirmed by a new ship track that recorded negative anomalies between the two (Fig. 16). One problem with the round anomaly is that it is only constrained by two E-W trending ship tracks, so N-S control is poor. Thus, its exact trend and pattern remain unclear and the gridding algorithm artificially connects it southward with M17.

The paucity of data around 35.5°N, 157°E allows the gridding algorithm to construct a misleading broad positive zone at the southwest corner of our study area. With the help of new ship tracks around 35.1°N, 158.25°E gridding connects the M17 lineation at the southeast boundary of Ori Massif with another M17 lineation at the southwest side of the massif. Where Nakanishi postulated an offset, the lineation is much wider than others in the area. However, this appears to be a gridding artifact and around 35°N, 158.5°E there are two linear seamounts (Fig. 17), which may distort nearby magnetic lineations.

3.4.2 Modeling results

3.4.2.1 Homogeneous model

The best fit magnetization vector obtained from the least-squares inversion (Plouff, 1976) has an inclination of 25.3° and a declination of -31.1° (Figs. 18C, 18D). The remanent inclination implies a paleolatitude of 13.3°N, which is not expected as previous studies suggest that Shatsky Rise moved ~35° northward from its formation position near the equator (Sager et al., 2015). The negative declination is westward, which does not agree with Pacific apparent polar wander path data (Larson and Sager,

1992). In addition, the GFR is 1.06, which is low and means that the magnitude of the mean residual is almost the same as the magnitude of the mean observed anomaly, implying that, the homogeneous model does not explain most of the anomaly characteristics. Moreover, the model correlation coefficient is 0.38, which indicates a poor match of observed and calculated anomalies (Fig. 18). Residual anomalies (Fig. 18D) are similar to the input anomaly, showing that the homogeneous model does a poor job of explaining observed anomaly features.

3.4.2.2 Uniform thickness inverse model

The pattern of the magnetization structure derived from the uniform thickness model is similar to the pattern of the magnetic anomaly map (Fig. 19). The study area is predominantly characterized by linear magnetization zones, among which negative zones correlate to positive anomaly lineations and vice versa. The trend of the magnetization lineations is slightly more northward than that of the observed magnetic anomalies, however, we found that magnetization lineation trends were highly dependent on the assumed, but poorly known remanent magnetization declination. Greater modeled declinations produced greater lineation azimuths. This may indicate that Early Cretaceous paleomagnetic poles located farther west are preferred (e.g., Larson and Sager, 1992). These linear magnetization zones appear to traverse the topographic contours, similar to the magnetic anomaly lineations. Additionally, the magnetization lineations within Ori Massif have similar trends to the Japanese lineations to the north.

Although most parts of Ori Massif show linear magnetization zones with no obvious relationship to the underlying topography, after inversion one feature appears to be inconsistent with this scenario. The normal magnetization zone at the summit of Ori Massif, which encompasses two low-amplitude M16 reversed polarity lineations, displays a similar shape to the summit topographic contours (e.g., -4 km contour, Fig. 19).

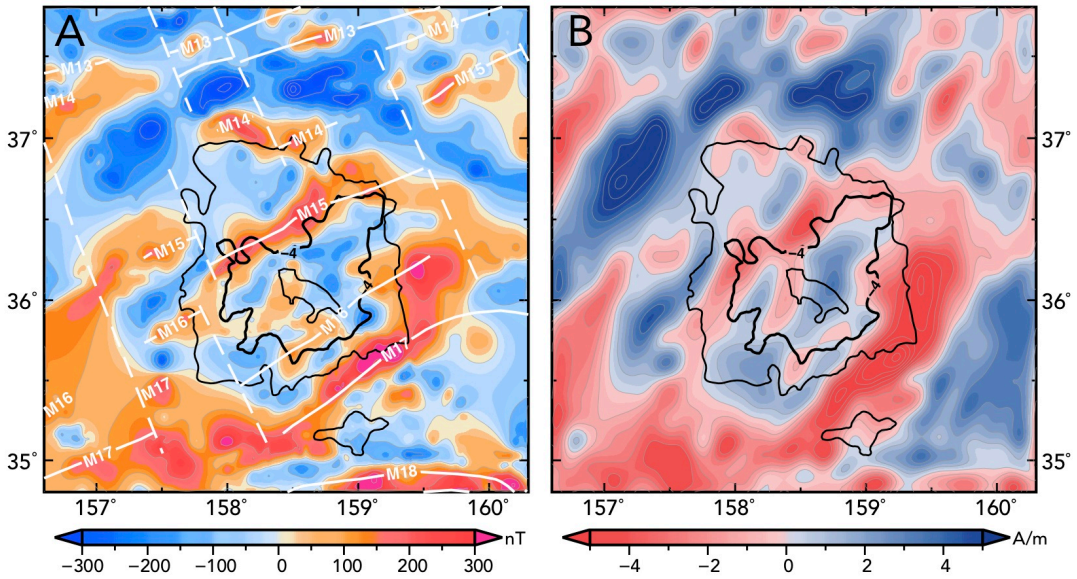

Figure 19. Uniform-thickness layer magnetic inversion model (Parker and Huestis, 1974). (A) Magnetic anomaly map of Ori Massif. Black dotted lines show basement contours from 3.5 km to 4.5 km around the center of Ori Massif. White annotated lines and d dashed lines denote magnetic isochrons and fracture zones identified by Nakanishi et al. (1999), respectively. (B) Calculated magnetization map resulting from the uniform-thickness inverse model (Parker and Heustis, 1974). The assumed remanent magnetic field direction is inclination, -20°, and declination, 20°. Black dotted lines are basement depth contours for reference.

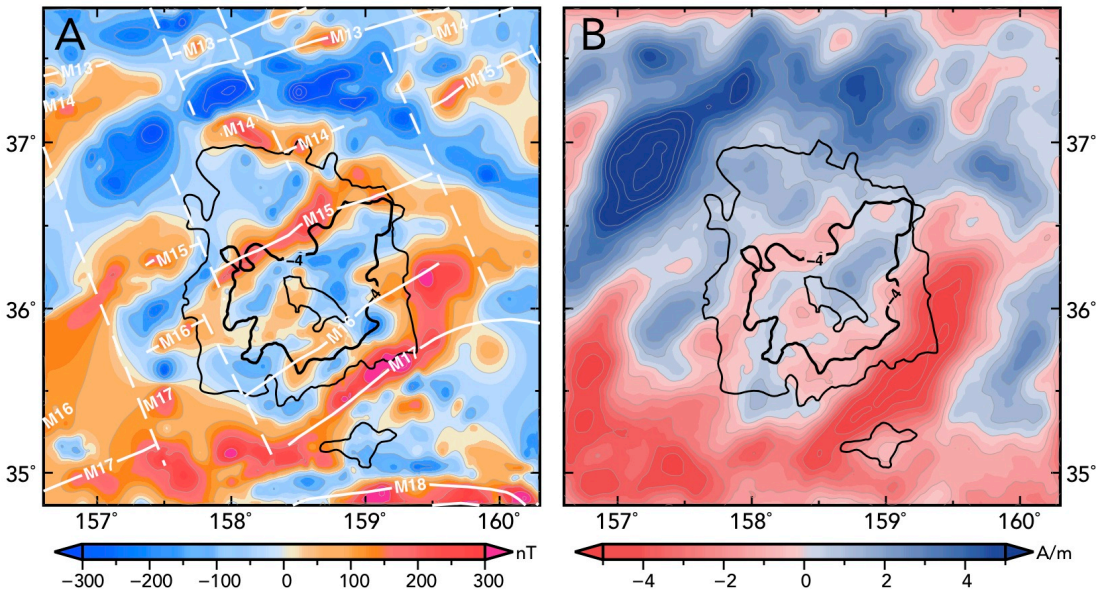

Figure 20. Variable-thickness layer magnetic inversion model. A) Magnetic anomaly map for Ori Massif. B) Calculated magnetization map resulting from the variable thickness inverse model (Caratori Tontini et al., 2008). Contours and annotations are the same as Figure 19.

3.4.2.3 Variable thickness inverse model

The general pattern of the magnetization map given by variable thickness model is similar to the result of uniform thickness model, with the most notable difference being the higher amplitudes of lower flank magnetizations and lower amplitudes of summit magnetizations (Fig. 20). This mainly arises from the different thickness assumptions between the two models. For the variable thickness model, the assumed thickness ranges from 5 km at the center to 1 km over the adjacent abyssal plain. As a result, the magnetization is concentrated on the lower flank and nearby abyssal plain but is spread or attenuated at the summit. For example, adjacent to Ori Massif, the maximum magnetization in the positive body at 37.0˚N, 157. 2˚E is >5 A/m compared to 3 A/m in

the uniform thickness model (Figs. 19B, 20B). Additionally, the positive magnetization at the Ori summit around 36.2˚N, 158. 6˚E is less prominent at 3 A/m in the variable thickness model compared with 4 A/m in the uniform thickness model. Otherwise, the variable thickness model confirms the observation of linear magnetization zones and that the uniform thickness assumption of the previous model did not unduly bias the magnetization interpretation.

3.5 Discussion

3.5.1 Magnetic anomaly map

With the help of new data, our anomaly map confirmed isochrons picked by Nakanishi et al. (1999) as magnetization lineations and allowed examination of the patterns and connections of the magnetic anomalies to shed light on the formation of Ori Massif. However, there are still large gaps in the survey coverage (Fig. 16), hindering the construction of a detailed anomaly map. For instance, although it is plausible that there is a positive magnetic bight adjacent to and south of the broad negative bight located north of Ori Massif, it is not continuous in the anomaly map owing to data gaps. Likewise, some isochrons and fracture zones identified by Nakanishi et al. (1999) on the flank are not seen also because of the scarcity of data. In addition, some parts of different isochrons may be artificially connected by the gridding algorithm because of local data paucity. Despite these problems, the data set is relatively dense at the center of Ori Massif, and because the lineation width within Ori Massif is relatively large (~10-20

km), the sparse data in most places do not hinder the identification of linear anomaly zones within Ori Massif, implying its formation at a mid-ocean ridge.

3.5.2 Geophysical constraints for magnetic modeling

Moho depth inferred from multichannel seismic reflection data indicates that the lower flanks of Ori Massif have crustal thickness of ~12-13 km (i.e., ~1.5 times that of normal oceanic crust) while the crust at the center has a thickness of ~25 km (i.e., triple normal oceanic crust thickness) (Zhang et al., 2016). A common assumption for the thickness of the main source layer in normal oceanic crust is 0.5-1.0 km, which is usually assumed to represent the upper crust (seismic layer 2A) (e.g., Gee and Kent, 2007). Seismic refraction data across Tamu Massif indicate that the crustal layers are approximately proportional to normal crust (Korenaga and Sager, 2012). Thus, the proportional source layer thickness assumptions for Ori Massif should be 0.75-1.5 km at the flank and 1.5-3 km at the center. In view of the above, the 3-km assumption in our uniform thickness model is reasonable for the center of Ori Massif but probably too thick for the flanks. In contrast, the flat bottom assumption in the variable thickness model is proper for the flank and surrounding seafloor where assumed crustal thickness is about 1 km, but is probably too large for the center of Ori Massif where model thickness is ~5 km. Both models are simplified as we have no data to estimate the bottom boundary of the upper crust. Consequently, in both models, where the crustal thickness is over-estimated, inverted magnetization values are reduced proportionally (Figs. 19, 20). Even so, changing assumed crustal thickness mainly results in changes in

the magnetization amplitude but not the structure, which is affected little by thickness. Both models capture the pattern of the magnetic structure, that is, linear magnetization zones predominantly characterize Ori Massif.

3.5.3 Volcanism at Ori Massif

Bathymetry of Ori Massif indicates that it is sub-circular in plan view, similar to the structure of many central volcanoes (Sager et al., 1999). Furthermore, seismic structure suggests that Ori Massif is a central volcano with low flank slopes (Sager et al., 2016; Zhang et al., 2015). For such a massive volcano, voluminous magma outpouring from a central vent or vents would not be expected to form linear pattern of magnetic anomalies. Instead, anomalies should reflect the shape of the volcano if the magnetization is homogenous or show high complexity (i.e., short-wavelength features) where zones of opposite polarity are juxtaposed. In studies of magnetic modeling of smaller seamounts, if a volcano formed during just one polarity period (i.e., homogeneously magnetized), the magnetic anomaly usually looks like a dipole (e.g., Harrison et al., 1975; Sager et al., 1993). If a seamount erupted over multiple polarity periods, its anomaly pattern is complicated by a vertical or complex stack of normal and reversed magnetizations whose anomalies interfere (Sager et al., 1993; 2005). However, this is not observed over Ori Massif, where the magnetic lineations are coherent and dominantly linear.

Linear magnetic anomalies over and around Ori Massif resemble those commonly observed at mid-ocean ridges (Vine and Matthews, 1963). Moreover, these

lineations are not deflected at topographic contours, implying that topography does not control these lineations. In addition, the trend of the magnetic lineations within Ori Massif appear to be coherent and nearly parallel to the orientation of the adjacent Japanese lineation set (Nakanishi et al., 1999), suggesting that Ori Massif's emplacement occurred at the west arm of the P-F-I triple junction, the Pacific-Izanagi ridge. Finally, if the isochrons identified by Nakanishi et al (1999) are correct, Ori Massif's formation started at the south side around M17, and ended along the north side around M14, a time span of ~4 Myr from 142.6 to 138.7 Ma (Ogg, 2012).

The magnetic modeling performed in this study further corroborates Ori Massif's formation as a mid-ocean ridge. The homogeneous model presents broad, coherent anomalies over Ori Massif and residual anomalies (observed anomalies minus calculated anomalies) show that lineations are not explained by this model (Fig. 18). This result rules out a homogeneous magnetization for Ori Massif. The Fourier inversion results of the uniform thickness model and variable thickness model both represent the magnetic lineations as alternating blocks of normal and reversed polarity magnetization (Figs. 19, 20), similar to crustal accretion along seafloor spreading centers (e.g., Gee and Kent, 2007). The linearity of the magnetic anomalies and their close resemblance to seafloor spreading anomalies in adjacent basins suggest that volcanic eruptions contributing to Ori Massif's construction were mostly confined to a narrow zone along the spreading axis, with limited off-axis reach of lava flows. This is the essential characteristic of mid-ocean ridge crustal accretion that allows these plate boundaries to record coherent and linear magnetic anomalies (Gee and Kent, 2007).

Nevertheless, some discordant patterns do exist, suggesting that Ori Massif's formation is not precisely the same as normal formation of oceanic lithosphere at mid-ocean ridges. Although magnetic lineations within Ori Massif align reasonably well with the Japanese lineation set, the trend is ~N45°E within Ori Massif, but outside the edifice the trend is ~N65°E, with the difference most notable on the south flank of the edifice (Fig. 19A). In that area, the trend of M17 diverges significantly from that of M18 farther south, possibly owing to a jump of the P-F-I triple junction occurred between those isochrons (Nakanishi et al., 1999).

Another anomalous feature is the extra positive anomaly between M16 and M15 at the Ori Massif summit (Fig.19A). This small, linear anomaly is not included in the geomagnetic polarity time scale (e.g., Gee and Kent, 2007; Ogg, 2012). Moreover, the two low-amplitude M16 lineations at the summit of Ori Massif have similar shapes and anomaly intensities and the spacing between M17 and M15 is unexpectedly large. The two repeated anomalies suggest a small, northwestward jump of the Pacific-Izanagi ridge which captured a second version of M16 on the Pacific plate.

On the north side of Ori Massif, there are other discordant magnetic lineations departing from the Japanese lineation trend. A prominent negative anomaly forms a magnetic bight, with the apex at 37.3°N, 158.0°E and arm trends of N45°E and N110°E (Fig. 19A). Furthermore, positive anomalies immediately south of the negative bight have a similar shape, although this positive magnetic bight is not completely connected owing to the paucity of data (Figs. 16, 19). This pair of magnetic bights imply two ridges connected to a triple junction (e.g., Nakanishi et al., 1999). However, the interpretation

of these magnetic bights is complicated because it is difficult, with only one pair of anomalies, to decipher how this triple junction relates to the P-F-I triple junction, which was probably farther northeast at the axis of Shatsky Rise (Nakanishi et al., 1999). Additionally, the isochrons within Ori Massif are consistent with the nearby Japanese lineations and they appear to be successive (Nakanishi et al., 1999), but the magnetic bights north of Ori Massif do not fit this trend. Instead, they suggest a short-lived triple junction. A mechanism that can explain multiple triple junctions in a small region is a microplate (e.g., Bird et al., 1998). Indeed, it has been suggested that anomalous spacing of magnetic lineations around Shatsky Rise exist because of microplates that were attached to the Pacific plate by the spreading reorganization that occurred at the time of its origin (Sager et al., 1988; Nakanishi et al., 1999). Given the complex tectonics that occurred along the path of the P-F-I triple junction and the poor coverage of magnetic data over abyssal seafloor around Ori Massif (Nakanishi et al., 1999), we do not attempt to reconstruct ridge configurations at the time of Ori Massif formation because this model would be highly speculative and likely misleading.

Although most of Ori Massif is characterized by magnetic lineations, the three-dimensional magnetic structure at the summit of Ori Massif is partially consistent with topographic contours. The M16 lineation and another positive anomaly to its north, along with negative lineations that surround them, all trend parallel to the -4 km basement contour (Fig. 19), implying that near the Ori Massif summit, lineation trend is affected by topography, perhaps because of the shallowness of the summit.

Linear magnetic anomalies passing through high basaltic edifices and related linear source blocks are also found in other plateaus, such as Iceland, the Azores, and Roo Rise (Fullerton et al., 1989; Ryan 1990; Gente et al., 2003). The center of Iceland is actively spreading, showing that present volcanic eruptions along the rift zone are split into the western and eastern sides of the edifice (Jonsson et al., 1991; Kristjansson and Jonsson, 2007). The internal structure of the magma transport system beneath Iceland suggests that the Mid-Atlantic Ridge influences the magma system down to a depth of ~175 km (Ryan, 1990). In addition, azimuthal anisotropy and phase velocity beneath Iceland imply that hot, buoyant flow appears channeled along the Mid-Atlantic Ridge from at least 100 km underneath the island (Li and Detrick, 2003).

In the crust, feeder dikes arise from the axial magma chambers (AMC), forming fissure eruptions (Sinton and Detrick, 1992; Gudmundsson, 2012). This is a mechanism consistent with crustal structure at fast spreading centers, where 2D upwelling dominates the neovolcanic zones (Macdonald, 1982; Karson, 2002). At slow spreading centers, long-term AMCs are rarely developed and 3D upwelling complicates the crustal formation (Macdonald, 1982; Parmentier and Morgan, 1990; Mutter and Karson, 1992). Some numerical models attribute the different crustal accretion and mantle upwelling patterns to be spreading-rate dependent (Parmentier and Morgan, 1990; Lin and Morgan, 1992; Morgan and Chen, 1993), while other studies argue that the volcanic emplacement processes are primarily controlled by local magma supply (Carbotte et al., 1998; Colman et al., 2012; McClinton and White, 2015). Iceland and the Azores Plateau both formed at slow spreading centers but exhibit magnetic lineations passing though the topographic

highs, partially owing to the excess magma supply and steady-state magma feeder along the rift zone. Ori Massif was formed at a fast spreading center, likely with a large magma supply, thus steady-state 2D upwelling along the ridge axis formed linear magnetized source blocks.

Another requirement for linear crustal accretion is that new linear eruptions should split a preexisting weak zone along the axial feeding system. This is the common view of the spreading process at mid-ocean ridges (Macdonald, 1982). However, as aforementioned, the summit of Ori Massif presents some 3D magnetic structure. Ori Massif formed with anomalously thick ocean crust at a ridge (Zhang et al., 2016). A widely accepted mechanism to explain this type of oceanic plateau is hotspot-ridge interaction with anomalously voluminous melting to explain the thickened crust and elevated seafloor of oceanic plateaus, such as Iceland and Azores plateau (Wilson, 1963; Ito et al., 1999; Gente et al., 2003). The same may have occurred at Ori Massif. Whereas, the source depth of the melting anomaly at Ori Massif is unknown due to the lack of related geophysical constraints. Iceland, as a large volcanic edifice, has been attributed to the result of a mantle plume (Bijwaard and Spakman, 1999). The plume model, however, is debated and decompression melting of shallow fertile mantle is also proposed to explain the excessive magma supply beneath Iceland (Foulger et al., 2005). Without geophysical constraints for the deep internal structure of Ori Massif, whether excess magma resulted from a mantle plume is unclear. In addition, Ori Massif formed within a time period of ~4 Ma at a fast spreading ridge, whereas Iceland was emplaced at a slow spreading ridge over a longer time interval of ~17-18 Ma. This difference may

explain why the anomalies within Ori Massif are wider and more coherent than those within Iceland (Ryan, 1990).

Another question is why is there no far-traveling lava flows away from the axial volcanic zone that degrades the linear pattern of the narrow crustal accretion zone? One explanation is that the magma supply is not high enough. Icelandic crust is predicted to be more than 60 km thick due to high plume temperature (Ito et al., 2003; Ruedas et al., 2004). In contrast, actual melt generation beneath Iceland is not as large as predicted (~20-40 km) and magma viscosity is increased by mantle dehydration (Hirth and Kohlstedt, 1996; Ito et al., 1999). Another possibility is that, as more newly-formed crust piled up, a feedback mechanism changes the thermal conditions underlying the volcano, decreasing the melt production (Schmeling and Marquart, 2008). Thus, although Ori Massif's crustal thickness indicates excess magma supply, the melt production was nevertheless not large enough to allow the eruptive lavas move significantly away from the axial zone to destroy the linear and narrow pattern of the crust accretion zone. Indeed, IODP drill cores yielded core samples of thin massive flows (Site U1349) and pillow lavas (Site U1350), both of which indicate a modest rate of extrusion (Sager et al., 2011b).

3.6 Conclusions

We compiled a large and heterogeneous magnetic dataset around Ori Massif and constructed a magnetic anomaly map to provide clues about the formation mechanism of Ori Massif. The magnetic anomaly map agrees with the prior isochron map, showing

magnetic lineations predominantly characterize Ori Massif, with isochrons M16 and M15 cutting through the center of the edifice. In addition, we found another low-amplitude positive anomaly within the summit of the massif, which suggests a repeated M16 caused by a ridge jump. Magnetic modeling results represent the linear anomalies as a result of alternating normal and reversed polarity blocks. This mechanism is consistent with that observed at mid-ocean ridges where crustal accretion is confined within a narrow zone at the ridge axis. If the isochron pattern is correctly identified, Ori Massif took ~4 Ma to form and the south flank is older than the north flank.

Discordant anomaly patterns are noted in the study area, suggesting that Ori Massif's emplacement was slightly more complex than simple mid-ocean ridge volcanism. At the summit, minor 3D anomaly structure was found to follow the -4 km basement contour. Lineations within Ori Massif show a trend of N45°E, slightly different from the N65°E trend of the surrounding Japanese lineations. Moreover, Ori Massif is bracketed by two magnetic bights, implying two triple junctions. The previously-recognized P-F-I triple junction, formed magnetic bights to the south of Ori Massif, whereas newly-recognized bights on the north flank imply another triple junction at that location. These observations may be explained if Ori Massif formed on a small microplate.

Ori Massif is similar to other oceanic plateaus that formed at spreading ridges. Although magnetic lineations are often distorted within other oceanic plateaus, those within Ori Massif are remarkably clear, probably because it formed at a fast-spreading ridge. Despite the fact that large size and the thickened crust of Ori Massif implies

excessive volcanism, the flows must not have travelled far away from the axis center to overwhelm the linear pattern.

CHAPTER IV

MAGNETIC ANOMALY MAP OF TAMU MASSIF IMPLIES ITS FORMATION BY SEAFLOOR SPREADING

4.1 Overview

Tamu Massif is an immense Mesozoic submarine volcano in the northwest Pacific and the main edifice of the Shatsky Rise oceanic plateau. It was hypothesized to be an immense, central, shield volcano based on its morphology and internal structure implied by seismic data. Magnetic lineations surrounding Tamu Massif suggest its formation at a triple junction of spreading ridges, but it is unclear how such a massive volcano can form in this setting. Previous studies found that magnetic lineations can be traced into the flanks of Tamu Massif, but it is uncertain whether lineations extend into the center of Tamu Massif. The magnetic anomaly pattern should be dipositive because spreading ridges and a central volcano should yield different patterns. More than 4.6×10^6 data points from 54 geophysical surveys were merged to create a magnetic anomaly map for Tamu Massif. Systematic corrections of this large and heterogeneous data were made to reduce misfits between cruise data sets. The map was improved by the addition of recent well-navigated cruises, especially FK151005 because it was an extensive magnetic survey navigated by GPS. Linear magnetic anomalies were identified across the center of Tamu Massif and were interpreted as a sequence showing a ~90º anticlockwise rotation of a segment of the Pacific-Farallon ridge at Tamu Massif. The rotation was accompanied with complex tectonics indicated by curvilinear and complex

ridge segments. Magnetic modeling indicates that the linear magnetic anomalies within and around Tamu Massif can be interpreted as alternating normal and reversed polarity magnetization blocks, analogous to those formed at spreading ridges. These findings suggest that Tamu Massif is not a normal volcano constructed by vertical stack of far-flowing lava flows, but rather was emplaced by narrowly focused volcanism along spreading ridges. Therefore, Tamu Massif is not a central volcano. Instead, it was formed by seafloor spreading and the morphology of Tamu Massif reflects the variations of crustal emplacement and thickness, rather than lava flow slopes.

4.2 Introduction

The hotspot hypothesis was developed to explain the formation of age-progressive intra-plate volcanism (Wilson, 1963). A hotspot was originally envisioned as an isolated thermal plume rising from deep in the mantle and not associated with plate boundaries. Nevertheless, many hotspots have interacted with the main source of mantle melting, the spreading ridge system. Examples include Iceland (Ryan, 1990), the Azores (Cannat et al., 1999; Gente et al., 2003), Rio Grande Rise (Cande et al., 1988) in the Atlantic Ocean; Ontong Java-Manihiki-Hikurangi complex (Taylor, 2006), Hess Rise (Sager, 2005), Magellan Rise (Tamaki and Larson, 1988) in the Pacific Ocean; Joey and Roo Rise (Gibbons et al., 2012) in the Indian Ocean. Although many examples of ridge-hotspot interaction have been found, the process is not well understood, especially in the case of oceanic plateaus.

Tamu Massif, the largest and oldest edifice in the Shatsky Rise oceanic plateau, was recently hypothesized to be a single massive shield volcano, indeed perhaps the largest single volcano in the world (Sager et al., 2013). Magnetic anomalies surrounding it suggest its formation near a triple junction of spreading ridges, making it an important site for studying hotspot-ridge interaction and its connection with oceanic plateau formation (Sager et al., 1988; Nakanishi et al, 1989, 1999).

As records of seafloor spreading, magnetic anomalies play an important role in understanding the tectonic evolution of ocean crust because of the strikingly linear pattern formed by spreading ridge volcanism (Vine and Matthews, 1963; Gee and Kent, 2007). In contrast, magnetic anomalies over central volcanoes usually have a different pattern, either a simple dipolar anomaly for volcanoes with uniform magnetization or highly complex for those that encompass magnetic reversals (Harrison et al., 1975; Sager et al., 1993; 2005). Because of this difference and the fact that it formed during a period of frequent magnetic reversals, magnetic anomalies over Tamu Massif should be diagnostic of its formation mechanism. New magnetic data collected by recent surveys prompts a re-examination of magnetic anomalies over Tamu Massif.

In this study, we compiled a large and heterogeneous magnetic data set to construct a magnetic anomaly map for Tamu Massif. Surprisingly, the massif, even at its center, is predominately characterized by linear or curvilinear magnetic anomalies, analogous to those observed at spreading ridges. To further study the nature of the magnetic source, we performed magnetic models to estimate the internal magnetic structure of the large volcano. Modeling results suggest that massive eruptions at Tamu

Massif are confined to a narrow zone along the axis of the spreading ridge. That is to say, the topography of the massive volcano shows little influence on the formation of the magnetic anomalies.

4.2.1 Geological setting of Tamu Massif

Tamu Massif is the largest and oldest edifice in the Shatsky Rise oceanic plateau located in the northwest Pacific Ocean. With an area of ~3.1×10^5 km^2, it is comparable in size with the largest volcano in the solar system (i.e., Olympus Mons on Mars), and appears to be the largest single volcano on Earth (Sager et al., 2013). Tamu Massif is mainly elongated southwest to northeast, but a low westward extension departs from this trend (Sager et al., 1999). The northern flank of Tamu Massif displays several curved topographic highs that follow the trends of the magnetic bights across it (Nakanishi et al., 1999; Sager et al., 1999) (Fig. 21). Its center is characterized by two highs, the shallower being Toronto Ridge.

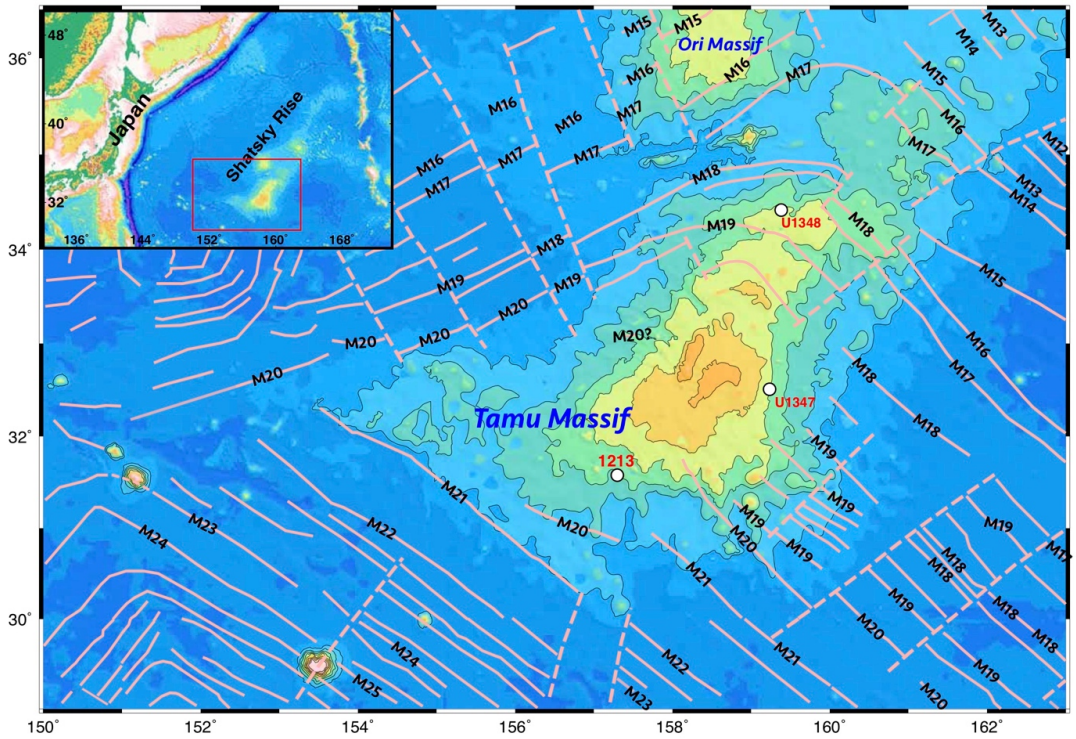

Figure 21. Location, bathymetry and magnetic lineations of Tamu Massif. Bathymetry (Smith and Sandwell, 1997) shallower than -5 km is illustrated with contours at 0.5-km intervals. Magnetic isochrons and fracture zones are denoted as solid and dashed pink lines, respectively, following Nakanishi et al. (1999) and Nakanishi et al. (2015). White filled circles show the locations of the Ocean Drilling Program Site 1213 as well as Integrated Ocean Drilling Program Sites U1347. Inset map shows the locations of Shatsky Rise and Tamu Massif in the northwest Pacific Ocean.

Multichannel seismic (MCS) data from Tamu Massif show lava packages sloping downward only from its summit, implying that it is a single central volcano (Sager et al., 2013; Zhang et al., 2015). The basement interface and intra-basement reflectors display anomalously low slopes (< 1º), similar to Iceland, and were explained by lava flows of low viscosity combined with high eruption rate and volume (Sager et al., 1999; Sager et al., 2013; Zhang et al., 2015). Seismic tomography from refraction data (Korenaga and Sager, 2012) and the Moho structure inferred from MCS data and isostasy (Zhang et al.,

2016) both suggest that the crustal thickness of Tamu Massif is much thicker (~30 km) than normal oceanic crust (~7 km average), similar to other oceanic plateaus and large igneous provinces, such as Ontong Java Plateau (Coffin and Eldholm; 1994; Korenaga, 2011) or Iceland (Staples et al., 1997; Foulger et al., 2003).

Igneous rocks from Tamu Massif were recovered by drilling at Ocean Drilling Program (ODP) Site 1213 and Integrated Ocean Drilling Program (IODP) Site U1347 (Shipboard Scientific Party, 2002, Sager et al., 2011) (Fig. 21). Core samples from these two sites both recovered thick massive flows (Koppers et al., 2010; Expedition 324 Scientists, 2010) analogous to those found at Ontong Java Plateau (Shipboard Scientific Party, 2001) and continental flood basalts (Self et al., 1997). The massive flows are thin or replaced by pillow lavas on the two smaller massifs in Shatsky Rise (Ori and Shirshov massifs), suggesting a diminution of effusive volcanic eruptions as Shatsky Rise evolved (Sager et al., 2011a). This trend coincides with a decrease in edifice volume, thought to represent the waning of the Shatsky Rise mantle plume, perhaps as a transition from plume head to plume tail (Nakanishi et al., 1999; Sager et al., 1999; Sager, 2005; Sager et al., 2011). The geochemical and isotopic signatures from core samples, however, fail to provide unequivocal evidence favoring the mantle plume hypothesis. The chemical compositions of basalts recovered from Site 1213 and Site U1347 are similar to normal mid-ocean-ridge-basalts (N-MORB) (Mahoney et al., 2005; Sano et al., 2012; Husen et al., 2013).

Because SW-NE trending Japanese lineations and NW-SE trending Hawaiian lineations converge at Tamu Massif, it was suggested that Tamu Massif formed near the

Pacific-Farallon-Izanagi (P-F-I) triple junction (Larson and Chase, 1972; Sager et al., 1988; Nakanishi et al., 1989, 1999). The initiation of the emplacement of Tamu Massif was sometime after M21 (~149 Ma, herein we use the time scale of Ogg, 2012) because Chron M21 follows the southwest boundary of Tamu Massif (Fig. 21). The magnetic isochron map also implies that the formation of Tamu Massif began at the time of an ~800 km eastward jump of the P-F-I triple junction (Sager et al., 1988). In addition, the formation of Tamu Massif is associated with a large spacing between M20 and M19, interpreted as a ridge jump (Nakanishi et al., 1999).

Sager and Han (1993) modeled the magnetic anomaly of Tamu Massif, with its broad central positive and flanking lows, concluding that the magnetization was mainly negative, implying a long period of reversed polarity. Using M17, the longest reversed polarity period near the formation of Tamu Massif, they calculated a high effusion rate ($1.7\ km^3a^{-1}$) for the formation of the bulk of Tamu Massif, supporting the idea that it was formed by a massive magma pulse related to a mantle plume head. As no lineations were traced across the center of Tamu Massif, Nakanishi et al. (1999) proposed that the formation of Tamu Massif began off ridge and that its massive eruption caused the ridge to jump toward it.

A number of magnetic lineations have been identified as traversing the lower flanks of Shatsky Rise (Nakanishi et al., 1999). Of particular note is that some magnetic bights (M19-M18) were traced across the northern flank of Tamu Massif (Fig. 21). Additionally, a few magnetic lineations were traced into the southeast flank of Tamu Massif.

Age constraints for Tamu Massif are few, yet yield important implications for its formation. The lower lava groups recovered by IODP Site U1347 yield $^{40}Ar/^{39}Ar$ radiometric ages of 143-145 Ma (Geldmacher et al., 2014; Heaton and Koppers, 2014; Tejada et al., 2016), consistent with the 144.6 ± 0.8 Ma $^{40}Ar/^{39}Ar$ age dated from igneous rocks in ODP Site 1213 (Mahoney et al., 2005). Furthermore, these ages are in good agreement with the ages of the M21-M19 Chrons around Tamu Massif (149-145 Ma; Ogg, 2012), indicating that Tamu Massif formed near the spreading ridges. Some radiometric ages suggest younger ages that complicate the picture of Tamu Massif volcanism. The uppermost section of the basaltic flows in Site U1347 gave a radiometric age of ~139 Ma, several million years younger than the lower lava units (Geldmacher et al., 2014). In addition, a large summit ridge (Toronto Ridge) produced a radiometric age of ~129 Ma (Tejada et al., 2016). These younger ages suggest that late-stage volcanic eruptions postdated the primary, main edifice building of Tamu Massif.

4.3 Data and Methods

4.3.1 Magnetic dataset

To construct a new magnetic data set for Tamu Massif, we collected more than 4.6×10^6 magnetic field measurements from 54 geophysical surveys (Table 4). These surveys span from 1962 to 2015, during which navigation systems and positioning accuracy greatly improved. Notable among the surveys is the 2015 cruise of R/V Falkor (FK151005), which collected ~1.7×10^6 magnetic readings over Tamu Massif along 17 parallel, N-S transects (Fig. 22). The new compilation expands that of Nakanishi et al.

(1999) with nine GPS-navigated surveys. With the addition of these 9 recent surveys, a total of 13 surveys in the dataset are positioned by GPS (Fig. 22), contributing ~71% of all the data measurements. Having these well-navigated data tracks allowed us to merge all GPS-navigated data into a "backbone" that was used to correct navigation inaccuracies in older survey data, greatly reducing inconsistencies in the data set.

The distribution of ship tracks is uneven in the study area (Fig. 22). Most of data tracks are concentrated over the center of Tamu Massif, whereas data over the northwest and southeast flanks are sparse. Thus, anomalies over Tamu Massif itself are relatively well constrained, but those on the northwest and southeast flanks and adjacent abyssal plains are poorly defined.

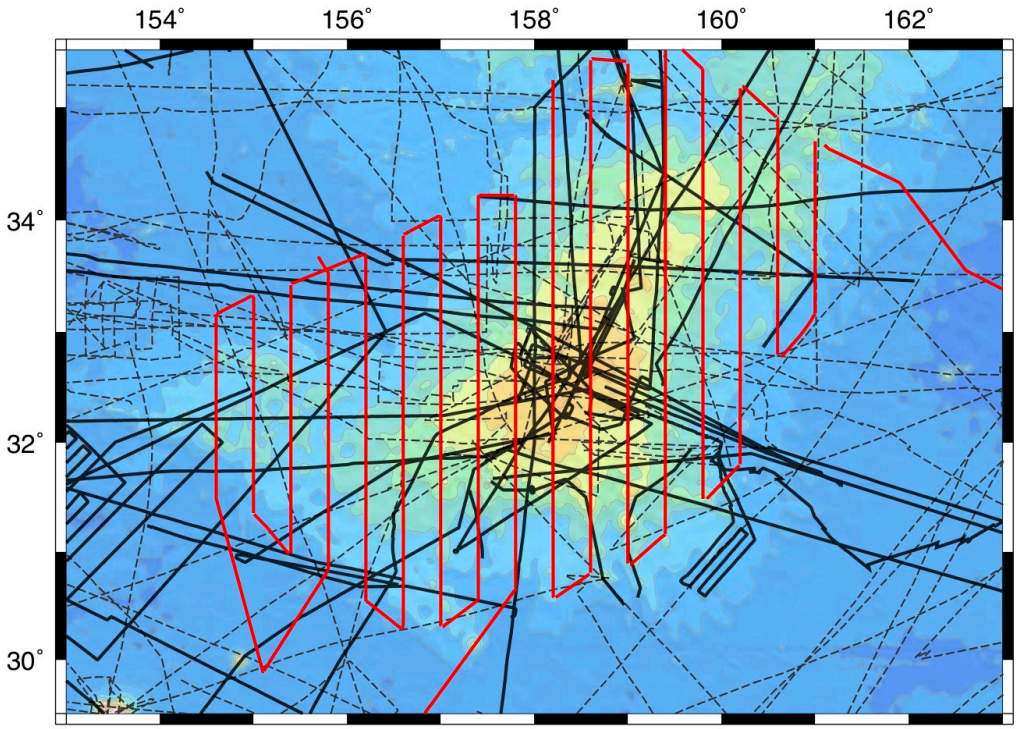

Figure 22. Magnetic ship tracks over Tamu Massif. Red solid lines show the tracks of cruise FK151005. Black solid lines show recent GPS-navigated cruises, black dashed lines denote older cruises with other, less accurate navigation systems.

Table 4. Magnetic data cruises around Tamu Massif.

Cruise ID	N1*	N2§	L@	Year	*Ship*	Institution	Navigation¶
LUSI01AR	444	444	1006	1962	*Argo*	Scripps Institution of Oceanography	Celest
V2106	27	27	117	1965	*Vema*	Lamont-Doherty Geological Observatory	Celest
V2110	227	227	1013	1965	*Vema*	Lamont-Doherty Geological Observatory	Celest
RC1007	463	463	2103	1966	*Robert D. Conrad*	Lamont-Doherty Geological Observatory	unknown
RC1008	404	403	1857	1966	*Robert D. Conrad*	Lamont-Doherty Geological Observatory	unknown
ZTES03AR	361	360	845	1966	*Argo*	Scripps Institution of Oceanography	Celest
ZTES05AR	356	355	915	1966	*Argo*	Scripps Institution of Oceanography	Celest
RC1108	30	30	128	1967	*Robert D. Conrad*	Lamont-Doherty Geological Observatory	DopSat
DSDP06GC	699	698	1172	1969	*Glomar Challenger*	Scripps Institution of Oceanography	DopSat
HUNT03HT	454	454	449	1969	*Hunt*	Scripps Institution of Oceanography	Celest
RC1219	781	780	1661	1969	*Robert D. Conrad*	Lamont-Doherty Geological Observatory	DopSat
SCAN03AR	1803	1800	3757	1969	*Argo*	Scripps Institution of Oceanography	DopSat
SILS01BT	543	543	895	1969	*Silas Bent*	Scripps Institution of Oceanography	Celest
SILS02BT	2460	2458	3778	1969	*Silas Bent*	Scripps Institution of Oceanography	Celest
ANTP03MV	876	876	1394	1970	*Melville*	Scripps Institution of Oceanography	DopSat
POL7004	879	878	3495	1970	*Oceanographer*	NOAA	DopSat
ARES05WT	541	541	935	1971	*Thomas Washington*	Scripps Institution of Oceanography	DopSat
ARES07WT	35	35	975	1971	*Thomas Washington*	Scripps Institution of Oceanography	DopSat
SI932005	7522	7522	3264	1971	*Silas Bent*	US Naval Oceanographic Office	DopSat/Loran
SI932009	4065	4065	2823	1972	*Silas Bent*	US Naval Oceanographic Office	DopSat/Loran
DSDP32GC	616	615	1136	1973	*Glomar Challenger*	Scripps Institution of Oceanography	DopSat
GECS-DMV	834	834	984	1973	*Melville*	Scripps Institution of Oceanography	Celest/Loran
KH7404	125	125	223	1974	*Hakuho-Maru*	University of Tokyo	DopSat
V3212	197	197	363	1975	*Vema*	Lamont-Doherty Geological Observatory	DopSat
INDP01WT	549	549	974	1976	*Thomas Washington*	Scripps Institution of Oceanography	DopSat
RC2004	392	392	368	1976	*Robert D. Conrad*	Lamont-Doherty Geological Observatory	DopSat
RC2005	253	253	193	1976	*Robert D. Conrad*	Lamont-Doherty Geological Observatory	DopSat
V3311	85	85	62	1976	*Vema*	Lamont-Doherty Geological Observatory	DopSat
77031705	5613	5612	2096	1977	*Kana Keoki*	University of Hawaii	DopSat
GH7901	4	4	5	1979	*Hakurei Maru*	Geological Survey of Japan	DopSat
GH801A	43	43	194	1980	*Hakurei Maru*	Geological Survey of Japan	DopSat
GH801B	156	156	336	1980	*Hakurei Maru*	Geological Survey of Japan	DopSat
V3612	834	834	1370	1980	*Vema*	Lamont-Doherty Geological Observatory	DopSat
GH814B	100	100	200	1981	*Hakurei Maru*	Geological Survey of Japan	DopSat
DSDP86GC	750	749	1101	1982	*Glomar Challenger*	Scripps Institution of Oceanography	DopSat
KH8205	4	4	84	1982	*Hakuho-Maru*	University of Tokyo	DopSat
MG21	33	33	72	1982	*Morskoy Geofizik*	Institute of Marine Geology/Geophysics	DopSat
85002211	789	789	450	1985	*Jean Charcot*	Hawaii Institute of Geophysics	GPS/DopSat
KH8803	4018	4018	1548	1988	*Hakuho-Maru*	University of Tokyo	DopSat
RNDB10WT	300	300	109	1988	*Thomas Washington*	Scripps Institution of Oceanography	DopSat
KH8902	2990	2990	1653	1989	*Hakuho-Maru*	University of Tokyo	DopSat
ODP132JR	3656	3656	1079	1990	*JOIDES Resolution*	Texas A and M University	GPS/Loran
KH9301	1160	1152	815	1993	*Hakuho-Maru*	University of Tokyo	GPS
TN037	9223	9223	1742	1994	*Thomas Thompson*	Texas A and M University	GPS
KH9603	5844	2933	925	1996	*Hakuho-Maru*	University of Tokyo	GPS
MR99K04‡	39619	663	341	1999	*Mirai*	JAMSTEC	GPS
ODP197JR‡	1489	1489	518	2001	*JOIDES Resolution*	Texas A&M University	GPS
ODP198JR‡	2950	2950	1193	2001	*JOIDES Resolution*	Texas A&M University	GPS
YK0809‡	10745	3671	1632	2008	*Yokosuka*	University of Tokyo	GPS
EXP324‡	4630	4630	1435	2009	*JOIDES Resolution*	Texas A&M University	GPS
MR0806‡	468	85	33	2009	*Mirai*	JAMSTEC	GPS
MGL1004‡	2042696	34355	7663	2010	*Marcus G. Langseth*	Lamont-Doherty Earth Observatory	GPS
MGL1206‡	381879	6373	1081	2012	*Marcus G. Langseth*	Lamont-Doherty Earth Observatory	GPS
FK151005‡	1726896	28861	7537	2015	*Falkor*	Schmidt Ocean Institute	GPS
Total	4272910	141682	71987				

N1*=total number of data points; N2§=number of data points, decimated to 1-minute (time) interval. L@=track length (km); ¶Navigation codes: Celest=celestial; Loran=Long Range (radio) Navigation; DopSat=Doppler satellite (NNSS); GPS=Global Positioning system (satellite). ‡Data not used in previous compilation[2].

4.3.2 Data processing

The following steps were performed to extract the magnetic anomaly caused by the crustal magnetic field. (1) Measured total field values were first adjusted to the 11th generation of International Geomagnetic Reference Field (IGRF11), which applies to times up to 2015 (Finlay et al., 2010). (2) Outliers and noise were identified and deleted by visual inspection of time series profiles of each survey. (3) External field signals in quiet and moderately-disturbed days (Kp index ≤ 5.0) were estimated and removed with the help of the Comprehensive Model 4 (CM4, Sabaka et al., 2004). (4) Noise and spurious readings in strongly-disturbed days (Kp index > 5.0) were identified and deleted by comparison of each survey profile with the contemporaneous Kp index curve. The Kp index is an indicator of solar flux, which is strong when solar activity is high (Dessler and Fejer, 1963). (5) Crossover errors (COE, differences where tracks interact each other) were used to evaluate the external consistency between data from different cruises. Two strategies have been applied to improve the inconsistency within our data set. First, data from each non-GPS-navigated cruise were added or subtracted by a constant offset in order to fit the aforementioned "backbone", which is comprised by recent GPS-navigated survey data. Then, straight segments of older cruises with celestial navigation system were moved around their original position (< 3 km offset) to correct the navigation errors. After these systematic corrections, the mean and root mean square of the data set COE ($Mean_{COE}$ and RMS_{COE}), respectively, were reduced from -95 nT and 2481 nT to 0.5 nT and 38 nT.

The gridding of the corrected data was achieved by two steps. First, using the GMT routine "blockmedian", the median values within every 1-arc minute block were calculated to construct a regularly spaced data set. Subsequently, using the GMT routine "surface", the output median values was gridded by continuous spline curvature with a tension factor of 0.25, a value appropriate for potential field data (Smith and Wessel, 1990). The gridded dataset was then used for the plot of a magnetic anomaly map and input for the modeling.

4.3.3 Magnetic modeling

Three magnetic modeling techniques were applied to study the magnetic structure of Tamu Massif. The first one is a repeat of Sager and Han (1993), using the least-squares inversion developed by Plouff (1976). This method represents the magnetic source as a stack of polygonal prisms, all with identical, homogeneous magnetization, whose shapes are determined by topographic contours. The top of the model was set at the interface between sediments and igneous rocks, determined by MCS profiles (Zhang et al., 2015) and a database derived from single channel seismic profiles (National Centers for Environmental Information (NCEI); https://www.ngdc.noaa.gov/mgg/sedthick/index.html, Fig. 23). Additionally, we performed a forward model to check the appearance of the magnetic anomaly if Tamu Massif was formed rapidly during just one reversal polarity time period near the equator.

The other two modeling techniques are Fourier domain inversions. One assumes a uniform thickness source layer (Parker and Huestis, 1974). The other is an extension of

this routine, assuming a source layer with variable thickness (Caratoni Tontini et al., 2008). As before, the top of both models was the top of igneous crust (Fig. 23). Because Tamu Massif is ~3 km above the surrounding abyssal plains, for the uniform thickness model, the source layer was assumed to be 3 km thick. According to seismic imaging, the bottom of the upper crust at Tamu Massif is approximately horizontal (Korenaga and Sager, 2012). Therefore, the bottom of the variable thickness model was assumed to be flat and 1 km below the abyssal seafloor, i.e., ~7.5 km in depth. This model has a thickness of ~5 km at the center of Tamu Massif.

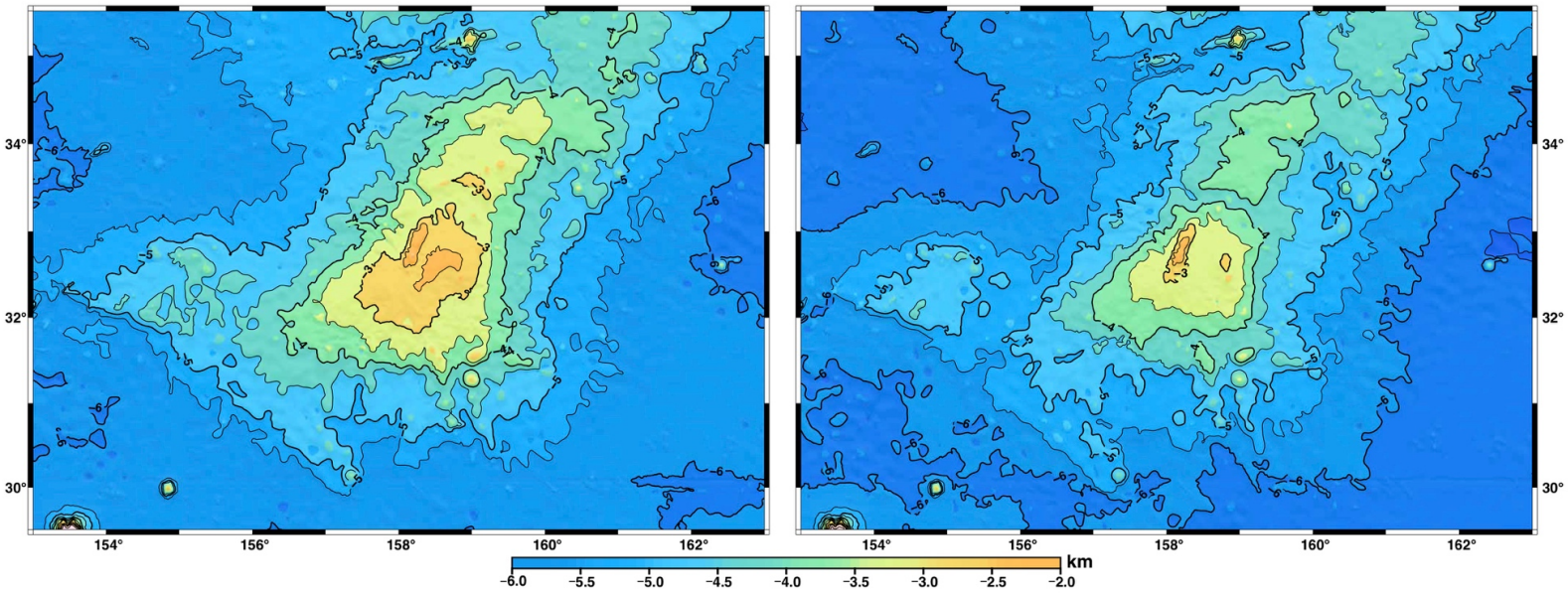

Figure 23. Bathymetry (left) and top of igneous basement (right). Basement top is produced by subtracting sediment thickness from the bathymetry. Topographic contours are plotted at 0.5 km intervals with 1-km intervals shown by thicker lines and annotated.

The ambient field direction for the Fourier domain inversions was calculated using the IGRF model at the center of Tamu Massif, giving a declination of -1.4º and an inclination of 43.6º. Clues about the remanent field direction are given by the paleomagnetic data from drilling samples and paleomagnetic poles of the Pacific plate during the Early Cretaceous and Late Jurassic. Paleomagnetic analysis from ODP Site 1213 and IODP site U1347 as well as magnetic wireline log interpretation from Site U1347 imply that Tamu Massif formed near the paleoequator (Tominaga et al., 2012; Sager et al., 2015). Therefore, a reasonable assumption for the remanent inclination is near-zero. As to the declination of the remanent field, the paleomagnetic pole for Chrons M16-M21 (Larson and Sager, 1992) implies a declination of ~8.5º. Because of large uncertainties in these paleomagnetic direction values, we tested remanent field direction values with near-zero inclination (-30º to 30º) and near-zero declination (-30º to 30º). The model with -20º inclination and 0º declination was selected as a representative result. Other magnetization models derived from other remanent field directions were insignificantly different.

4.4 Results

4.4.1 Magnetic anomaly patterns

With new data, the new magnetic anomaly map over Tamu Massif shows greater detail than previous studies (Fig. 24). The anomalies around and within Tamu Massif are complex but are mostly linear or curvilinear segments, many of which display trends in

accord with the NW-SE Hawaiian or SW-NE Japanese lineations. Anomalies with discordant trends mainly occur over the center and the west of Tamu Massif.

Around Tamu Massif, most parts of the abyssal plain are characterized by narrow and linear magnetic anomalies whose trends agree with the isochrons traced by Nakanishi et al. (1999) (Fig. 24). Lineations to the southwest, northeast and northwest of Tamu Massif are relatively long and distinct with the former two regions recording the NW-SE trending Hawaiian lineations and the latter recording the SW-NE trending Japanese lineations. In contrast, Hawaiian lineations in the abyssal plain to the southeast are short and less coherent, which may be caused by short ridge segments and sparse measurements.

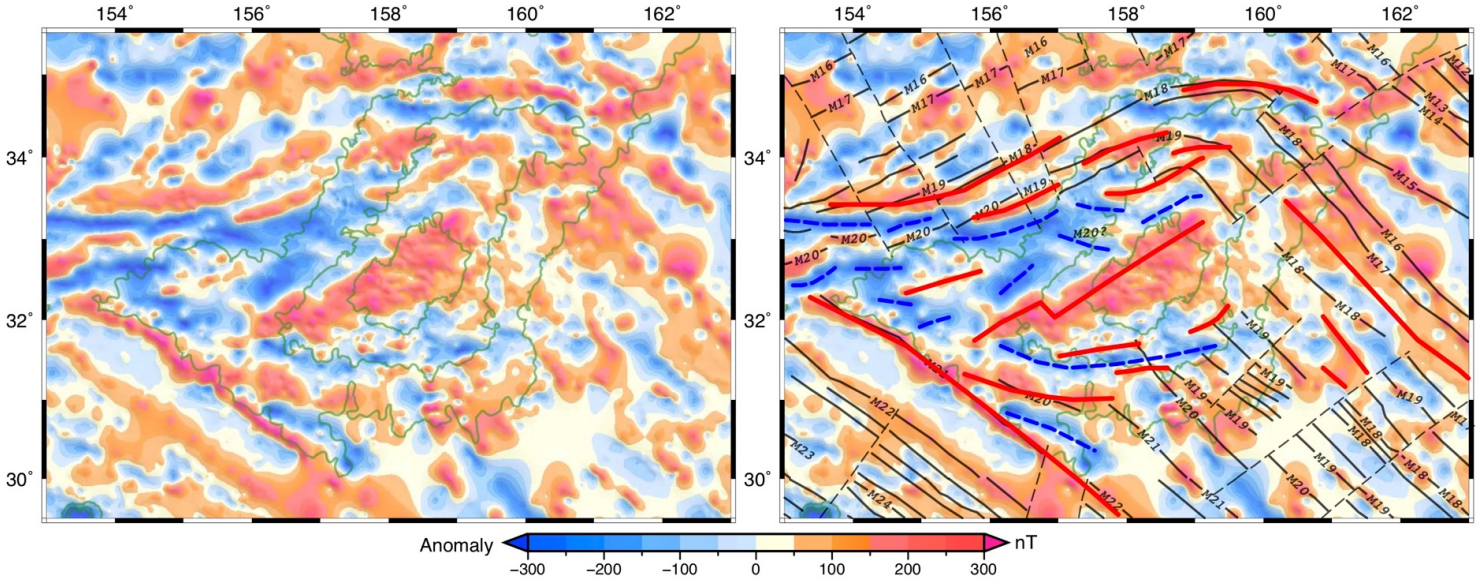

Figure 24. Magnetic anomaly map for Tamu Massif. (left) Anomaly map with bathymetry contours of -5, -4 and -3 km, denoted by green lines. (right) Anomaly map compared to lineations. Solid black lines show magnetic isochrons identified by Nakanishi et al. (1999), and dashed black lines show fracture zones. Solid red lines represent newly-identified positive lineations, while dashed blue lines represent newly-identified negative lineations.

The most distinct feature in the anomaly map is the broad positive anomaly at the center of Tamu Massif. The width of this anomaly is broader compared to other anomalies in our study area. Unexpectedly, this anomaly is also linear, especially on its north side, and it trends in the SW-NE direction, parallel to the Japanese lineations.

To the south of the central positive, around 31.5°N and extending from 156°E to 160°E, there is a long curvilinear negative anomaly that cuts through the Hawaiian lineations identified by Nakanishi et al. (1999). It extends eastward with a trend of W-E and its north and south are characterized by anomalies with similar trends. At 31.0°N, 156.5°E, there is a linear positive anomaly, identified by Nakanishi et al. (1999) as M20, with a trend ~20° counterclockwise from that of nearby anomaly M21. With the help of new data, we traced this anomaly as longer and splitting from M21 at 31.2°N, 155.5°E.

To the north of the central positive, a series of linear or curvilinear magnetic anomalies were identified. Most of the lineations in this area trend SW-NE, in consistent with the orientation of the Japanese lineations. However, these lineations are less coherent with some of them trending almost E-W. At 32.4°N, 155.4°E, new data deciphered a broken positive lineation with the same trend as the central positive. Negative anomalies surrounding it, however, are not strictly trending SW-NE. New data also portrayed a low-amplitude positive lineation at 32.8°N, 157.2°E, on the north side of the central positive, just south of a short anomaly tentatively interpreted as M20 by Nakanishi et al. (1999). The trends of these two positives are also at odds with the nearby SW-NE trending Japanese lineations. Notably, at 33.2°N, 153°E an E-W trending negative lineation cuts through the M19 and M20 Japanese isochrons identified by

Nakanishi et al. (1999). North of it, we identified a long curvilinear positive anomaly, whose west part is also trending E-W, while the east part in alignment with Japanese lineations.

The northern flank of Tamu Massif is characterized by several magnetic bights that may be ascribed to the P-F-I triple junction. However, constraints from new data decipher the trajectories of these bights differently from that traced by Nakanishi et al. (1999). They identified two bights M19 and M18 around 34°N, 159°E, whereas our map shows two SW-NE trending curvilinear anomalies at 34°N, 158°E and 33.8°N, 158.8°E. The northern one fits well with the west arm of the M19 bight identified by Nakanishi et al. (1999), while the southern one seems to connect previously identified M19 and M18 bights. Father north, there are two curvilinear negative anomalies surrounding one approximately W-E trending positive anomaly at 34.8°N, 159.8°E. The positive is also curved and appears to be the apex of a magnetic bight.

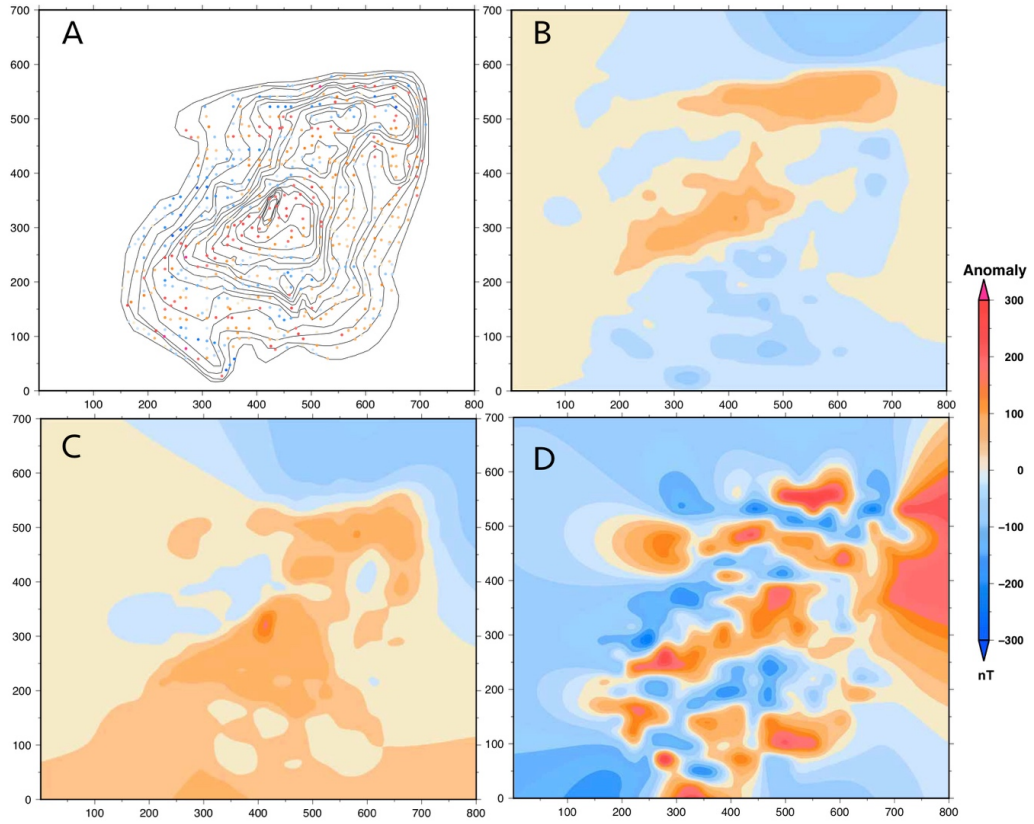

Figure 25. Results of homogeneous model (Plouff, 1976). (A) Input magnetic anomaly measurements and polygons following topographic contours used to represent the source body. (B) Calculated magnetic anomalies from a forward model with remanent magnetization representative of an equatorial formation. (C) Calculated magnetic field from the least-squares inversion. (D) Residual magnetic field from subtracting least-square inversion model from observed magnetic anomalies.

4.4.2 Results of magnetic models

4.4.2.1 Homogeneous model

The least-squares inversion of the homogeneous magnetization model exhibits similar results to those of Sager and Han (1993), giving a reversed polarity with an inclination of 74.5º and a declination of 155.4º. This remanent field direction does not agree with the inclination and declination values (8º, 9º for normal polarity, -8°, 189° for

reversed polarity) estimated from the M16-M21 paleomagnetic pole of Larson and Sager (1992). The calculated inclination (74.5º) is much higher because of the location of the positive anomaly over the center of the edifice. A forward model (Fig. 25B) used a magnetization consistent with the M16-M21 paleomagnetic pole (Larson and Sager, 1992). Although both models fit the pattern of a central positive anomaly with flanking negative anomalies (Figs. 25B, 25C), the amplitude of the calculated anomalies is low. For the inverse model, the correlation coefficient (calculated versus observed anomalies) is only ~0.28, suggesting a poor match of the calculated anomalies to the observed anomalies. Residual anomalies (observed minus calculated) have similar amplitudes and patterns to the observed magnetic anomalies (Fig. 25D). In general, the long-wavelength model failed to mimic short-wavelength features (i.e., narrow and linear magnetic anomalies) in the observed anomalies.

4.4.2.2 Uniform thickness inverse model

The magnetization structure resulting from the uniform thickness model exhibits high similarity to the pattern of the observed anomaly map. Most of the linear magnetic anomalies are recovered as linear magnetization blocks. Positive magnetic anomalies correlate to reversely magnetized blocks and vice versa (Fig. 26). Magnetic lineations on the lower flanks and adjacent abyssal plain around Tamu Massif are modeled as narrow linear magnetized zones, like those typically formed at spreading ridges. Magnetization zones at the center and west of Tamu Massif are also linear but broader than surrounding linear magnetization zones.

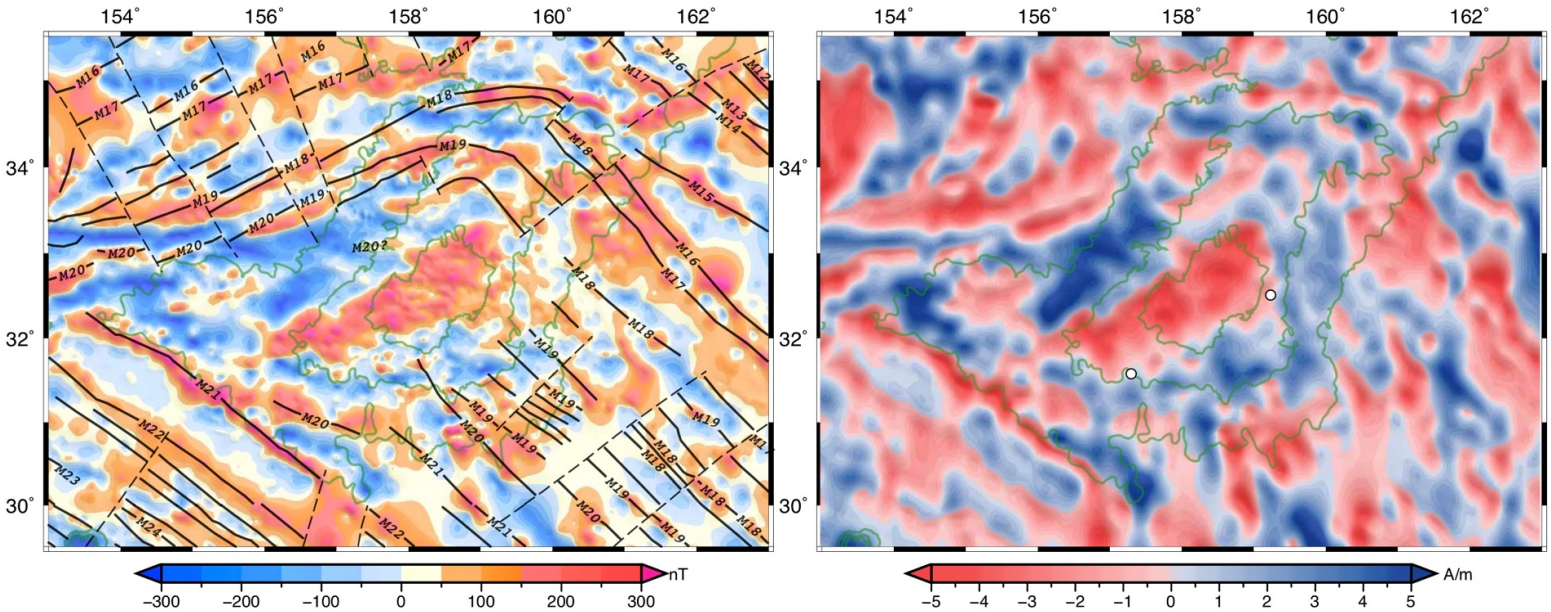

Figure 26. Magnetic anomaly map(left) compared to magnetization map (right) calculated by uniform thickness model (Parker and Huestis, 1974). In left map, solid and dashed lines denote magnetic isochrons and fracture zones, respectively. Green contours show bathymetry contours for Tamu Massif at -5, -4 and -3 km. White filled black circles show the locations of ODP Site 1213 and IODP Site U1347.

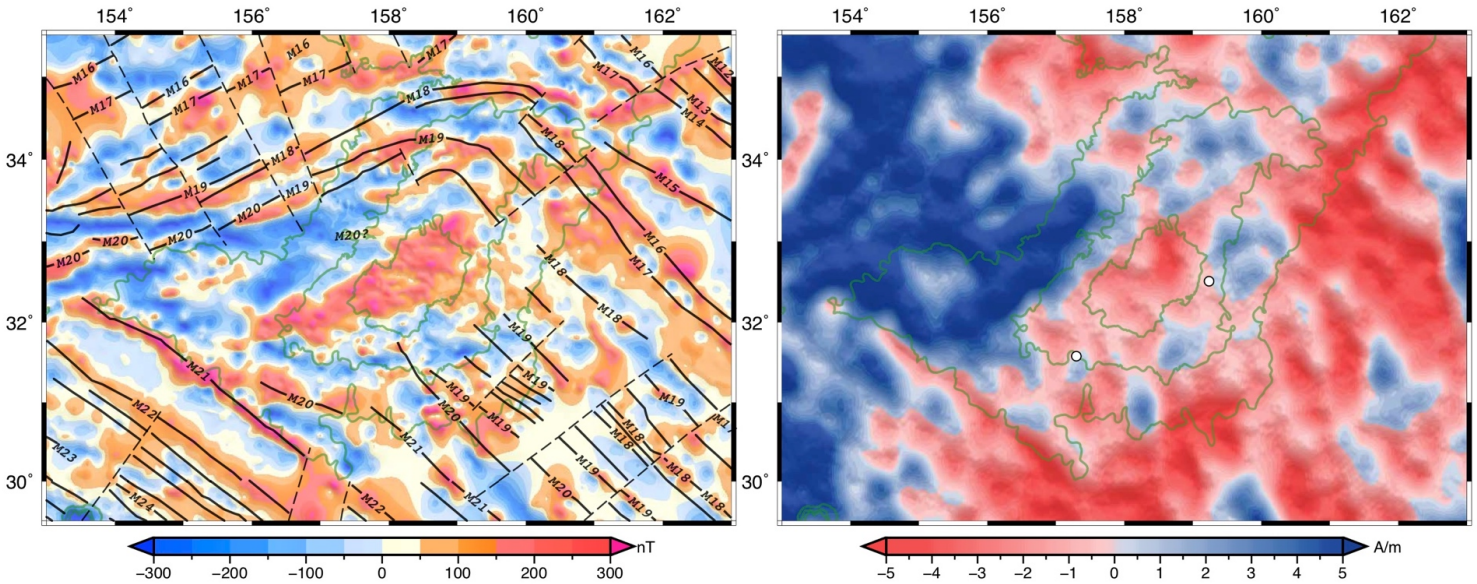

Figure 27. Magnetic anomaly map (left) compared to magnetization map (right) calculated by variable thickness model (Caratini Tontoni et al., 2008). Annotations are the same as those in Figure 26.

4.4.2.3 Variable thickness inverse model

As shown in Figure 27, the variable thickness model did a poor job of recovering the observed anomaly patterns. Broad negative and positive magnetization zones characterize the northwest and southeast areas of our study area, respectively. The model mimics the linear central positive and a linear reversed-polarity magnetization zone related to the M21 Chron that follows the southwest boundary of Tamu Massif. Other linear features, including the strong linear magnetic anomalies on the northwest flank and magnetic bights across the northeast flank, are not represented in the magnetization map. Because this model does a poor job of recovering the highly linear anomalies over abyssal oceanic crust, it is considered unreliable. The reasons for this failure are unclear and outside the scope of this study. It is notable that this technique has not been widely applied.

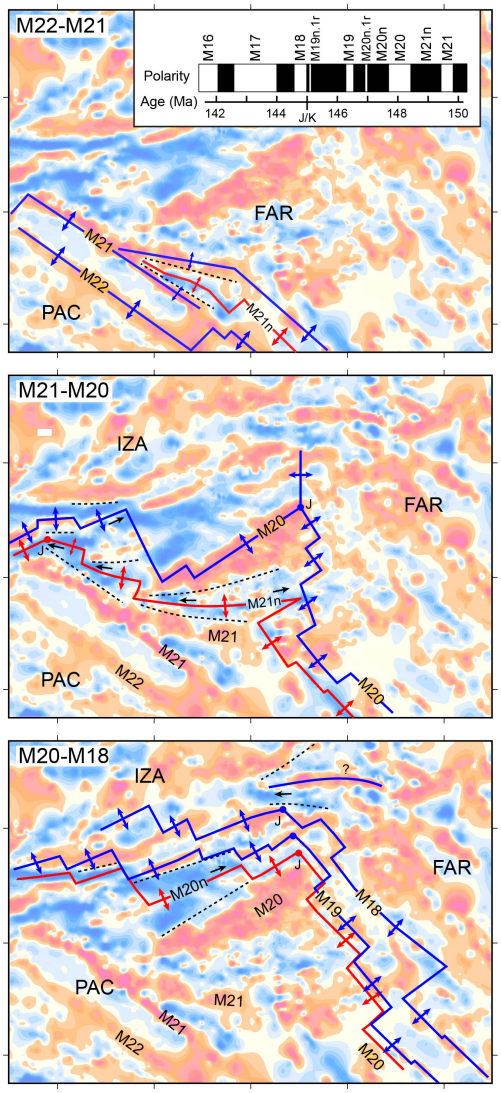

Figure 28. Reconstruction of tectonic evolution of Tamu Massif. (top) The counterclockwise rotation of Pacific-Farallon ridge began with the split of M21. (middle) The rotation continued between Chrons M21n and M20r, end up with the broad central positive which show a trend parallel to Pacific-Izanagi ridge. (bottom) Magnetic bights resumed regularly from M20n to M18, traversing the northern flank of Tamu Massif. Red (blue) lines denote spreading ridges during normal (reversed) geomagnetic polarity time periods, with small arrows showing the direction of seafloor spreading. Red and blue dots, annotated with "J", show the apex of the P-F-I triple junction. Dashed lines show wedge-shaped anomalies owing to ridge propagations, with small black arrows show the propagating direction. Inset map is the geomagnetic polarity time scale from Late Jurassic to Early Cretaceous (Ogg, 2012). J/K means Jurassic-Cretaceous boundary.

4.5 Discussion

The new magnetic anomaly map constructed for Tamu Massif is characterized by linear anomalies, implying that this massive volcanic edifice formed by seafloor spreading. This is a significant change in our view of how this volcano was emplaced. The newly-identified anomalies seem to record the reorientation of a segment of Pacific-Farallon ridge synchronous with the northeast migration of the P-F-I triple junction across Tamu Massif. The preservation of these linear and curvilinear anomalies is unexpected as Tamu Massif has been postulated to be an enormous shield volcano constructed by voluminous eruptions. The modeling results, however, indicate that these linear features are most likely produced by magnetization blocks of alternating normal and reversed polarities, similar to the magnetic structure of spreading ridges.

The overall pattern of the magnetic lineations across Tamu Massif can be explained by a ~90º counterclockwise rotation of the Pacific-Farallon Ridge (Fig. 24, Fig. 28). The rotation appears to have initiated with a split of M21 by propagating ridge during M20n (Fig. 28A) and ceased as the linear central positive (M20) formed. The rotation shifted the Pacific-Farallon ridge from trending NW-SE to SW-NE, ultimately in alignment with the Pacific-Izanagi ridge and Japanese lineations (Fig. 28B). Magnetic anomalies also show some complex features in response to ridge reorientations and possible microplate tectonics. The central positive and the negative anomalies west of it are of greater width compared to adjacent anomalies, indicating rapid crustal accretion during the building of the Tamu Massif edifice. North and south of the central positive, there are multiple curvilinear anomalies that appear to reflect changes in spreading

direction. Short positive segments over the west flank of Tamu Massif overlap with the broad negative that we identified as M20n (Fig. 24, Fig. 28), suggesting that the anomaly sequence is non-monotonic, which may be ascribed to ridge jumps. The positive anomaly at 32.4°N, 155.4°E, located over the southwestern "tail" of Tamu Massif, has the same trend as the Japanese lineations, indicating that this is a separate edifice that did not grow large. The E-W trending negative that cuts through magnetic bights at 34.5°N, 159°E appears to be another indicator of the complex tectonic reorganization.

Interpreted as recording the rotation of Pacific-Farallon ridge, the magnetic anomalies over Tamu Massif show mostly continuous age progression from south to north. Due to the complex tectonics, it is difficult to identify magnetic isochrons with certainty, especially for some poorly surveyed areas, such as northwest of Tamu Massif. However, isochrons bracketing Tamu Massif suggest its formation between M21 and M19 (Nakanishi et al., 1999). The central positive and its flanking lows may be a normal-reversed-normal (N-R-N) polarity transition with respect to the aforementioned ~90º rotation of the Pacific-Farallon ridge. It is hypothesized here that this N-R-N period is M21n-M20n (149.4-146.5 Ma, 2.9 Ma) (Fig. 28). The volume of Tamu Massif is ~4.8 x 10^6 km^3(Zhang et al., 2016), of which approximately 70% is related to the N-R-N period. These constraints imply an eruption rate of ~1.2 km^3a^{-1}. Although our anomaly map does not support Tamu Massif's formation within just one single reversed polarity as proposed by Sager and Han (1993), the effusion rate is not greatly different. The eruption rate is still extraordinarily large, comparable to eruption rates of flood basalts

(e.g., 1.5 km^3a^{-1} at Deccan Traps; Richards, et al., 1989), and consistent with the plume-head hypothesis.

Modeling results suggest that the magnetization structure of Tamu Massif is not vertical stack of lava layers, but rather is comprised by lateral magnetization blocks with alternating geomagnetic polarities. This finding is supported by paleomagnetic data from ODP Site 1213 and IODP Site U1347 (Fig. 26), which gave paleoinclination values with opposite signs (Tominaga et al., 2005; Sager et al., 2015), implying different magnetic polarities. Although near the borders of magnetization blocks (Fig. 26B), the two sites appear to be in different polarity zones. The magnetization model implies that the formation of Tamu Massif is similar to crustal accretion by seafloor spreading. Linear magnetization blocks formed at spreading centers are caused by 2D upwelling constrained to the ridge axis (e.g., Macdonald, 1982; Gee and Kent, 2007). Although, the greater crustal thickness implies an extraordinary magma supply for Tamu Massif, the magnetic pattern implies that lava flows rarely flowed far from the ridge axis, otherwise the linear anomaly pattern would have been obscured. That is to say, the formation and structure of Tamu Massif are different from seamounts or central volcanoes. Tamu Massif is the crust itself, not a volcano sitting on pre-existing crust. The morphology of Tamu Massif indicates changes of the magma supply and crustal thickness, rather than edifice building by stacked lava flows.

Several lines of evidence appear to concur with the spreading model proposed here. It has been proposed that Tamu Massif was formed by a plume head eruption (Sager and Han, 1993; Nakanishi et al., 1999; Sager et al., 1999). So far, however, there

is no direct evidence that strongly supports mantle plume formation of Tamu Massif. Instead, geochemical analysis of basaltic samples from Tamu Massif displays large overlap with the signature of N-MORB (Mahoney et al., 2005; Sano et al., 2012; Husen et al., 2013). Moreover, $^{40}Ar/^{39}Ar$ ages estimated from ODP Site 1213 and lower basaltic unit of IODP Site U1347 are around 143-145 Ma (Mahoney et al., 2005; Heaton and Koppers, 2014; Geldmacher et al., 2014; Tejada et al., 2016), almost contemporaneous with magnetic Chrons M20-M19 that traverse Tamu Massif. The small difference in age may be a result of poor calibration of the M-sequence magnetic anomalies (Tominaga and Sager, 2010). In addition, Tamu Massif is characterized by small-amplitude free-air gravity anomalies, similar to those observed at spreading centers (Sandwell and MacKenzie, 1989). This is different from shield volcanoes which often display local zones of mass concentration caused by intrusive rocks (Strange et al., 1965). Moreover, Tamu Massif seems to have been in isostatic balance as it evolved (Sager et al., 2013; Zhang et al., 2015). If massive eruptions focused at the center of Tamu Massif, the accumulation of voluminous lava flows would have depressed the center and intra-basement reflectors should dip toward the center, similar to seaward dipping reflectors found at continental margins (Mutter, 1985; Planke et al., 2000). This is not observed (Sager et al, 2013). Another surprising finding is that the slopes of stratified lava sequences are abnormally low at Tamu Massif (Sager et al., 2013; Zhang et al., 2015). This may be explained by the formation at a spreading center where the lithosphere is thin and weak.

4.6 Conclusion

This study compiled of a large and heterogeneous magnetic data set to define magnetic anomalies over and around Tamu Massif. Surprisingly, Tamu Massif, even at its center, is characterized by linear magnetic anomalies. The magnetic anomaly pattern implies a ~90º counterclockwise rotation of a segment of the Pacific-Farallon ridge tied to the formation of Tamu Massif. The rotation of Pacific-Farallon ridge segment is interpreted here as coeval with geomagnetic field reversals of M21n-M20r-M20n (149.4-146.5 Ma, 2.9 Ma). This differs from previous studies that ascribed the formation of Tamu Massif to the massive eruption of a central volcano.

The interpretation of multiple magnetic polarities within Tamu Massif is supported by paleomagnetic data as two drilling sites (1213 and U1347) on Tamu Massif yielded paleoinclinations of opposite signs, indicating geomagnetic polarity reversals.

The modeling results show that linear magnetic anomalies are produced by linear magnetization blocks with alternating normal and reversed polarities, analogous to crust formed at spreading ridges. Thus, Tamu Massif does not appear to be a central volcano, but is a product of seafloor spreading. The preservation of anomaly linearity implies that voluminous volcanic eruptions that contribute to Tamu Massif's thickened crust (~30 km at the center) must not significantly escape the neo-volcanic zone to obscure the linear pattern.

Odd observations that are not well explained by previous studies are explained by the spreading model for Tamu Massif. Small gravity anomalies suggest that Tamu Massif is in complete isostatic compensation, consistent with the formation near

spreading ridges. Lack of dipping-to-center reflectors in seismic profiles does not support the stacking of lava flows at the volcano center. And the morphology of Tamu Massif is not normal slope of a volcano but are indicator of variant amount of magma outpouring.

CHAPTER V

SUMMARY OF CONCLUSIONS

After systematic corrections to a large and heterogeneous magnetic data set, we constructed a new magnetic anomaly map for Shatsky Rise. The mean and root mean square of crossover errors have been greatly reduced and the improvements of the data set are also evident in the final magnetic anomaly map. Surprisingly, the whole Shatsky Rise is mainly characterized by linear magnetic anomalies, analogous to what usually observed at spreading ridges. High edifices are even traversed by linear magnetic anomalies, indicating that the emplacement of high edifices has little effect on the pattern of magnetic anomalies. In places around the high edifies, disturbances to the magnetic anomaly pattern were identified, indicating complex tectonic regimes involved during the formation of Shatsky Rise, which may be produced by the influence of a hotspot.

Ori Massif is traversed by linear and coherent SW-NE trending magnetic anomalies, parallel to surrounding Japanese lineations and thus indicating its formation at the Pacific-Izanagi spreading ridge. Several findings suggest that its formation is more complex than normal oceanic crust accretion. We identified a new magnetic bight north of Ori Massif. Surrounded with the M17 bight to the south and the newly recognized bight to the north, Ori Massif may have formed on a microplate encompassed by multiple triple junctions. Furthermore, we identified another repeated M16 Chron resulting from a ridge jump. Modeling results reveal the magnetic structure of Ori Massif, which appear to be constructed by horizontal array of linear magnetization

blocks showing different geomagnetic polarities. The implication is that Ori Massif is not a central volcano, but rather a product of seafloor spreading.

Like Ori Massif, new data reveal that Tamu Massif is also traversed by linear and curvilinear magnetic anomalies. Whereas, the central anomalies are not so coherent and clear as those in Ori Massif. The most astonishing finding is that magnetic lineations across Tamu Massif seems to show an ~90º counterclockwise rotation of Pacific-Farallon Ridge. West of Tamu Massif, curvilinear and "V-shape" magnetic anomalies are identified, indicating ridge propagations. The rotation occurred during Chrons M21n-M21r-M20n (149.4-146.5 Ma), suggesting that Tamu Massif did not form at just one geomagnetic polarity time. Magnetic modeling results indicate that linear magnetic anomalies are produced by alternating magnetization blocks of normal and reversed polarity, similar to crustal accretion at spreading centers. In this view, Tamu Massif is not a central volcano with vertical sequences of lava layers. Instead, its magnetic structure shows lateral combination of different polarity magnetization blocks.

The magnetic structures of Tamu and Ori massifs suggest that, although extra magma supply thickened the crust, 2D magma upwelling dominates and lava flows are still confined to neo-volcanic zone. No widespread lava flows should form to obscure the linearity of the magnetic anomalies. Many oceanic plateaus have been formed near spreading ridges, even triple junctions. If oceanic plateaus are products of mantle plumes, these coincidences may indicate a link between mantle plumes and spreading ridges.

REFERENCES

Anderson, D.L., Natland, J.H., 2014. Mantle updrafts and mechanisms of oceanic volcanism. Proc. Natl. Acad. Sci. 111, E4298-E4304. https://doi.org/10.1073/pnas.1410229111

Bartels, J., Heck, N.H., Johnston, H.F., 1939. The three-hour-range index measuring geomagnetic activity. Terr. Magn. Atmos. Electr., 44, 411–454. https://doi.org/10.1029/TE044i004p00411

Bijwaard, H., Spakman, W., 1999. Tomographic evidence for a narrow whole mantle plume below Iceland. Earth Planet. Sci. Lett. 166, 121–126. https://doi.org/10.1016/S0012-821X(99)00004-7

Bird, R.T., Naar, D.F., Larson, R.L., Searle, R.C., Scotese, C.R., 1998. Plate tectonic reconstructions of the Juan Fernandez microplate: Transformation from internal shear to rigid rotation. J. Geophys. Res. Earth 103, 7049–7067. https://doi.org/10.1029/97jb02133

Brozena, J.M., White, R.S., 1990. Ridge jumps and propagations in the South Atlantic Ocean. Nature 348, 149–152. https://doi.org/10.1038/348149a0

Campbell, I.H., Griffiths, R.W., 1990. Implications of mantle plume structure for the evolution of flood basalts. Earth Planet. Sci. Lett. 99, 79–93. https://doi.org/10.1016/0012-821X(90)90072-6

Cande, S.C., LaBrecque, J.L., Haxby, W.F., 1988. Plate Kinematics of the South Atlantic: Chron C34 To Present. J. Geophys. Res. Solid Earth 93, 13479–13492. https://doi.org/10.1029/JB093iB11p13479

Cannat, M., Briais, A., Deplus, C., Escartín, J., Georgen, J., Lin, J., Mercouriev, S., Meyzen, C., Muller, M., Pouliquen, G., Rabain, A., da Silva, P., 1999. Mid-Atlantic Ridge–Azores hotspot interactions: along-axis migration of a hotspot-derived event of enhanced magmatism 10 to 4 Ma ago. Earth Planet. Sci. Lett. 173, 257–269. https://doi.org/10.1016/S0012-821X(99)00234-4

Caratori Tontini, F., Cocchi, L., Carmisciano, C., 2008. Potential-field inversion for a layer with uneven thickness: The Tyrrhenian Sea density model. Phys. Earth Planet. Inter. 166, 105–111. https://doi.org/10.1016/j.pepi.2007.10.007

Carbotte, S., Mutter, C., Mutter, J., Ponce-Correa, G., 1998. Influence of magma supply and spreading rate on crustal magma bodies and emplacement of the extrusive

layer: Insights from the East Pacific Rise at lat 16°N. Geology 26, 455–458. https://doi.org/10.1130/0091-7613(1998)026<0455:iomsas>2.3.co;2

Chandler, M.T., Wessel, P., Taylor, B., Seton, M., Kim, S.S., Hyeong, K., 2012. Reconstructing Ontong Java Nui: Implications for Pacific absolute plate motion, hotspot drift and true polar wander. Earth Planet. Sci. Lett. 331, 140–151. https://doi.org/10.1016/j.epsl.2012.03.017

Chandler, M.T., Wessel, P., 2008. Improving the quality of marine geophysical track line data: Along-track analysis. J. Geophys. Res. Solid Earth 113, B02102. https://doi.org/10.1029/2007JB005051

Coffin, M.F., Eldholm, O., 1994. Large igneous provinces: Crustal structure, dimensions, and external consequences. Rev. Geophys. 32, 1–36. https://doi.org/10.1029/93RG02508

Colman, A., Sinton, J.M., White, S.M., McClinton, J.T., Bowles, J.A., Rubin, K.H., Behn, M.D., Cushman, B., Eason, D.E., Gregg, T.K.P., Gronvold, K., Hidalgo, S., Howell, J., Neill, O., Russo, C., 2012. Effects of variable magma supply on mid-ocean ridge eruptions: Constraints from mapped lava flow fields along the Galapagos Spreading Center. Geochemistry Geophys. Geosystems 13, Q08014. https://doi.org/10.1029/2012gc004163

Duncan, R.A., Richards, M.A., 1991. Hotspots, mantle plumes, flood basalts, and true polar wander. Rev. Geophys. 29, 31–50. https://doi.org/10.1029/90RG02372

Expedition 324 Scientists, E., 2010. Site U1347, in: Sager, W.W., Sano, T., Gelsmacher, J. (Eds.). Proceeding of the IODP. https://doi.org/10.2204/iodp.proc.324.104.2010

Finlay, C.C., Maus, S., Beggan, C.D., Bondar, T.N., Chambodut, A., Chernova, T.A., Chulliat, A., Golovkov, V.P., Hamilton, B., Hamoudi, M., Holme, R., Hulot, G., Kuang, W., Langlais, B., Lesur, V., Lowes, F.J., Lühr, H., Macmillan, S., Mandea, M., McLean, S., Manoj, C., Menvielle, M., Michaelis, I., Olsen, N., Rauberg, J., Rother, M., Sabaka, T.J., Tangborn, A., Tøffner-Clausen, L., Thébault, E., 2010. International Geomagnetic Reference Field: the eleventh generation. Geophys. J. Int. 183, 1216–1230. https://doi.org/10.1111/j.1365-246X.2010.04804.x

Foulger, G.R., 2002. Plumes, or plate tectonic processes? Astron. Geophys. 43, 6.19-6.23. https://doi.org/10.1046/j.1468-4004.2002.43619.x

Foulger, G.R., Anderson, D.L., 2005. A cool model for the Iceland hotspot. J. Volcanol. Geotherm. Res. 141, 1–22. https://doi.org/10.1016/j.jvolgeores.2004.10.007

Foulger, G.R., Natland, J.H., Anderson, D.L., 2005. Genesis of the Iceland melt anomaly by plate tectonic processes, in: Foulger, G.R., Natland, J.H., Presnall, D.C. (Eds.), Plates, Plumes and Paradigms. Geological Soc Amer Inc, Boulder. https://doi.org/10.1130/2005.2388(35)

Foulger, G.R., Du, Z., Julian, B.R., 2003. Icelandic-type crust. Geophys. J. Int. 155, 567–590. https://doi.org/10.1046/j.1365-246X.2003.02056.x

Foulger, G.R., 2007. The "plate" model for the genesis of melting anomalies, in: Special Paper 430: Plates, Plumes and Planetary Processes. https://doi.org/10.1130/2007.2430(01)

Fullerton, L.G., Sager, W.W., Handschumacher, D.W., 1989. Late Jurassic-Early Cretaceous evolution of the eastern Indian Ocean adjacent to northwest Australia. J. Geophys. Res. Earth Planets 94, 2937–2953. https://doi.org/10.1029/JB094iB03p02937

Gee, J.S., Kent, D. V., 2007. Source of Oceanic Magnetic Anomalies and the Geomagnetic Polarity Timescale, in: Treatise on Geophysics. pp. 455–507. https://doi.org/10.1016/B978-044452748-6.00097-3

Geldmacher, J., van den Bogaard, P., Heydolph, K., Hoernle, K., 2014. The age of Earth's largest volcano: Tamu Massif on Shatsky Rise (northwest Pacific Ocean). Int. J. Earth Sci. 103, 2351–2357. https://doi.org/10.1007/s00531-014-1078-6

Gente, P., Dyment, J., Maia, M., Goslin, J., 2003. Interaction between the Mid-Atlantic Ridge and the Azores hot spot during the last 85 Myr: Emplacement and rifting of the hot spot-derived plateaus. Geochemistry Geophys. Geosystems 4, 23. https://doi.org/10.1029/2003gc000527

Georgen, J.E., 2011. Lithospheric control on the spatial pattern of Azores hotspot seafloor anomalies: Constraints from a model of plume-triple junction interaction. Geophys. Res. Lett. 38, L19305. https://doi.org/10.1029/2011GL048742

Gibbons, A.D., Barckhausen, U., Van Den Bogaard, P., Hoernle, K., Werner, R., Whittaker, J.M., Müller, R.D., 2012. Constraining the Jurassic extent of Greater India: Tectonic evolution of the West Australian margin. Geochemistry, Geophys. Geosystems 13, Q05W13. https://doi.org/10.1029/2011GC003919

Gudmundsson, A., 2012. Magma chambers: Formation, local stresses, excess pressures, and compartments. J. Volcanol. Geotherm. Res. 237, 19–41. https://doi.org/10.1016/j.jvolgeores.2012.05.015

Hardarson, B.S., Fitton, J.G., Ellam, R.M., Pringle, M.S., 1997. Rift relocation - A geochemical and geochronological investigation of a palaeo-rift in northwest Iceland. Earth Planet. Sci. Lett. 153, 181–196. https://doi.org/10.1016/S0012-821X(97)00145-3

Harris, P.T., Macmillan-Lawler, M., Rupp, J., Baker, E.K., 2014. Geomorphology of the oceans. Mar. Geol. 352, 4–24. https://doi.org/10.1016/j.margeo.2014.01.011

Harrison, C.G.A., Jarrard, R.D., Vacquier, V., Larson, R.L., 1975. Paleomagnetism of Cretaceous Pacific Seamounts. Geophys. J. R. Astron. Soc. 42, 859–882. https://doi.org/10.1111/j.1365-246X.1975.tb06455.x

Heaton, D.E., Kroppers, A.A.P., 2014. Constraining the rapid construction of TAMU Massif at an ~145Myr old triple junction, Shatsky Rise, in: V.M. Goldschmidt Conference - Program and Abstracts, Vol. 24, p.948. Sacramento, CA.

Heirtzler, J.R., Dickson, G.O., Herron, E.M., Pitman, W.C., Lepichon, X., 1968. Marine magnetic anomalies, geomagnetic field reversals, and motions of the ocean floor and continents. J. Geophys. Res. 73, 2119–2136. https://doi.org/10.1029/JB073i006p02119

Hey, R.N., 2004. Propagating rifts and microplates at mid-ocean ridges, in: Selley, R.C., Cocks, R., Plimer, I. (Eds.), Encyclopedia of Geology. London: Academic Press, pp. 396–405.

Heydolph, K., Murphy, D.T., Geldmacher, J., Romanova, I. V., Greene, A., Hoernle, K., Weis, D., Mahoney, J., 2014. Plume versus plate origin for the Shatsky Rise oceanic plateau (NW Pacific): Insights from Nd, Pb and Hf isotopes. Lithos 200–201, 49–63. https://doi.org/10.1016/j.lithos.2014.03.031

Hilde, T.W.C., Isezaki, N., Wageman, J.M., 1976. Mesozoic seafloor spreading in the north pacific, in: Sutton, G.H., Manghnani, M.H., Moberly, R., Mcafee E.U. (Eds.), The Geophysics of the Pacific Ocean Basin and Its Margin, A Volume of George P. Woolland, Geophys. Monogr. Ser. AGU, Washington, D.C., pp. 205–226. https://doi.org/10.1029/GM019p0205

Hirth, G., Kohlstedt, D.L., 1996. Water in the oceanic upper mantle: Implications for rheology, melt extraction and the evolution of the lithosphere. Earth Planet. Sci. Lett. 144, 93–108. https://doi.org/10.1016/0012-821x(96)00154-9

Husen, A., Almeev, R.R., Holtz, F., Koepke, J., Sano, T., Mengel, K., 2013. Geothermobarometry of basaltic glasses from the Tamu Massif, Shatsky Rise oceanic plateau. Geochemistry, Geophys. Geosystems 14, 3908–3928. https://doi.org/10.1002/ggge.20231

Ishihara, T., 2015. A new leveling method without the direct use of crossover data and its application in marine magnetic surveys: weighted spatial averaging and temporal filtering. Earth Planets Sp. 67, 11. https://doi.org/10.1186/s40623-015-0181-7

Ito, G., Lin, J., Graham, D., 2003. Observational and theoretical studies of the dynamics of mantle plume-mid-ocean ridge interaction. Rev. Geophys. 41, 24. https://doi.org/10.1029/2002rg000117

Ito, G., Shen, Y., Hirth, G., Wolfe, C.J., 1999. Mantle flow, melting, and dehydration of the Iceland mantle plume. Earth Planet. Sci. Lett. 165, 81–96. https://doi.org/10.1016/s0012-821x(98)00216-7

Ito, G., 2001. Reykjanes 'V'-shaped ridges originating from a pulsing and dehydrating mantle plume. Nature 411, 681–684.

Jonsson, G., Kristjansson, L., Sverrisson, M., 1991. Magnetic surveys of Iceland. Tectonophysics 189, 229–247. https://doi.org/10.1016/0040-1951(91)90499-I

Karson, F.A., 2002. Geologic structure of the uppermost oceanic crust created at fast- to intermediate-rate spreading centers. Annu. Rev. Earth Planet. Sci. 30, 347–384. https://doi.org/10.1146/annurev.earth.30.091201.141132

Koppers, A.A.P., Sano, T., Natland, J.H., Widdowson, M., Almeev, R., Greene, A.R., Murphy, D.T., Delacour, A., Miyoshi, M., Shimizu, K., Li, S., Hirano, N., Geldmacher, J., 2010. Massive basalt flows on the southern flank of Tamu Massif, Shatsky Rise: a reappraisal of ODP Site 1213 basement units, in: Proceedings of the IODP, 324. https://doi.org/10.2204/iodp.proc.324.109.2010

Korenaga, J., 2011. Velocity–depth ambiguity and the seismic structure of large igneous provinces: a case study from the Ontong Java Plateau. Geophys. J. Int. 185, 1022–1036. https://doi.org/10.1111/j.1365-246X.2011.04999.x

Korenaga, J., Sager, W.W., 2012. Seismic tomography of Shatsky Rise by adaptive importance sampling. J. Geophys. Res. Solid Earth 117, B08102. https://doi.org/10.1029/2012JB009248

Kristjansson, L., Jonsson, G., 2007. Paleomagnetism and magnetic anomalies in Iceland. J. Geodyn. 43, 30–54. https://doi.org/10.1016/j.jog.2006.09.014

Larson, R.L., Sager, W.W., 1992. Skewness of magnetic anomalies M0 to M29 in the northwestern Pacific. Proc., Sci. results, ODP, Leg 129, old Pacific crust 471–481. https://doi.org/10.2973/odp.proc.sr.129.137.1992

Larson, R.L., Chase, C.G., 1972. Late Mesozoic Evolution of the Western Pacific Ocean. GSA Bull. 83, 3627–3644.

Li, A., Detrick, R.S., 2003. Azimuthal anisotropy and phase velocity beneath Iceland: Implication for plume-ridge interaction. Earth Planet. Sci. Lett. 214, 153–165. https://doi.org/10.1016/S0012-821X(03)00382-0

Lin, J., Morgan, J.P., 1992. The spreading rate dependence of three-dimensional mid-ocean ridge gravity structure. Geophys. Res. Lett. 19, 13–16. https://doi.org/10.1029/91GL03041

Love, J.J., Remick, K.J., 2007. Magnetic Indices, in: Gubbins, D., Herrero-Bervera, E. (Eds.), Encyclopedia of Geomagnetism and Paleomagnetism. Springer Netherlands, pp. 509–512.

Macdonald, K.C., 1982. Mid-Ocean Ridges: Fine Scale Tectonic, Volcanic and Hydrothermal Processes Within the Plate Boundary Zone. Annu. Rev. Earth Planet. Sci. 10, 155–190. https://doi.org/10.1146/annurev.ea.10.050182.001103

Mahoney, J.J., Duncan, R.A., Tejada, M.L.G., Sager, W.W., Bralower, T.J., 2005. Jurassic-Cretaceous boundary age and mid-ocean-ridge-type mantle source for Shatsky Rise. Geology 33, 185–188. https://doi.org/10.1130/G21378.1

Mammerickx, J., Sharman, G.F., 1988. Tectonic evolution of the North Pacific during the Cretaceous quiet period. J. Geophys. Res. Earth Planets 93, 3009–3024. https://doi.org/10.1029/JB093iB04p03009

Maus, S., Barckhausen, U., Berkenbosch, H., Bournas, N., Brozena, J., Childers, V., Dostaler, F., Fairhead, J.D., Finn, C., Von Frese, R.R.B., Gaina, C., Golynsky, S., Kucks, R., Lühr, H., Milligan, P., Mogren, S., Müller, R.D., Olesen, O., Pilkington, M., Saltus, R., Schreckenberger, B., Thébault, E., Tontini, F.C., 2009. EMAG2: A 2-arc min resolution Earth Magnetic Anomaly Grid compiled from satellite, airborne, and marine magnetic measurements. Geochemistry, Geophys. Geosystems 10, Q08005. https://doi.org/10.1029/2009GC002471

McClinton, J.T., White, S.M., 2015. Emplacement of submarine lava flow fields: A geomorphological model from the Ninos eruption at the Galapagos Spreading Center. Geochemistry Geophys. Geosystems 16, 899–911. https://doi.org/10.1002/2014gc005632

Meyer, B., Chulliat, A., Saltus, R., 2017. Derivation and Error Analysis of the Earth Magnetic Anomaly Grid at 2 arc min Resolution Version 3 (EMAG2v3). Geochemistry, Geophys. Geosystems 18, 4522–4537. https://doi.org/10.1002/2017GC007280

Mitchell, N.C., 2001. Transition from circular to stellate forms of submarine volcanoes. J. Geophys. Research 106, 1987–2003. https://doi.org/10.1029/2000JB900263

Mittelstaedt, E., Ito, G., Behn, M.D., 2008. Mid-ocean ridge jumps associated with hotspot magmatism. Earth Planet. Sci. Lett. 266, 256–270. https://doi.org/10.1016/j.epsl.2007.10.055

Mittelstaedt, E., Ito, G., Van Hunen, J., 2011. Repeat ridge jumps associated with plume-ridge interaction, melt transport, and ridge migration. J. Geophys. Res. Solid Earth 116, B01102. https://doi.org/10.1029/2010JB007504

Morgan, J.P., Chen, Y.J., 1993. The genesis of oceanic crust: Magma injection, hydrothermal circulation, and crustal flow. J. Geophys. Res. Solid Earth 98, 6283–6297. https://doi.org/10.1029/92JB02650

Morgan, W.J., 1971. Convection Plumes in the Lower Mantle. Nature 230, 42–43. https://doi.org/10.1038/230042a0

Mutter, J.C., Karson, J.A., 1992. Structural Processes at Slow-Spreading Ridges. Science. 257, 627–634. https://doi.org/10.1126/science.257.5070.627

Mutter, J.C., 1985. Seaward dipping reflectors and the continent-ocean boundary at passive continental margins. Tectonophysics 114, 117–131. https://doi.org/10.1016/0040-1951(85)90009-5

Nakanishi, M., Sager, W.W., Korenaga, J., 2015. Reorganization of the Pacific-Izanagi-Farallon triple junction in the Late Jurassic: Tectonic events before the formation of the Shatsky Rise, in: Neal, C.R., Sager, W.W., Sano, T., Erba, E. (Eds.), The Origin, Evolution, and Environmental Impact of Oceanic Large Igneous Provinces. Geological Society of America, pp. 85–101.

Nakanishi, M., Sager, W.W., Klaus, A., 1999. Magnetic lineations within Shatsky Rise, northwest Pacific Ocean: Implications for hot spot-triple junction interaction and oceanic plateau formation. J. Geophys. Res. 104, 7539–7556. https://doi.org/10.1029/1999JB900002

Nakanishi, M., Tamaki, K., Kobayashi, K., 1989. Mesozoic magnetic anomaly lineations and seafloor spreading history of the northwestern Pacific. J. Geophys. Res. 94, 15437–15462. https://doi.org/10.1029/JB094iB11p15437

Ogg, J.G., 2012. Geomagnetic Polarity Time Scale, in: The Geologic Time Scale 2012. Elsevier B.V., Department of Earth, Atmospheric and Planetary Sciences, Purdue University, Civil Engineering Building, 550 Stadium Mall Drive, West Lafayette,

IN 47907-2051, United States, pp. 85–113. https://doi.org/10.1016/B978-0-444-59425-9.00005-6

Onovughe, E., Holme, R., 2015. The CM4 model prediction of ground variation of the geomagnetic diurnal field away from quiet time. Phys. Earth Planet. Inter. 249, 1–10. https://doi.org/10.1016/j.pepi.2015.09.007

Parker, R.L., Huestis, S.P., 1974. The inversion of magnetic anomalies in the presence of topography. J. Geophys. Res. 79, 1587–1593. https://doi.org/10.1029/JB079i011p01587

Parmentier, E.M., Morgant, J.P., 1990. Spreading rate dependence of three-dimensional structure in oceanic spreading centres. Nature 348, 325–328. https://doi.org/10.1038/348325a0

Planke, S., Symonds, P.A., Alvestad, E., Skogseid, J., 2000. Seismic volcanostratigraphy of large-volume basaltic extrusive complexes on rifted margins. J. Geophys. Res. Solid Earth 105, 19335–19351. https://doi.org/10.1029/1999JB900005

Plouff, D., 1976. Gravity and magnetic fields of polygonal prisms and application to magnetic terrain corrections. GEOPHYSICS 41, 727–741. https://doi.org/10.1190/1.1440645

Quesnel, Y., Catalán, M., Ishihara, T., 2009. A new global marine magnetic anomaly data set. J. Geophys. Res. Solid Earth 114, B04106. https://doi.org/10.1029/2008JB006144

Richards, M.A., Duncan, R.A., Courtillot, V.E., 1989. Flood basalts and hot-spot tracks: Plume heads and tails. Science. 246, 103–107. https://doi.org/10.1126/science.246.4926.103

Ruedas, T., Schmeling, H., Marquart, G., Kreutzmann, A., Junge, A., 2004. Temperature and melting of a ridge-centred plume with application to Iceland. Part I: Dynamics and crust production. Geophys. J. Int. 158, 729–743. https://doi.org/10.1111/j.1365-246X.2004.02311.x

Ryan, M.P., 1990. The physical nature of the Icelandic magma transport system, in: Ryan, M.P. (Ed.), Magma Transport and Storage. Wiley, New York, pp. 175–224.

Sabaka, T.J., Olsen, N., Purucker, M.E., 2004. Extending comprehensive models of the Earth's magnetic field with Ørsted and CHAMP data. Geophys. J. Int. 159, 521–547. https://doi.org/10.1111/j.1365-246X.2004.02421.x

Sager, W.W., Han, H.C., 1993. Rapid formation of the Shatsky Rise oceanic plateau inferred from its magnetic anomaly. Nature 364, 610–613. https://doi.org/10.1038/364610a0

Sager, W.W., 2005. What built Shatsky Rise, a mantle plume or ridge tectonics? Geol. Soc. Am. Spec. Pap. 388, 721–733. https://doi.org/10.1130/0-8137-2388-4.721

Sager, W.W., Duncan, R.A., Handschumacher, D.W., 1993. Paleomagnetism of the Japanese and Marcus-Wake Seamounts, Western Pacific Ocean, in: The Mesozoic Pacific: Geology, Tectonics, and Volcanism. American Geophysical Union, pp. 401–435. https://doi.org/10.1029/GM077p0401

Sager, W.W., Lamarche, A.J., Kopp, C., 2005. Paleomagnetic modeling of seamounts near the Hawaiian–Emperor bend. Tectonophysics 405, 121–140. https://doi.org/10.1016/j.tecto.2005.05.018

Sager, W.W., Pueringer, M., Carvallo, C., Ooga, M., Housen, B., Tominaga, M., 2015. Paleomagnetism of igneous rocks from the Shatsky Rise: Implications for paleolatitude and oceanic plateau volcanism, in: Neal, C.R., Sager, W.W., Sano, T., Erba, E. (Eds.), The Origin, Evolution, and Environmental Impact of Oceanic Large Igneous Provinces. Geological Society of America. https://doi.org/10.1130/2015.2511(08)

Sager, W.W., Sano, T., Geldmacher, J., 2016. Formation and evolution of Shatsky Rise oceanic plateau: Insights from IODP Expedition 324 and recent geophysical cruises. Earth-Science Rev. 159, 306–336. https://doi.org/10.1016/j.earscirev.2016.05.011

Sager, W.W., Handschumacher, D.W., Hilde, T.W.C., Bracey, D.R., 1988. Tectonic evolution of the northern Pacific plate and Pacific-Farallon Izanagi triple junction in the Late Jurassic and Early Cretaceous (M21-M10). Tectonophysics 155, 345–364. https://doi.org/10.1016/0040-1951(88)90274-0

Sager, W.W., Kim, J., Klaus, A., Nakanishi, M., Khankishieva, L.M., 1999. Bathymetry of Shatsky Rise, northwest Pacific Ocean: Implications for ocean plateau development at a triple junction. J. Geophys. Res. Solid Earth 104, 7557–7576. https://doi.org/10.1029/1998JB900009

Sager, W.W., Sano, T., Geldmacher, J., 2011a. IODP expedition 324: Ocean drilling at Shatsky Rise gives clues about oceanic plateau formation. Sci. Drill. 12, 24–31. https://doi.org/10.2204/iodp.sd.12.03.2011

Sager, W.W., Sano, T., Geldmacher, J., 2011b. How do oceanic plateaus form? Clues from drilling at shatsky rise. Eos (Washington. DC). 92, 37–38. https://doi.org/10.1029/2011EO050001

Sager, W.W., Zhang, J., Korenaga, J., Sano, T., Koppers, A.A.P., Widdowson, M., Mahoney, J.J., 2013. An immense shield volcano within the Shatsky Rise oceanic plateau, northwest Pacific Ocean. Nat. Geosci. 6, 976–981. https://doi.org/10.1038/ngeo1934

Sandwell, D.T., Mackenzie, K.R., 1989. Geoid height versus topography for oceanic plateaus and swells. J. Geophys. Res. 94, 7403–7418. https://doi.org/10.1029/JB094iB06p07403

Sano, T., Shimizu, K., Ishikawa, A., Senda, R., Chang, Q., Kimura, J.I., Widdowson, M., Sager, W.W., 2012. Variety and origin of magmas on Shatsky Rise, northwest Pacific Ocean. Geochemistry, Geophys. Geosystems 13, Q08010. https://doi.org/10.1029/2012GC004235

Schmeling, H., Marquart, G., 2008. Crustal accretion and dynamic feedback on mantle melting of a ridge centred plume: The Iceland case. Tectonophysics 447, 31–52. https://doi.org/10.1016/j.tecto.2006.08.012

Sharman, G.F., Risch, D.L., 1988. Northwest Pacific tectonic evolution in the middle Mesozoic. Tectonophysics 155, 331–344. https://doi.org/10.1016/0040-1951(88)90273-9

Sinton, J.M., Detrick, R.S., 1992. Midocean ridge magma chambers. J. Geophys. Res. Earth 97, 197–216. https://doi.org/10.1029/91jb02508

Smith, W.H.F., Wessel, P., 1990. Gridding with continuous curvature splines in tension. GEOPHYSICS 55, 293–305. https://doi.org/10.1190/1.1442837

Smith, W.H.F., Sandwell, D.T., 1997. Global sea floor topography from satellite altimetry and ship depth soundings. Science. 277, 1956–1962. https://doi.org/10.1126/science.277.5334.1956

Staples, R.K., White, R.S., Brandsdottir, B., Menke, W., Maguire, P.K.H., McBride, J.H., 1997. Faroe-Iceland Ridge Experiment .1. Crustal structure of northeastern Iceland. J. Geophys. Res. 102, 7849–7866. https://doi.org/10.1029/96JB03911

Tamaki, K., Larson, R.L., 1988. The Mesozoic tectonic history of the Magellan microplate in the western central Pacific. J. Geophys. Res. 93, 2857–2874. https://doi.org/10.1029/JB093iB04p02857

Taylor, B., 2006. The single largest oceanic plateau: Ontong Java-Manihiki-Hikurangi. Earth Planet. Sci. Lett. 241, 372–380. https://doi.org/10.1016/j.epsl.2005.11.049

Tejada, M.L.G., Geldmacher, J., Hauff, F., Heaton, D., Koppers, A.A.P., Garbe-Schönberg, D., Hoernle, K., Heydolph, K., Sager, W.W., 2016. Geochemistry and age of Shatsky, Hess, and Ojin Rise seamounts: Implications for a connection between the Shatsky and Hess Rises. Geochim. Cosmochim. Acta 185, 302–327. https://doi.org/10.1016/j.gca.2016.04.006

Tominaga, M., Sager, W.W., 2010. Revised Pacific M-anomaly geomagnetic polarity timescale. Geophys. J. Int. 182, 203–232. https://doi.org/10.1111/j.1365-246X.2010.04619.x

Vine, F.J., Matthews, D.H., 1963. Magnetic anomalies over oceanic ridges. Nature 199, 947–949. https://doi.org/10.1038/199947a0

Vine, F.J., 1966. Spreading of the ocean floor: New evidence. Science. 154, 1405–1415. https://doi.org/10.1126/science.154.3755.1405

Wessel, P., 2010. Tools for analyzing intersecting tracks: The x2sys package. Comput. Geosci. 36, 348–354. https://doi.org/10.1016/j.cageo.2009.05.009

Wilson, J.T., 1963. Evidence from Islands on the spreading of ocean floors. Nature 197, 536-538. https://doi.org/10.1038/197536a0

Zhang, J., Sager, W.W., Korenaga, J., 2015. The Shatsky Rise oceanic plateau structure from two-dimensional multichannel seismic reflection profiles and implications for oceanic plateau formation, in: Neal, C.R., Sager, W.W., Sano, T., Erba, E. (Eds.), The Origin, Evolution, and Environmental Impact of Oceanic Large Igneous Provinces. Geological Society of America. https://doi.org/10.1130/2015.2511(06)

Zhang, J., Sager, W.W., Korenaga, J., 2016. The seismic Moho structure of Shatsky Rise oceanic plateau, northwest Pacific Ocean. Earth Planet. Sci. Lett. 441, 143–154. https://doi.org/10.1016/j.epsl.2016.02.042